Universidade de São Paulo
Instituto de Física

Raios cósmicos de ultra-altas energias: origem e propagação

Johnnier Pérez Armand

Orientador: Prof. Dr. Edivaldo Moura Santos

Tese apresentada ao Instituto de Física da Universidade de São Paulo como requisito parcial para obtenção do título de Doutor em Ciências

Banca Examinadora:

Prof. Dr. Edivaldo Moura Santos - Orientador (IFUSP)
Prof. Dr. Luis Raul Weber Abramo - (IFUSP)
Prof. Dr. Aion da Escossia Melo Viana - (IFSC/USP)
Profa. Dra. Carola Dobrigkeit Chinellato - (IFGW/Unicamp)
Prof. Dr. Rogério Menezes de Almeida - (UFF)

São Paulo
2023

FICHA CATALOGRÁFICA

Preparada pelo Serviço de Biblioteca e Informação do Instituto de Física da Universidade de São Paulo

Pérez Armand, Johnnier

Raios cósmicos de ultra-altas energias: origem e propagação /
Ultra-high energy cosmic rays: origin and propagation

São Paulo, 2022.

Tese (Doutorado) – Universidade de São Paulo. Instituto de Física.
Depto. de Física Experimental.

Orientador: Prof. Dr. Edivaldo Moura Santos.

Área de Concentração: Física.

Unitermos:

1. Cosmologia; 2. Astrofísica; 3. Raios cósmicos;
4. Chuveiros atmosféricos extensos; 5. Observatório Pierre Auger.

USP/IF/SBI-90/2022

University of São Paulo
Physics Institute

Ultra-high energy cosmic rays: origin and propagation

Johnnier Pérez Armand

Advisor: Prof. Dr. Edivaldo Moura Santos

Thesis submitted to the Physics Institute of the University of São Paulo in partial fulfillment of the requirements for the degree of Doctor of Science

---

Examining Committee:

Prof. Dr. Edivaldo Moura Santos - Advisor (IFUSP)

Prof. Dr. Luis Raul Weber Abramo - (IFUSP)

Prof. Dr. Aion da Escossia Melo Viana - (IFSC/USP)

Profa. Dra. Carola Dobrigkeit Chinellato - (IFGW/Unicamp)

Prof. Dr. Rogério Menezes de Almeida - (UFF)

São Paulo
2023

Acknowledgments

This study was financed in part by the Coordenação de Aperfeiçoamento de Pessoal de Nível Superior – Brasil (CAPES) – Finance Code 001.

I want also to thank my family and friends for their support and encouragement to reach my personal and professional goals. To my colleagues in the department of experimental physics (FEP), especially my advisor Edivaldo Moura Santos, for his instruction, disposition, and support during the development of my research. To the Institute of Physics and the USP in general for the logistic support that allowed me to use the computational resources of the university, especially the aguia4 cluster. To the CAPES agency, for the essential financial support to carry out my studies at this prestigious university. In general, to all the people who made possible the successful culmination of this important stage in my life.

Abstract

Cosmic rays are highly energetic charged nuclei that propagate through intergalactic space being the most energetic particles ever detected on Earth. Even though they have been exhaustively studied since their discovery more than 100 years ago, there are still many open questions in the field regarding the sources and mechanisms of creation and acceleration, chemical composition, energy spectrum, and arrival directions distribution, among others, which are the goal of current research. The main objective of this work is to explore astrophysical scenarios of origin and propagation consistent with the energy spectrum and depth of shower maximum ($X_{\rm max}$) data collected by the Pierre Auger Observatory in the region of ultra-high energies ($E \gtrsim 10^{17.5}\,$eV) over a period of more than 15 years of observations. The astrophysical models were constructed using the Monte Carlo code CRPropa to simulate the cosmic ray extragalactic propagation. Special attention is given to the processes involving energy losses resulting from the particles' interaction with the cosmic radiation fields as well as to the influence of the cosmic magnetic fields over the particles' trajectories in their journey from the points of injection at the sources to the detection at Earth. We quantified the role of $X_{\rm max}$ in breaking degeneracies in the parameter space of the astrophysical models used. We also extended previous analyses in the literature combining cosmic-ray energy spectrum and $X_{\rm max}$ data, performed in the absence of magnetic fields, to the case where extragalactic magnetic deflections are present.

Keywords: cosmology; astrophysics; cosmic rays; extensive air showers; Pierre Auger observatory

Resumo

Os raios cósmicos são núcleos carregados altamente energéticos que se propagam pelo espaço intergaláctico sendo as partículas mais energéticas já detectadas na Terra. Mesmo tendo sido exaustivamente estudados desde sua descoberta há mais de 100 anos, ainda existem muitas questões em aberto com respeito às fontes e mecanismos de criação e aceleração, composição química, espectro de energia, distribuição de direções de chegada, entre outras, que são o objetivo da pesquisa atual. O principal objetivo deste trabalho é explorar cenários astrofísicos de origem e propagação consistentes com os dados do espectro de energia e da profundidade atmosférica de máximo desenvolvimento de chuveiros ($X_{\rm max}$) coletados pelo Observatório Pierre Auger na região de ultra-altas energias ($E \gtrsim 10^{17.5}\,$eV) ao longo de um período de mais de 15 anos de observações. Os modelos astrofísicos foram construídos utilizando o código de Monte Carlo CRPropa para simular a propagação extragaláctica dos raios cósmicos. Especial atenção é dada aos processos que envolvem perdas de energia resultantes da interação das partículas com os campos de radiação cósmica, bem como à influência dos campos magnéticos cósmicos sobre as trajetórias das partículas em sua jornada desde os pontos de injeção nas fontes até a detecção na Terra. Quantificamos o papel do $X_{\rm max}$ na quebra de degenerescências no espaço de parâmetros dos modelos astrofísicos usados. Também estendemos análises anteriores da literatura combinando dados de espectro de energia e $X_{\rm max}$, realizados naa ausência de campos magnéticos, para o caso em que deflecções magnéticas estão presentes.

Palavras chave: cosmologia; astrofísica; raios cósmicos; chuveiros atmosféricos extensos; Observatório Pierre Auger

List of Figures

List of Tables

Contents

Chapter 1

Introduction

Cosmic rays are relativistic charged particles that, after being created and accelerated at astrophysical sources, propagate through interstellar space, becoming an essential probe for studies related to astrophysics and cosmology. The cosmic-rays energy spectrum varies in a wide energy range, going from values of $\sim$ MeV up to energies above 10^{20} eV. This range includes the so-called ultra-high energy cosmic rays (UHECRs) denomination that is given to the particles detected at the upper end of the spectrum, with energies above $\sim 10^{17.5}$ eV, a significant fraction of which is believed to have an extragalactic origin.

After gaining their high energies, cosmic rays start propagating through the intergalactic space, interacting with the radiation backgrounds as the Cosmic Microwave Background (CMB) [1, 2, 3] and the Extragalactic Background Light (EBL) [4, 5, 6]. These interactions can lead to energy loss processes that modify the initial injection spectrum at the sources, introducing new features in the detected energy spectrum that can be used to either validate or discard different proposed theoretical models of production, acceleration, and propagation of cosmic rays. For example, a usual issue of interest is the origin of an observed change in the spectral index of the detected energy spectrum known as the *ankle*, which appears around 5×10^{18} eV. This feature might be associated with a scenario of transition from a galactic component of the flux to a predominantly extragalactic one [7], but also can be explained by the way a pure extragalactic proton beam loses its energy when interacting with the CMB [8, 9, 10]. The first hypothesis suggests a chemical composition in the ankle region similar to that of the low-energy cosmic rays, while the second points to a pure proton flux.

During their journey to Earth, cosmic rays also suffer magnetic deflections in both extragalactic and galactic magnetic fields. For energies above $\simeq 10^{20}$ eV, the trajectory of a particle from the source to the point of detection can be considered almost rectilinear, thus making possible correlation studies at small angular scales aimed to identify the location of potential sources. On the other hand, particles with energies below $\simeq 10^{20}$ eV are expected to suffer large deflections, so the correlation analyses at these energies have to be limited to the search of anisotropy patterns at large angular scales as dipolar or quadrupolar.

Anisotropy studies in the distribution of the cosmic-ray arrival directions can provide information about the source spatial distribution and acceleration mechanisms, as well as the characteristics of particle propagation through the galactic and extragalactic magnetic fields. In particular, studies of anisotropies at small angular scales make it possible to identify the locations of point sources, while studies based on large angular scales can give insight into the propagation, magnetic deflection aspects, and source distribution at large scales.

The intensity of the cosmic-ray flux detected at Earth decreases rapidly with energy. In the energy region where the incoming flux is high enough, which is below $\simeq 10^{14}$ eV, direct detection is still possible by means of experiments using satellites and balloons. However, when we explore higher energy regions, the arriving flux drastically decreases to the point that the number of cosmic rays that reach Earth with energies above 10^{14} eV is about 3 particles per hour per steradian per square meter [7], making the use of direct detection techniques an extremely challenging task. Fortunately for us, when a cosmic ray energetic enough hits the top of the atmosphere it can interact with its atoms, producing new highly energetic particles which, in turn, undergo subsequent inelastic collisions generating a chain process called cascade or extensive air shower (EAS). When reaching the Earth's surface, the shower spreads over tens of square kilometers in length, which makes its detection possible using arrays of detectors disposed over large regions on the ground. Those designs are known as EAS experiments.

The largest experiment in the world designed to detect EAS originated by UHECRs is the Pierre Auger Observatory [11], located in the city of Malargüe, province of Mendoza, Argentina, which has an array of more than 1600 surface detectors spread over 3000 km^2. In addition, it counts on four optical stations located on the periphery of the array, allowing it to measure the fluorescence light emitted during the shower development. With this, the Pierre Auger Observatory has a unique hybrid design, turning it into a one of a kind experiment with privileged resources for the study of cosmic rays, especially in high-energy regions.

Although cosmic rays have been investigated for over 100 years, many of their main characteristics, especially those of the UHECRs, are not fully understood. Questions related to the peculiarities of the energy spectrum, the chemical composition, and the location of the astrophysical sources of production and acceleration of those particles are still the goal of current research in the field. The main goal of this work is to identify potential astrophysical scenarios of the origin and acceleration of UHECRs. To accomplish this, we intend to compare the predictions of different astrophysical models with the data collected by the Pierre Auger Observatory regarding energy spectrum, arrival direction distribution, and chemical composition, in order to find astrophysical scenarios consistent with the data collected so far.

The structure of the thesis is divided as follows: Chapter 2 presents an introduction to the theory of cosmic-ray physics regarding origin and acceleration by candidate sources, propagation through the intergalactic space, and detection. Chapter 3 gives an insight into the peculiarities of the Pierre Auger Observatory and the processes involving the detection and reconstruction of extensive air showers originated by UHECRs. Chapters 4, 5 and 6 contain the core of the studies

performed in this work. Chapter 4 presents studies related to large-scale anisotropy patterns of the UHECRs flux arriving on Earth. Chapter 5 explores astrophysical scenarios of extragalactic propagation in the absence of magnetic fields while in chapter 6 the studies are extended considering the extragalactic propagation of cosmic rays under the influence of different models of cosmic magnetic fields. Finally, chapter 7 presents a summary of the main results obtained in previous chapters and their potential implications.

Chapter 2

Cosmic ray physics

2.1 Definition

Cosmic Rays are commonly defined as highly energetic charged particles that propagate through interstellar space with energies ranging over ≈ 14 orders of magnitude from ~ 1 MeV to above 10^{20} eV with an overall flux composed, in general, by $\simeq 98\%$ of fully ionized nuclei and a remaining 2% of electrons or positrons. A small fraction of this cosmic-ray radiation hits the Earth's surface being the most energetic particles ever detected by humankind. The exact distribution of the arriving cosmic-ray chemical composition varies highly over the energy spectrum. However, in general terms, we can say that $\sim 90\%$ of the arriving nuclei are protons, $\sim 9\%$ are α particles and $\sim 1\%$ are heavier nuclei. The intensity of the cosmic-ray flux that hits Earth's surface decreases rapidly with energy. For energies of $\sim 10^6$ eV, they strike in a rate of $\sim 10^4$ km^{-2} s^{-1}, dropping to $\sim 10^{-7}$ km^{-2} s^{-1} (a few times a year) at 10^{16} eV and about $\sim 10^{-15}$ km^{-2} s^{-1} (less than once a century) for energies around 10^{20} eV and beyond. This is the main reason why their detection and identification, particularly in the region of ultra-high energies (above $\simeq 10^{17.5}$ eV), is a challenging task most of the time. Despite the fact that more than 100 years have passed since the cosmic-rays discovery, there are still many open questions in the field. In particular, there is no consensus on where they originated or how they are able to gain such remarkable energies. Even the chemical composition of the arriving flux at the highest energy region is still an open question. So far, cosmic rays with energies up to $\simeq 3 \times 10^{20}$ eV have been detected at Earth, which means they are about 40 million times more energetic than the highest typical values ~ 10 TeV reached in the Large Hadron Collider (LHC). For that reason, they represent matter in the most extreme departure from thermal equilibrium found anywhere in the universe and may be evidence of unknown physics or exotic particles formed in the early universe, being probably the only samples of extragalactic material that we can directly detect so far.

2.2 Discovery

The discovery and first exploration of cosmic rays began as a result of a mixture of physics and environmental studies more than a hundred years ago. After the discovery of radioactivity by Henri Becquerel in 1896, it was noticed that between 10 to 20 ions were generated per cubic centimeter of air every second. Whether or not this ionization was the product of Earth's natural radioactivity was the major question at the time. At first glance, the agent of this radioactivity was assumed to be γ rays because the two other types of known radioactive particles, namely α rays (ionized He nuclei) and β rays (electrons), were easily shielded in the experiments. In order to understand the origin of this ionizing radiation, physicists performed ionization measurements at different heights above the Earth's surface. During the decade from 1900 to 1910 several experiments confirmed the measurements of increasing ionization rates with height above the ground, which ruled out the theory of the particles as being a product of natural radioactivity because, in that case, the ionization should decay instead of increase with height.

The term *cosmic rays* was first introduced by Robert Millikan in the 1920s, who believed that those particles were γ rays with energies of 10 to 100 MeV resulting from nucleosynthesis of the common ${}^{12}_{6}\mathrm{C}$ and ${}^{16}_{8}\mathrm{O}$ elements. He proposed a theory in which cosmic rays were produced in interstellar space as by-products of the fusion of hydrogen atoms into heavier elements, and that secondary electrons were produced in the atmosphere by Compton scattering of γ rays. Jacob Clay found evidence [12], later confirmed in many experiments, that the cosmic-ray intensity increases from the tropics to mid-latitudes, which indicated that the primary cosmic rays are deflected by the geomagnetic field and must, therefore, be charged particles instead of photons.

In 1929, Bothe and Kolhörster [13] proved that cosmic rays can penetrate through heavy shields up to ~ 4.1 cm of gold, discarding Millikan's theory of such charged particles being produced by photons from interstellar fusion processes. Many expeditions were organized at high mountains to study the interactions of cosmic rays with the geomagnetic field. During the years from 1930 to 1945, a wide variety of investigations confirmed that the primary cosmic rays are indeed charged particles, protons in the majority. For example, in 1930, Bruno Rossi predicted a difference between the intensities of cosmic rays arriving from the east and west that depends upon the charge of the primary particles. This was called the "east-west effect" [14]. It was found in several independent experiments that the intensity is, in fact, greater from the west, proving that most primaries are positive [15] [16] [17]. During the years from 1930 to 1945, a wide variety of investigations confirmed that the primary cosmic rays are indeed charged nuclei [18] [19] showing that approximately 10% of the primaries are helium nuclei and 1% are heavier nuclei of elements such as carbon, iron, and lead.

2.3 Detection

The cosmic-ray flux is a steeply-falling function of energy. In the low-energy region where the rate of incidence is high enough, direct detection is possible using satellite particle detectors, or high-altitude detectors at the International Space Station. However, there are constraints in weight and size limiting the choices of these detectors, making direct detection feasible only for cosmic rays in the region of relatively low energies, below 10^{14} eV, where the flux is higher. On the other hand, indirect detection is a much more efficient technique, and it allows the detection of the most energetic particles in a region of the energy spectrum where the rate of incidence upon the Earth's surface is very low.

When an energetic enough ($\gtrsim 10^6$ GeV) primary cosmic ray reaches the atmosphere, it can interact in different ways with its atoms, producing new particles of very high energies which in turn undergo subsequent inelastic collisions, thus generating a chain process called a cascade or extensive air shower. After being triggered the shower continues its development incorporating new particles into the cascade until the energy losses due to ionization are dominant over processes involving the creation of new particles. This condition is satisfied when the average energy per particle in the cascade is about 80 MeV (the critical energy in air). At this point, the shower reaches its maximum development stage, characterized by the atmospheric depth $X_{\max}$, and can contain tens of billions of secondary particles. Upon reaching the Earth's surface, the shower can cover several tens of square kilometers in length, which makes its detection possible using sparse detectors scattered over extensive regions on the ground. After the detection of the secondary particles of the cascade, a delicate procedure is carried out in order to reconstruct the main properties of the primary particle: namely its energy, arrival direction, and chemical composition.

The study of cosmic rays is particularly challenging for the region of ultra-high energies, that is, above $\sim 10^{17.5}$ eV. In this region, the intensity of the arriving flux is approximately one cosmic ray per square kilometer per year measured on the Earth's surface. Therefore, in order to achieve good statistics, it is necessary to build large detector arrays. These designs are known as extensive air shower experiments. The Pierre Auger Observatory is the main experiment in the world specially designed for the detection of atmospheric cascades originated from UHECRs.

Although cosmic rays have been investigated for more than 100 years, many of their main properties, especially for the highest energies, are still not well established. Understanding the properties of the energy spectrum, chemical composition, location and distribution of astrophysical sources, particle production, and acceleration mechanisms among others are the goals of current research in this field.

2.4 Acceleration mechanisms

Cosmic rays with energies above 10^{20} eV have been detected since the 1960s. However, the mechanisms by which those particles are able to gain such huge amounts of energy are still one

of the most intriguing open questions in the field. It is important to remark that the power of a source potentially capable of accelerating particles up to 10^{20} eV and beyond must be extremely large. This argument can be illustrated in a general way as follows: For a particle to remain the time necessary to gain such energies, the size of the acceleration region R must be comparable to the Larmor radius of the particle in a magnetic field of strength B, which must be sufficiently weak so that synchrotron losses are not greater than the energy gain. Thus, it can then be shown that for a particle to gain an energy $\sim 10^{20}$ eV, the magnetic energy contained in the source acceleration region must be $\gg 10^{59}$ ergs. Several theoretical/phenomenological models try to solve the acceleration problem. All of them have to deal with the basic problem of how to efficiently transfer a macroscopic amount of energy to a microscopic particle.

2.4.1 Exotic top-down models

In an attempt to solve this difficulty, some theoretical models have been proposed for which the accelerator itself is suppressed and particles with energies exceeding 100 EeV [1] are not accelerated as such, but directly produced via the decay of some super-massive relic of the Big Bang or by the collapse of topological defects in the early universe. These models are known as *top-down* [20, 21, 22], and the basic idea is that these cosmic rays are produced by the decay of hypothetical extremely massive particles X, with masses M_X that can reach energies of $\sim 10^{25}$ eV [20, 21, 22]. All top-down models have two distinctive characteristics: constant injection spectra and chemical composition of the particles different from the one expected from acceleration scenarios. Although these models are theoretically interesting, there are notable disagreements between the authors regarding the particularities of such models. They also have the drawback of replacing the acceleration problem with the question of the nature and existence of such top-down sources. One of the major inconveniences of these models is the difficulty to explain the detection of a cutoff suppression in the high energy end of the spectrum, above around 6×10^{19} eV. Besides that drawback, the data collected by the Pierre Auger Observatory have established limits on the fraction of photons and on the flux of high-energy neutrinos below the top-down expectations which have strongly reduced the interest in such exotic models.

2.4.2 Acceleration in astrophysical sources

Although there is not a definitive conclusion, the failure of the top-down models to explain in a satisfactory way the main peculiarities of the detected cosmic rays has led to a consensus in the community that the acceleration of UHECRs is believed to occur in astrophysical sources by means of two main mechanisms:

- direct acceleration in an extremely intense electric field,
- and diffusive shock acceleration, based on the Fermi mechanism.

[1] 1 EeV $\equiv 10^{18}$ eV.

In the direct acceleration mechanism, the electric fields in question are often generated by rapidly rotating compact magnetized objects such as young neutron stars or a rotating accretion disk filled with magnetic fields. The details of this process and the maximum energy to which a particle can be accelerated depend on the particular physical scenario. However, for a variety of reasons, the direct acceleration mechanism is not widely favored today as the main candidate for cosmic-ray acceleration. In addition to the disagreement among authors about the crucial details of the different models, the biggest disadvantage of these mechanisms is, in general, the difficulty to obtain in a natural way the power-law shape characteristic of the detected cosmic-ray energy spectrum.

On the other hand, the stochastic acceleration mechanism was first proposed by Fermi in [23] by suggesting the interactions of charged particles with interstellar magnetized clouds. In this scenario, the particles gain their energies when being dragged by the turbulent magnetic fields present inside the clouds they traverse. In the case of non-relativistic shock velocities, the energy gain at each encounter with a magnetic cloud ξ depends, in general, on the cloud velocity $\beta = V/c$ and the relationship between the particle entry and exit angles

$$\Delta E \sim E \propto \frac{4}{3}\beta^2 \, . \tag{2.1}$$

Because the energy gain per interaction is $\xi \simeq \frac{4}{3}\beta^2$, this model is named the *second-order* Fermi acceleration mechanism, and the energy reached by the particle after n encounters with clouds is

$$E = E_0(1+\xi)^n \, , \tag{2.2}$$

where E_0 is the initial energy of the particle. The energy gain rate depends on the frequency of encounters ν:

$$\frac{dE}{dt} = \nu \Delta E = \frac{c}{\lambda}\xi E \, , \tag{2.3}$$

where λ is the main free path between encounters. Thus the acceleration time is proportional to the particle's energy, and reaching large energy values requires considerable periods of time. Although this mechanism does reproduce the power-law shape of the energy spectrum observed in the detected cosmic rays, it is not efficient enough to explain the highest energies of these particles because of the typical small values of $\beta^2 \sim 10^{-7}$ as well as the large λ values that normally exceed 1 pc.

In that sense, a much more efficient mechanism is the diffusive shock acceleration [24, 25, 26, 27], which has been extensively studied since its conception in the late 1970s. This mechanism is expected to take place near shock waves and relies on the repeated scattering of charged particles on magnetic irregularities back and forth across the magnetic clouds produced, for example, in supernova remnants. In this case, the energy gained by the particle when crossing a shock wave is proportional to $\xi \simeq \frac{4}{3}\beta$, so this mechanism is known as the *first order* Fermi mechanism. Note that the energy gain is proportional to the first power of β instead of β^2 as in the second-order Fermi mechanism. In addition, the speed of the shock waves is typically much higher than the average speed of magnetized clouds, which makes diffusive acceleration a process several

orders of magnitude more efficient. One of the main advantages of the diffusive shock acceleration mechanism is that it naturally provides an energy spectrum subject to a power law with a spectral index in the range of $2.1 - 2.4$, which is consistent with the observational data in the ultra-high energy region.

Although there is no consensus, it is currently believed that cosmic rays with energies up to about 10^{15} eV are energized by diffusive shock acceleration, with supernova explosions identified as the most likely sites. At higher energies, it is argued that the same process continues being valid but with the particles being accelerated by interaction with multiple supernova remnants as they move through the interstellar medium, by large-scale shocks from structure formation and galaxy-galaxy collisions, or by *hot spots* of radio-Galaxies. This extended acceleration may take particles up to 10^{20} eV with the heavier nuclei becoming dominant at the higher energies.

2.5 Potential sources

There is a fundamental restriction on the candidate sources potentially capable of accelerating a cosmic ray up to the highest energies which consists in the fact that the characteristic size of the acceleration region R must be greater than the Larmor radius of the particle in the source's magnetic field to make possible its permanence in the region of acceleration long enough time to gain sufficient energy. The supernova remnants in the adiabatic regime of Sedov-Taylor [28] are considered efficient cosmic-ray accelerators because part of the kinetic energy of the remnant is transformed into energy from the accelerated cosmic rays. The supernova remnants are also attractive candidates for accelerating cosmic rays because they produce magnetic fields higher than the average interstellar ones, in addition to having a large enough size and duration for the accelerated particles to reach the highest energies. Taking into account the condition mentioned above ($R_L < R$), an estimate of the maximum energy that a particle with charge Ze can reach is then expressed as a function of the shock speed β, the size of the acceleration region R and the value of the intensity of the magnetic field B as

$$E_{max} = \beta Z \left(\frac{B}{1\ \mu\text{G}}\right)\left(\frac{R}{1\ \text{kpc}}\right) \text{EeV} \ . \tag{2.4}$$

An important component of equation 2.4 is the direct dependence of the maximum energy on the particle's charge. This means that a heavy, fully ionized Ze-charged nucleus could achieve an energy Z times greater than a proton accelerated under the same conditions. Using equation 2.4 with very particular values for B and R, it is possible to reach energies up to 10^{19} eV for protons in some cases. However, achieving energies of $\sim 10^{20}$ eV is still extremely difficult. Figure 2.1 shows the well-known Hillas diagram [29] with potential candidate sources of acceleration of cosmic rays, where the maximum energy that a particle with charge Ze can reach is related to the intensity of the magnetic field and the size of the acceleration region using equation 2.4.

Possible candidates include neutron stars and other similar compact objects, large-scale shocks due to the merger of galaxies or galaxy clusters, active galactic nuclei (AGN), hot spots of type

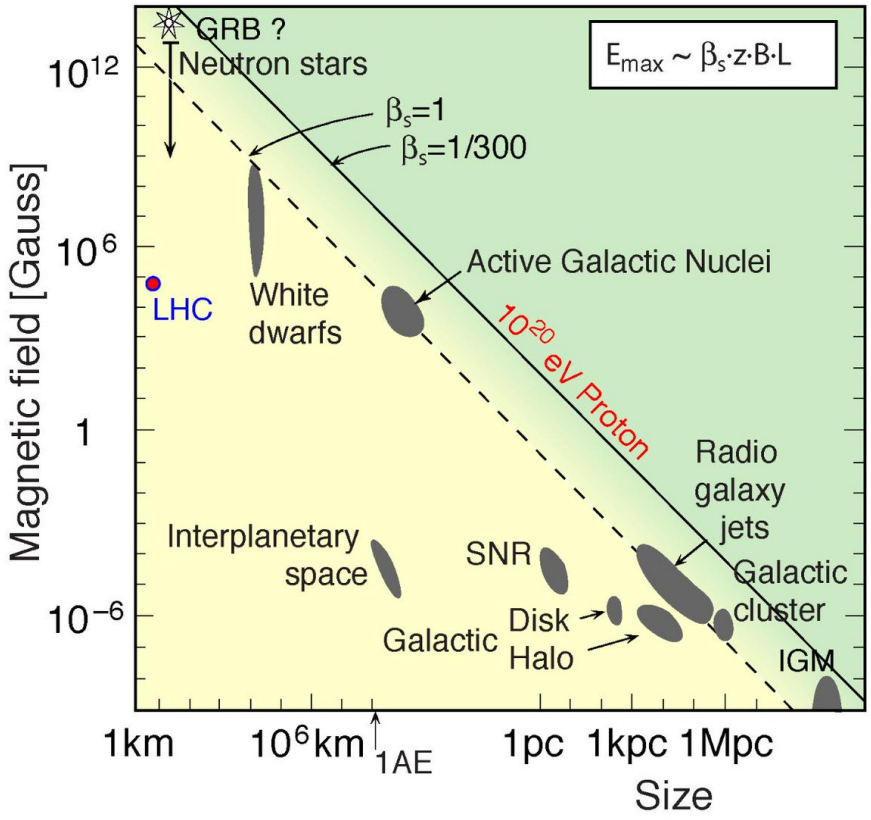

Figure 2.1: Hillas diagram relating the size and strength of the magnetic field of astrophysical objects which are candidates for sources and accelerators of cosmic rays. Objects capable of accelerating a particle above a given energy must be above the corresponding diagonal lines. Taken from [30].

II Faranoff-Riley (FR) radio-galaxies, and processes associated with gamma ray bursts (GRB). A detailed description of these objects can be found in [31]. It is worth emphasizing that Hillas' condition is necessary but not sufficient to guarantee the acceleration of a particle up to an E_{max} energy in a given source as energy losses are not considered in this model. Although most of the astrophysical systems mentioned above are capable of accelerating UHECRs up to the highest detected energies, the acceleration above 10^{20} eV is a very unlikely process that requires favorable spatial parameters and very efficient acceleration scenarios.

2.6 Extragalactic propagation

After cosmic rays are created and accelerated at the sources, they start propagating through interstellar space under the influence of magnetic and radiation cosmic fields in the regions of microwave, infrared, and radio backgrounds. The cosmic magnetic fields can produce considerable deflections in the original trajectory of the particles, making it difficult to establish any direct correlation with the initial source position. Also, in the highest energy region, the interaction of the cosmic rays with the cosmic radiation fields becomes paramount as the particles experience

significant energy losses along their trajectory, with which the detected energy spectrum at Earth can differ considerably from the original injection spectrum at the source.

2.6.1 The Greisen-Zatsepin-Kuz'min cutoff

The dominant radiation background in the interstellar medium is the CMB, with a peak energy of $\sim 6 \times 10^{-4}$ eV and a density of ~ 400 photons cm^{-3}. Shortly after the discovery of the CMB, Greisen, Zatsepin and Kuz'min [32, 33] predicted a sharp suppression in the cosmic-ray proton spectrum around 5×10^{19} eV as a result of the energy losses suffered by the high energetic protons due to the interaction with the CMB photons via production of pions. Since then, this phenomenon became known as the GZK cutoff or GZK effect. While the suppression was initially predicted for protons, the GZK effect is present, although by different mechanisms, also for heavier nuclei. In the case of heavier nuclei, the dominant process responsible for the energy losses is nuclear disintegration due to interaction with EBL photons. This phenomenon would lead to a cutoff in the cosmic-ray spectrum and even if the particles were accelerated to higher energies, they would not be able to survive the travel of large distances from their sources without losing a significant fraction of their energies. Because of the rapid decrease in the mean free path of UHECRs when their energies reach the threshold for production of pions or nuclear photodisintegration, in the case of protons or heavier nuclei respectively, one expects that above this energy the flux measured on Earth will be dominated by relatively close sources, at distances $\lesssim 200$ Mpc. This distance is known as the GZK horizon and is heavily dependent on energy.

2.6.2 Photoproduction of pions

The main reactions resulting from the interaction of protons with the CMB are

$$\begin{aligned} p + \gamma_{CMB} &\rightarrow p + \pi^0 && (2.5) \\ &\rightarrow n + \pi^+ \\ &\rightarrow p + e^+ + e^- \ . && (2.6) \end{aligned}$$

In nuclear reactions, the threshold for the production of secondary particles is determined by the energy that equals the mass of all the products in the center-of-mass frame. The proton energy at which the production of pions starts to be possible (eq. 2.5) can be obtained using the equation

$$s = m_p^2 + 2E_p E_\gamma \left(1 - \beta_p \cos\theta\right) \ , \tag{2.7}$$

where s is the square of the center of mass energy $\sqrt{s} = m_p + m_\pi$, E_p and E_γ are the energies of the proton and the photon, respectively, and θ the angle between them. In the particular case of co-linear collisions ($\cos\theta = -1$) and using the average energy of the CMB photons today ($E_\gamma^{CMB} \simeq 6.34 \times 10^{-4}$ eV), the energy threshold for this reaction becomes

$$E_p = \frac{m_\pi}{4E_\gamma}(2m_p + m_\pi) \simeq 10^{20} \text{ eV} \ . \tag{2.8}$$

In a similar way, the photon energy threshold in the proton rest frame can be calculated as follows

$$E'_\gamma = m_\pi \left(1 + \frac{m_\pi}{2m_p}\right) \simeq 145 \text{ MeV} . \tag{2.9}$$

Another important energy loss process involving highly energetic protons is the production of electron-positron pairs (eq. 2.6) [34]. The proton energy threshold for this process is much lower since only the rest energy of two electrons need to be added to the proton in the center-of-mass frame. For co-linear collisions, this energy threshold is about 4×10^{17} eV.

The mechanism of energy loss through pair production differs significantly from the one of photopion production. The first one is a quasi-continuous process since the energy loss for each pair created ($\sim 1\%$) is very small in the region where this process is dominant ($\sim 10^{18} - 10^{20}$ eV). On the other hand, the photo-production of pions is a stochastic and resonant process with large energy losses in each collision. In the energy region above 6×10^{19} eV, where this process becomes dominant over pair production, the energy losses in each interaction are $\approx 20\%$ of the cosmic-ray energy.

2.6.3 Nuclear photodisintegration

Nuclei heavier than protons suffer energy losses via pair production and photodisintegration processes [34, 35], where now the important radiation field becomes the EBL:

$$\begin{aligned} A + \gamma_{EBL} &\rightarrow (A-1) + N & (2.10)\\ &\rightarrow (A-2) + 2N \\ &\rightarrow A + e^+ + e^- & (2.11) \end{aligned}$$

where N represents an emitted nucleon, namely a proton or neutron. Photodisintegration occurs because the low-energy photons in the EBL are capable to excite a collective mode of nuclear oscillation, known as giant dipole resonance, which leads to nuclear disintegration via nucleon emission [36]. The main channels resulting from this interaction are $(\gamma,\ n)$ and (γ, p). The energy-loss rate via double-nucleon emission such as $(\gamma,\ 2n)$, $(\gamma,\ np)$, or $(\gamma,\ 2p)$ is about one order of magnitude lower than that via single-nucleon emission. Although a nucleus does not disintegrate via pair creation, it loses energy and there is a significant effect on the energy loss rate, most notably in the region between 5×10^{19} eV and 2×10^{20} eV.

2.6.4 Energy loss length

The mean energy loss length (ELL) is a measure of the traveled distance at which a particle loses its energy and is defined as

$$L_{loss} = \frac{E}{dE/dx} = \frac{\lambda(E)}{K_{inel}(E)} , \tag{2.12}$$

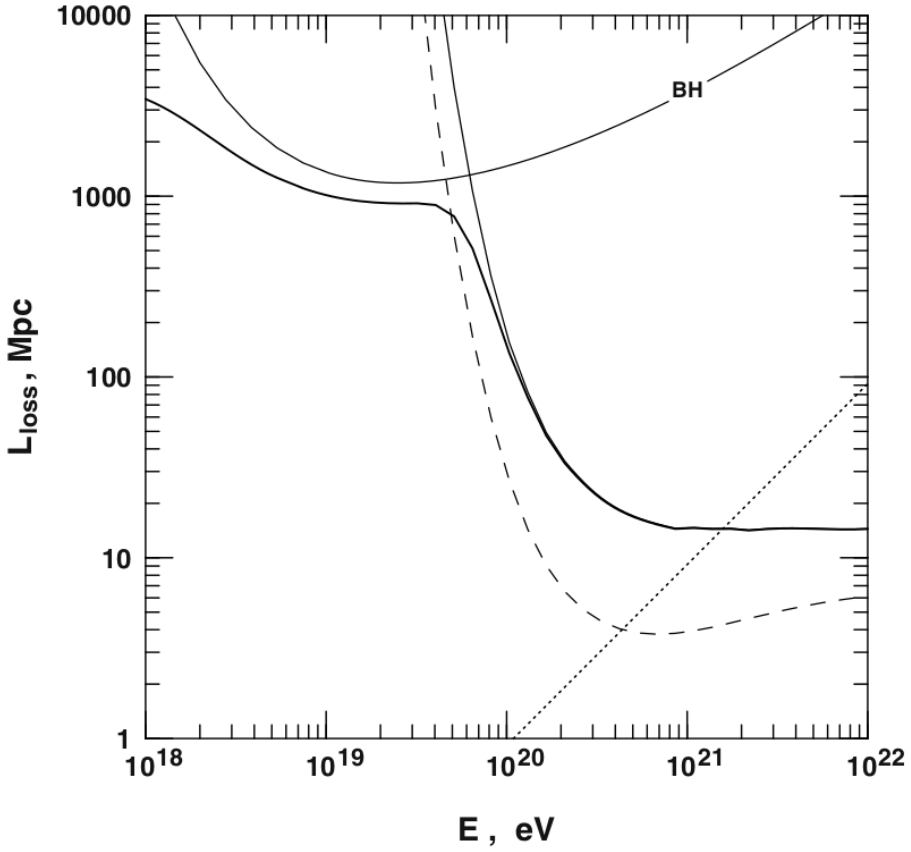

Figure 2.2: Energy loss length as a function of the energy for protons (thin continuous lines) due to photoproduction of pions and pair production (BH). The total ELL is shown by the thick line. The dashed line shows the proton interaction mean free length in the CMB $\lambda_{p\gamma}$, and the dotted one represents the neutron decay length. Taken from[31].

where the particle inelasticity K_{inel} represents the energy fraction lost by interaction and $\lambda(E)$ the mean free path between interactions.

Figure 2.2 shows the energy loss length due to the photoproduction of pions and pair production. For energies above 10^{20} eV, the photoproduction process dominates, and above 8×10^{20} eV, the ELL is almost constant at about 15 Mpc. Below about 5×10^{19} eV, the energy losses for protons are dominated by the creation of electron-positron pairs, and the ELL reaches a minimum at $\sim 2 \times 10^{19}$ eV. At the lowest energy region, the ELL tends to become constant and equal to the adiabatic energy loss that takes place as a consequence of the Universe's expansion. For the Einstein-de Sitter model of a flat, matter-dominated Universe, the current adiabatic energy loss length is [31]

$$L^{ad}_{loss}(z=0) = \frac{c}{H_0} \simeq 4000 \text{ Mpc} . \tag{2.13}$$

The redshift dependence of the adiabatic ELL in this model is

$$L^{ad}_{loss}(z) = L^{ad}_{loss}(z=0)(1+z)^{-3/2} . \tag{2.14}$$

For the particle production processes, the ELL scales differently with redshift because of

the additional changes in the energy and number density of the photon field. In this case, the dependence with redshift is

$$L_{loss}(E_p, z) = (1+z)^{-3} L_{loss}[(1+z)E_p, z=0] \; . \tag{2.15}$$

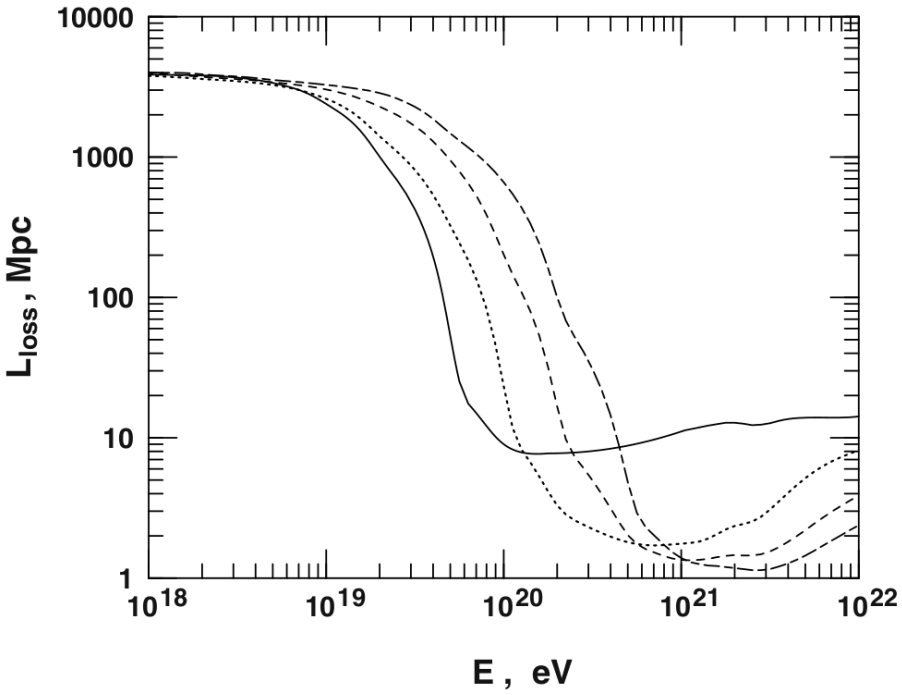

Figure 2.3: Energy loss length as a function of the total energy of the nuclei, due to photodisintegration, pair production, photoproduction, and adiabatic expansion processes combined, for nuclei of He (solid), O (dots), Si, (dashes) and Fe (dash-dash).Taken from [31].

Figure 2.3 shows the ELL for some nuclei heavier than H due to photodisintegration, pair production, and adiabatic expansion calculated as

$$\frac{1}{L_{loss}^{tot}} = \frac{1}{L_{loss}^{A+\gamma,N}} + \frac{1}{L_{loss}^{A+\gamma,e^+e^-}} + \frac{1}{L_{loss}^{ad}} \; . \tag{2.16}$$

As we can see from figure 2.3, below a total nucleus energy of about $\sim 10^{19}$ eV, the extremely high values of $L_{loss} \simeq 3 \times 10^3$ Mpc implies that if only the photodisintegration and pair production processes are considered, the energy losses are negligible below this value. That happens because the nucleon energy in any case is below the pair production threshold. As the energy increases above $\sim 10^{19}$ eV, the nuclei start undergoing pair production and disintegration losses. For He nuclei, the minimum ELL of about 8 Mpc is reached at energies between 1×10^{20} and 2×10^{20} eV. At that point, the photoproduction losses start being dominant over the pair production and the energy loss length at high energies approaches 15 Mpc, the same as for protons. With the increasing mass of the nuclei, the thresholds for all these processes also increase and, at the same time, the minimum ELL decreases. The minimum ELL for O nuclei is reached at $\sim 7 \times 10^{20}$ eV and is less than 2 Mpc. In the case of iron, the minimum ELL which is $\gtrsim 1$ Mpc, is reached at

energies above 10^{21} eV. In conclusion, we can summarize that nuclei lose their energy even faster than protons, and with the increase of the mass, the energy losses start being significant at higher energies.

2.7 Galactic propagation

The characteristic radius of our galaxy is about 20 kpc, which is several orders of magnitude smaller than the minimum ELLs. For this reason, UHECRs do not suffer significant energy losses during their propagation in the confines of the galaxy. However, they are deflected in the galactic magnetic field and therefore the most important effect on the propagation of cosmic rays within the galaxy is the influence of the magnetic field on the trajectory of the particles. Several models have been proposed for the description of the galactic magnetic field [37, 38], the most up-to-date being the JF12 model [39, 40]. Nonetheless, there is still no consensus on the definitive model. In general, the magnetic field in our galaxy can be described by a regular component on large scales $\mathbf{B}_0$ in addition to a small-scale random component $\mathbf{B}_r$ attributed to turbulence in the interstellar plasma. The characteristics of the propagation of cosmic rays of galactic origin under the action of these fields can be obtained from the solution of the diffusion equation for the stationary case

$$\nabla \cdot \mathbf{J}(\mathbf{x}) = Q(\mathbf{x}) \ , \tag{2.17}$$

where $Q(\mathbf{x})$ is the rate of production of cosmic rays per volume unit in the sources, and $\mathbf{J}(\mathbf{x})$ is the current density related to the space density of cosmic rays $N(\mathbf{x})$ by [41]

$$\mathbf{J} = -D_\perp \nabla_\perp N - D_\parallel \nabla_\parallel N + D_A \mathbf{b} \times \nabla N \ . \tag{2.18}$$

Here, $\mathbf{b} = \mathbf{B}_0/|\mathbf{B}_0|$ is the unit vector in the direction of the regular magnetic field, $\nabla_\parallel = \mathbf{b}(\mathbf{b} \cdot \nabla)$ and $\nabla_\perp = \nabla - \nabla_\parallel$. $D_\parallel$ and $D_\perp$ are the diffusion tensor components in the directions parallel and perpendicular to the regular magnetic field, respectively, while the D_A coefficient is related to the anti-symmetric part of the tensor.

The deflection angle α of a particle with charge Ze and energy E when traveling a distance d is typically of the order $\alpha \sim d/r_L$, where $r_L = E/ZeB$ is the Larmor radius. The Larmor radius increases with the energy of the particles, and with this the probability of the particles escaping from the confinement region. Studies carried out in [42, 43, 41] show that the changes in the spectral index of the cosmic-ray energy spectrum, known as the knee and second knee (2.8) can be explained by a change in the escape mechanism of the galaxy of proton and iron components, respectively, in a scenario where the propagation regime makes a transition from transversal diffusion to a regime dominated by drift effects.

In [44], the effects of magnetic field turbulence on the anisotropy of the highest energetic galactic cosmic rays were investigated. It has been found that if the flux of cosmic rays for energies above 10^{18} eV is composed predominantly of galactic protons, even if a halo of a turbulent magnetic field is assumed beyond the regular and turbulent galactic magnetic fields across the disk, a strong

anisotropy is expected around 10^{19} eV. This result is in contradiction with the main observations that show anisotropies smaller than 10% for the particles of these energies.

Regular magnetic fields deflect the trajectories of cosmic rays causing a flux variation in certain directions, known as the lensing effect [45, 46]. As a consequence of its dependency on the particle's energy, lensing can significantly affect the cosmic-ray energy spectrum observed on Earth. In addition, for sources located in a large fraction of the sky, cosmic rays can reach the Earth following different paths and, therefore, multiple images of a single source can be formed, and time delays in the arrival of particles coming from the same source can occur. Also, the observed composition of cosmic rays can be affected by the lensing effect. Due to the dependence of the amplification of the flux with E/Z, the flux of nuclei with different atomic numbers is amplified in different proportions for the same energy. Magnetic lensing effects are significant for cosmic rays with energies in the range $10^{18} \lesssim E/Z \lesssim 5 \times 10^{19}$ eV. However, any accurate prediction depends on the particular magnetic field model adopted.

2.8 Energy spectrum

The detected flux of cosmic rays as a function of energy, also called energy spectrum, can be represented for several orders of magnitude as a power law, $\frac{dN}{dE} \propto E^{-\gamma}$. The spectral index γ can present several variations along the energy range producing the peculiar features of the spectrum. The shape of the detected cosmic-ray energy spectrum, over a wide range of energies, is shown in figure 2.4. For energies right above 10^{11} eV, the spectral index takes a value of $\gamma = 2.7$. A first change known as the knee appears around $E_{knee} \simeq 3 \times 10^{15}$ eV, where the spectral index increases to $\gamma = 3$. A further increase in the spectral index known as the second knee occurs for energies around $\simeq 4 \times 10^{17}$ eV, where γ reaches a value of 3.3. Figure 2.5 shows the shape of the cosmic-ray spectrum measured by the Pierre Auger Observatory in the ultra-high energy region, where two distinctive features stand out. First, the appearance of the so-called ankle for energies around $\simeq 5 \times 10^{18}$ eV, where γ decreases to a value of ≈ 2.5. Second, the strong suppression of the flux that is observed for energies greater than $\simeq 5 \times 10^{19}$ eV. In general, the possible interpretations of the spectrum features consider changes in the mechanisms of acceleration at sources, propagation effects, and dependence on the energy of the cross sections of hadronic interactions [30].

2.8.1 The knee

There are three main scenarios that try to explain the appearance of the knee. First, it could be a characteristic generated by the limit on the maximum energy that can be provided by the cosmic-ray accelerators in the galaxy. More precisely, the maximum energy that the particle can reach will depend on how long it remains confined in the acceleration region, that is, as long as its Larmor radius r_L is smaller than the typical size of the region, with which the maximum energy will be proportional to the charge of the particle. Another possible explanation for the

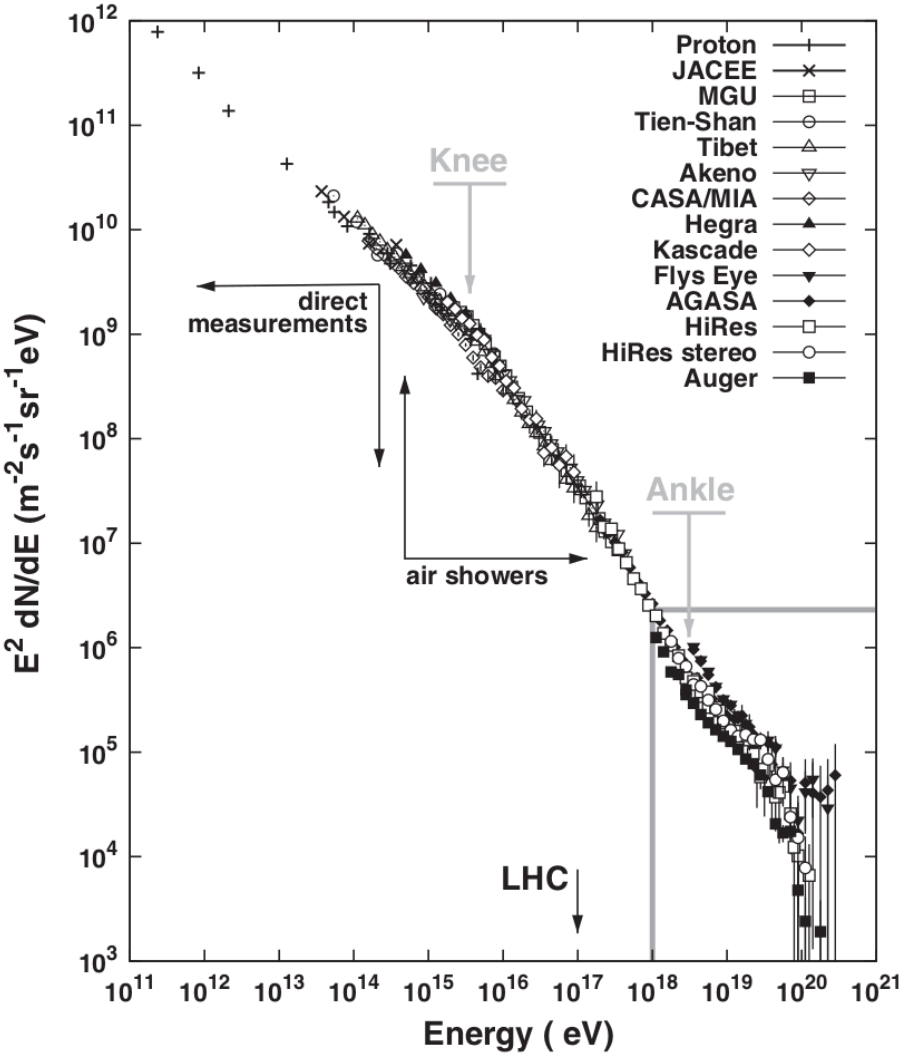

Figure 2.4: Cosmic rays energy spectrum above 10^{11} eV. For energies below $\simeq 10^{14}$ direct particle detection is possible. For energies above 10^{14} eV experiments are required for the indirect detection of cosmic rays as EAS. Taken from [7].

knee may be a change in the diffusion regime in the galactic magnetic field, giving rise to a loss of confinement of galactic protons: accelerated protons in the Milky Way can become energetic enough to overcome the confinement of the magnetic galactic field [42].

Another region of the cosmic-ray spectrum with less well-established characteristics, known as the second knee, appears around 4×10^{17} eV [47]. The second knee position is $\simeq 26 \times E_{knee}$, which may be an indicator that both knees have the same physical origin, with protons being the dominant component of the flux at the region of the first knee and iron ($Z = 26$) at the second one. The knees would then have a dependence on magnetic rigidity $R = E/Z$ with which a knee for each type of nuclei would be expected.

2.8.2 The ankle

Figure 2.5 shows the UHECRs energy spectrum measured by the Pierre Auger Observatory and the apparition of the ankle can be seen around $\simeq 10^{18.7}$ eV. As shown in figure 2.5, for energies above $10^{17.5}$ eV the energy spectrum $J(E) = dN/dE$ can be described using two different parameterizations as follows

$$J(E) = \begin{cases} J_0 \left(\frac{E}{E_{ankle}}\right)^{-\gamma_1} & (E \leq E_{ankle}) \\ J_0 \left(\frac{E}{E_{ankle}}\right)^{-\gamma_2} \left[1 + \left(\frac{E_{ankle}}{E_s}\right)^{\Delta\gamma}\right] \left[1 + \left(\frac{E}{E_s}\right)^{\Delta\gamma}\right]^{-1} & (E > E_{ankle}) \ , \end{cases} \tag{2.19}$$

where E_{ankle} is the energy at which the dip known as the *ankle* appears, $E_s = (39 \pm 2\,[\text{stat.}] \pm 8\,[\text{syst.}])$ EeV is the energy at which the suppression of the flux begins to take place, $E_{1/2} = (23 \pm 1\,[\text{stat.}] \pm 4\,[\text{syst.}])$ EeV is the energy at which the integral spectrum drops by a factor 2 below what would be the expected in a scenario without steepening, $\Delta\gamma = 2.5 \pm 0.1\,(\text{stat.}) \pm 0.4\,(\text{syst.})$, $\gamma_1 = (3.293 \pm 0.002\,[\text{stat.}] \pm 0.05\,[\text{syst.}])$ and $\gamma_2 = (3.53 \pm 0.02\,[\text{stat.}] \pm 0.5\,[\text{syst.}])$ are the spectral indexes below and above the ankle, respectively.

The most accepted explanation for the appearance of a spectral break in this region is the transition from a purely galactic component of the cosmic-ray flux to an extragalactic one, with the energy at which this transition takes place equal to E_{trans}. There are different models for this transition, leading to a different chemical composition for the flux of UHECRs around the ankle [48] so that knowledge of this region of the spectrum is of major importance to understanding the origin of the cosmic rays at these energies. The two most popular models will be presented and discussed briefly below with the available experimental evidence to explain the behavior of the cosmic-ray flux in the transition region.

2.8.2.1 Model with a transition at the ankle

In this model [10], the appearance of the ankle is assumed to be the product of the intersection of the galactic and extragalactic components of the flux, described by power laws proportional to $E^{-3.5}$ and $E^{2.3}$, respectively. Being the total flux the sum of the two components. The main characteristics of this scenario are:

- Heavy composition for energies below the ankle, since nuclei with high rigidity are the ones that achieve the largest energies in galactic accelerators.
- Anisotropies below the transition region, due to the anisotropic distribution of galactic sources and the loss of confinement in the galaxy. On the other hand, extragalactic flux is expected to be highly isotropic.

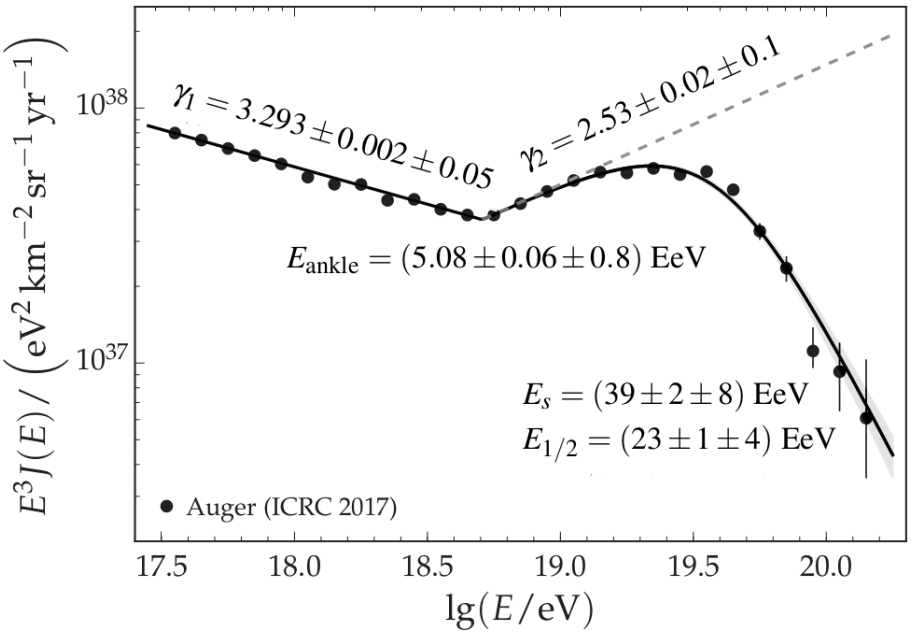

Figure 2.5: UHECRs energy spectrum measured by the Pierre Auger Observatory. The spectral breakdown known as the ankle is observed for energies around 5×10^{18} eV and the abrupt suppression of the flux is observed above $\sim 5 \times 10^{19}$ eV. Taken from [49].

2.8.2.2 Pair production model

In this scenario, also known as dip model [9], the galactic-extragalactic transition occurs around the energy of the second knee and is essentially completed at the energy of 1 EeV. The extragalactic flux above this energy is assumed to be a pure proton flux, and the ankle is explained by a dip in the extragalactic spectrum caused by energy losses due to pair creation in the interaction of highly energetic protons with the cosmic microwave background. The main predictions of this model are:

- Change of the dominant chemical composition in the second knee region: from iron nuclei with galactic origin to extragalactic protons.
- Absence of anisotropies for energies above 1 EeV.
- Spectral shape and position of the dip created by the protons.

At energies greater than 5×10^{19} eV, an abrupt suppression of the flux is observed with great statistical significance [50]. In the case of protons being the dominant species of particles in this region, such suppression is naturally explained by the GZK effect, mentioned in section 2.6.1. However, this suppression can also be the result of cosmic-ray sources reaching their acceleration limits at these energies.

2.9 Large scale anisotropies

The distribution of the arrival directions of cosmic rays is an important observable in an attempt to understand their origin and nature since it is closely linked to the spatial distribution of the sources. Above the GZK cutoff, the high magnetic rigidity of UHECRs implies moderate angular deviations ($\sim$ degrees), so that correlation studies with point sources are still possible. In fact, the typical deflection value for a particle with charge Ze, when propagating a distance D in the presence of a regular magnetic field of intensity B, is given by

$$\delta \simeq 2.7^{\circ} \frac{60 \text{ EeV}}{E/Z} \left| \int_0^D \left(\frac{d\mathbf{r}}{\text{kpc}} \times \frac{\mathbf{B}}{3\,\mu\text{G}} \right) \right| , \tag{2.20}$$

and in a turbulent field, with coherence length L_c and field RMS $B_{\text{rms}} = \sqrt{\langle B^2(\mathbf{x}) \rangle}$ it is

$$\delta \simeq 4^{\circ} \frac{60 \text{ EeV}}{E/Z} \frac{B_{\text{rms}}}{10^{-9}\text{G}} \sqrt{\frac{D}{100\,\text{Mpc}}} \sqrt{\frac{L_c}{1\,\text{Mpc}}} \, . \tag{2.21}$$

At lower energies, however, any correlation at small angular scales is destroyed by the influence of magnetic fields, of both galactic and extragalactic origin, so studies of anisotropy should be limited to the search for patterns that extend across regions of appreciable size in the sky. The large-scale anisotropy studies are a valuable source of information to understand the peculiarities of the origin and nature of UHECRs. For example, in relation to the controversial question of the ankle region, it is possible to explain this characteristic of the spectrum as a signature of the transition from a galactic to an extragalactic component of the UHECRs flux which would lead to the appearance of a dipolar pattern in the arrival distribution measured at Earth [51]. Another possible interpretation of the ankle is the distortion of an extragalactic spectrum dominated by protons that suffer energy losses due to the production of $e^{\pm}$ pairs by the interaction with photons of the CMB [9]. In this scenario, one would expect the appearance of a dipolar pattern in the cosmic-ray distribution, with an amplitude of $\sim 0.6\%$ [52], as a consequence of the Compton-Getting effect (see 2.9.1) due to the movement of the Earth within the rest frame of the CMB.

2.9.1 Compton-Getting effect

The relative movement of the detector with respect to a reference frame in which the distribution of cosmic rays is a priori isotropic produces the appearance of a spurious anisotropy in the measured cosmic-ray flux. This phenomenon is known as the Compton-Getting effect [52]. If a cosmic-ray detector moves with a speed v_{det}, it will experience an excess in the particle detection in the direction of movement together with the deficit in the opposite direction. Both effects will lead to the appearance of a dipolar pattern in the distribution of arrival directions of the cosmic rays measured by the moving detector. In a first-order approximation, the magnitude of the expected dipole amplitude d can be estimated simply by taking the ratio of the speed of the detector to the speed of light $d \sim v_{det}/c = \beta$. The exact expression is derived making an analogy with the

relativistic Doppler effect [52, 53]:

$$d \approx (\gamma + 2)\beta \,, \tag{2.22}$$

where γ is the spectral index of the cosmic-ray flux.

In order to calculate the dipole amplitude in a specific scenario, it is necessary to know in which frame of reference the distribution of cosmic rays is assumed to be isotropic. With this in mind, the problem can be reduced to calculate the relative speed between the detector and that frame. On the other hand, the observation of a dipole of a given amplitude and direction can also be useful to either exclude or confirm certain scenarios. The following are three of the most realistic scenarios that can lead to the appearance of the anisotropies described by the Compton-Getting effect.

2.9.1.1 Galactic Compton-Getting

At relatively low energies ($\sim 10^{17}$ eV), cosmic rays are mainly of galactic origin and are trapped for a long time in the magnetic field of the galaxy. Therefore, their arrival directions are randomized by the turbulent magnetic fields. However, in the hypothesis of the cosmic-ray radiation being isotropic in the galactic frame, the movement of the solar system relative to the galactic center would create a dipole in the measured distribution of UHECRs [54]. In this case, the relative speed of the detector coincides with the speed of the solar system $v_{det}^{sun} = 200$ km/s in the direction $(\alpha,\ \delta) = (270°,\ 30°)$ in equatorial coordinates, which together with the value of the spectral index in the region above the knee ($\gamma = 3.3$) leads to the appearance of a dipole anisotropy of amplitude $d_{gal} \approx 0.35\%$ in this direction. In the case of galactic cosmic rays rotating around the galactic center at the same speed as the solar system, the over-density of UHECRs arriving from the direction of travel is partially decreased leading to a decrease in the dipole amplitude of approximately an order of magnitude, generated essentially by the Earth's movement around the Sun.

2.9.1.2 Extragalactic Compton-Getting

For energies $\gtrsim 10^{18}$ eV, the appearance of an anisotropy pattern produced by the movement of our galaxy across intergalactic space is known as the extragalactic Compton-Getting effect [54]. In this case, the reference system where the cosmic rays are assumed to be isotropic coincides with the rest reference system of the Great Attractor. The relative speed of the detector with respect to the Great Attractor is given by the sum of the relative velocity of the Milky Way with respect to the referential of the Great Attractor, which is of $v_{det}^{gal} \approx 630$ km/s in the direction $(\alpha,\ \delta) = (241°,\ 61°)$, plus the above-mentioned speed of the solar system with respect to the galaxy v_{det}^{sun}, giving rise to a total relative velocity $v_{det}^{tot} \approx 800$ km/s in the direction $(\alpha,\ \delta) = (251°,\ 54°)$, with which a dipole anisotropy of amplitude $d_{ext} \approx 1.3\%$ in this direction is expected as a consequence of the movement of the galaxy in extragalactic space.

2.9.1.3 Cosmological Compton-Getting

A second scenario known as the cosmological Compton-Getting effect [53] takes place for energies around the ankle, a situation in which the reference system where cosmic rays are assumed isotropic coincides with the CMB resting frame. In this case, the relative speed of the solar system with respect to the CMB resting frame can be calculated from the detected dipolar anisotropy in the distribution of the CMB radiation [55], giving rise to a speed of $v_{det}^{CMB} \approx 370$ km/s in the direction $(\alpha,\ \delta) = (168°,\ -7°)$. Considering the spectral index $\gamma = 2.7$ for this energy region, the effect leads to an expected dipole amplitude of $d_{\rm CMB} \approx 0.6\%$ in this direction.

2.9.2 Influence of galactic magnetic fields

In case there is an anisotropy in the primary distribution, the influence of magnetic fields, both galactic and extragalactic, in the trajectory of cosmic rays during their propagation can lead to the appearance of anisotropic patterns in large angular scales in the distribution of the arrival directions of particles at Earth. In any case, the predictions depend on the peculiarities of the adopted magnetic field model, the chemical composition of the incident particles, as well as the spatial distribution of the sources. The dipolar amplitude associated with the galactic component of the flux is given by

$$\mathbf{d} = \frac{3}{c}\frac{\mathbf{J}}{N}\,, \tag{2.23}$$

where $\mathbf{J}$ is the current of galactic cosmic rays and N the total density (galactic plus extragalactic). Figures 2.6 and 2.7 show the expected dipolar amplitudes and right ascension orientation for the main galactic cosmic-ray components, computed in [41] using a model for the galactic magnetic field with axial symmetry around the galactic center (with respect to the galactic plane) and a regular component of amplitude $B_{\rm rms} = 1\mu$ G oriented along the z-axis. The sources are distributed in a cylindrical ring of inner radius $r_{in} = 3$ kpc and outer radius $r_{out} = 6$ kpc.

The lensing effect of the magnetic field can also cause anisotropies to appear in the arrival direction distribution of cosmic rays [45]: the coherent part of the field could lead to a focus of extragalactic UHECRs producing an excess in the magnitude of the flux measured in certain directions, which, in turn, could induce a dipolar anisotropy pattern. The amplitude and direction of the dipole depend strongly on the model used to describe the galactic magnetic field. The hypothesis of a single and powerful source of cosmic rays can also result in an anisotropy pattern that can be described at first approach by a dipole. Assuming that the injection spectrum of cosmic rays at the sources decreases rapidly with energy, similar to the detected energy spectrum on Earth, the following considerations can be made:

- In the first place, the particles of the highest energies would be deflected weakly by the magnetic fields so that their arrival directions would point in good measure to the source.
- Second, most UHECRs that are concentrated in the lowest energies in the spectrum would be subject to major deflections by magnetic fields, with an angular distortion increasing

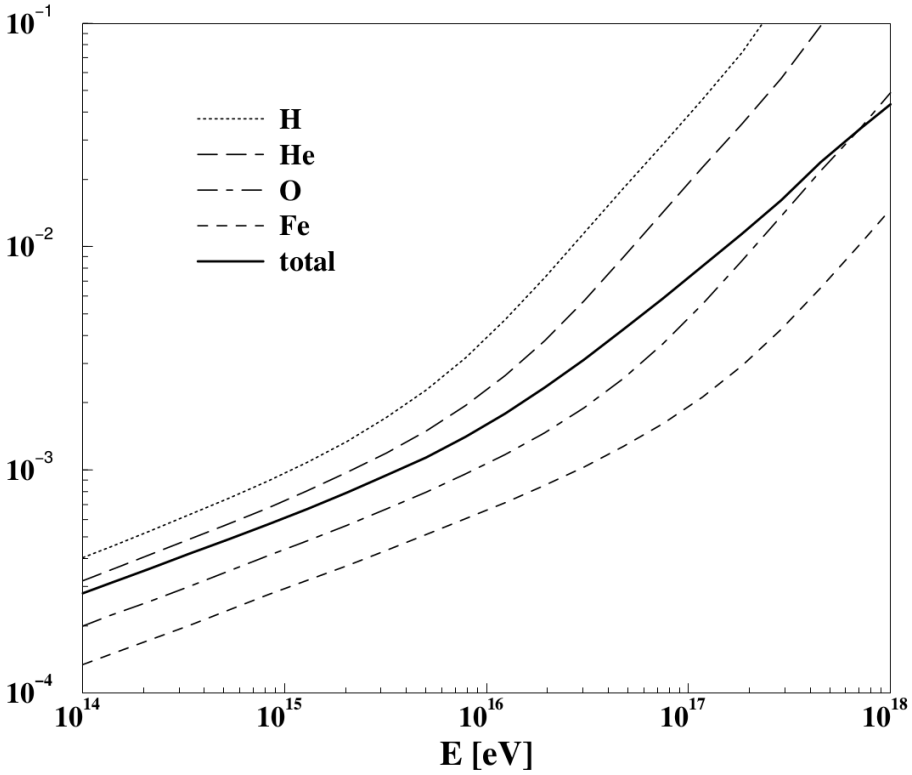

Figure 2.6: Dipolar anisotropy amplitudes as a function of energy corresponding to the main galactic CR components (H, He, O and Fe) compared to the total (galactic plus extragalactic) expected anisotropy. Taken from [41].

with the decrease of the particle energy, this would lead to a great scattering around the source of the arrival directions measured at Earth, which may result in the appearance of a dipolar pattern.

2.9.3 Influence of extragalactic magnetic fields

The influence of extragalactic magnetic fields on the propagation of cosmic rays can also produce anisotropic patterns in the arrival direction distribution measured at Earth. In [56] and [57], the authors studied the anisotropies produced by the diffusion of ultra-high energy cosmic rays from nearby extragalactic sources in turbulent magnetic fields outside the galaxy using simulations of the trajectories of protons and heavier nuclei. The evolution of the direction of propagation $\hat{n}$ of particles with charge Ze in the turbulent field was followed by integrating the Lorentz equation.

In general, large dipole amplitudes are expected in any case for energies above 1 EeV when a single cosmic-ray source is considered. However, in a more realistic situation, the total cosmic-ray flux probably originates from a set of multiple sources. The total dipolar component of the flux will then depend mainly on the location and the intensities of the nearby sources and whether there is a non-homogeneous distribution of sources on large scales. If the sources themselves have a non-homogeneous distribution around the observer, in particular a dipolar one, an additional

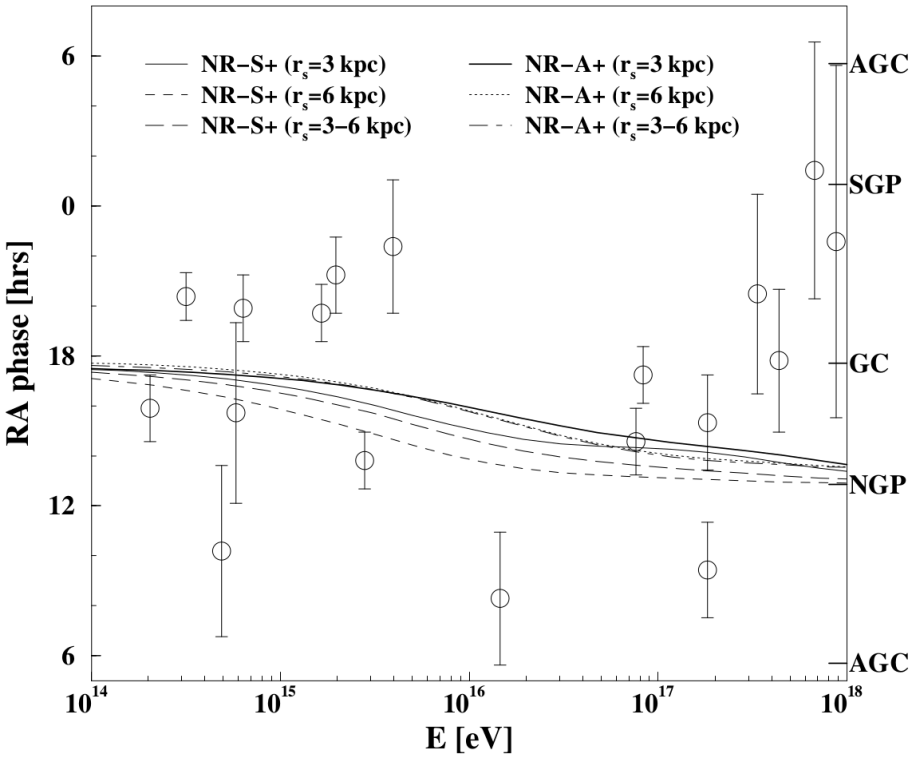

Figure 2.7: Phase of the dipole first harmonic in right ascension as a function of energy corresponding to the main galactic CR components (H, He, O and Fe) obtained using different models of the galactic magnetic field and source distributions. For comparison, experimental data measured by different experiments are also shown. The labels on the right indicate the directions of maximum CR intensity (GC-Galactic Center, AGC-Anti Galactic Center, NGP-North Galactic Pole, SGP-South Galactic Pole), considering that the dipolar amplitude δ is contained in the $r-z$ plane. Taken from [41].

contribution to the dipole amplitude of the observed anisotropy is expected.

As can be appreciated in figure 2.8, particles with a lower atomic number produce larger anisotropy at the same energy. This is because, due to their greater rigidity, they suffer fewer deflections than particles with a greater atomic number. It also can be seen that the greater the sources' number density, the smaller the anisotropies since the relative contribution to the total flux from each source decreases. Figure 2.9 shows the amplitudes and dispersion of the dipolar anisotropies expected for a flux composed of particles of different chemical species propagating in an extragalactic magnetic field of $B_{\rm rms} = 1$ nG, in a scenario in which the flux of accelerated cosmic rays is a mixture of proton, helium, carbon, silicon, and iron, obtained for a homogeneous distribution of sources with a density $\rho = 10^{-5}$ Mpc^{-3} and a distribution according to the 2MRS catalog [58], which presents a dipolar pattern. It can be seen that the 2MRS non-homogeneous distribution of sources produces a relative increase in the predicted dipole amplitude by a factor of ~ 2 compared to the case of a homogeneous source distribution.

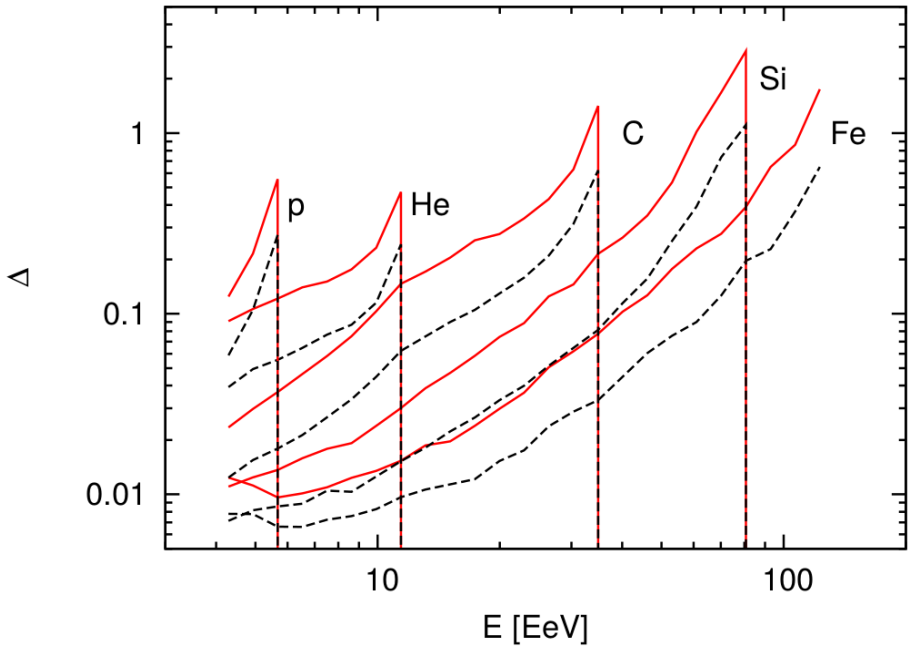

Figure 2.8: Expected dipole amplitude for H, He, C, Si, and Fe nuclei for a homogeneous distribution of sources with densities of 10^{-5} Mpc^{-3} (solid red lines) and 10^{-4} Mpc^{-3} (black broken lines). Taken from [57].

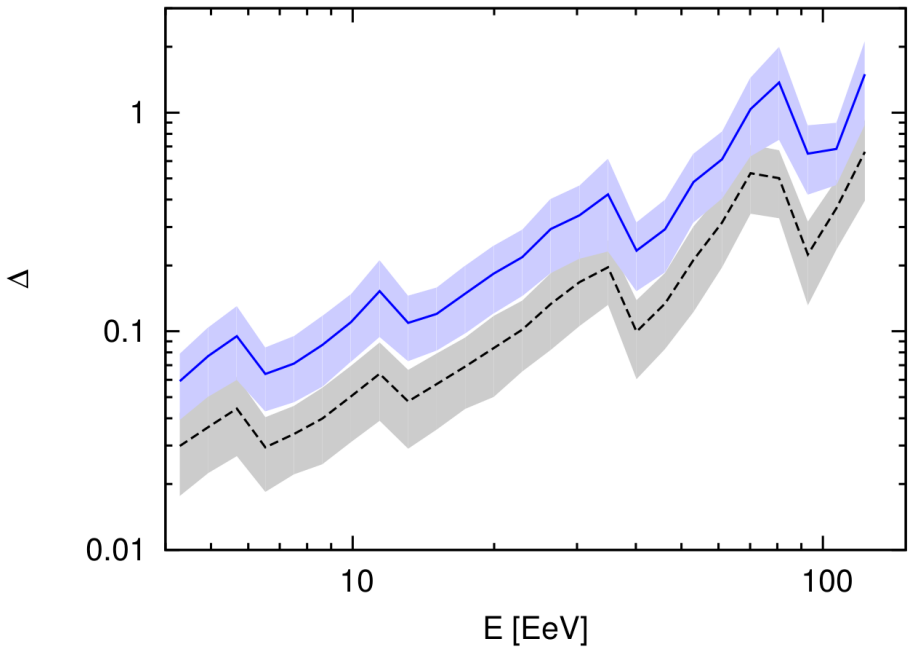

Figure 2.9: Expected dipole amplitude for a mixed composition of cosmic rays when local sources over a distance of up to 100 Mpc from the observer are homogeneously distributed (black discontinuous line) and distributed like the galaxies in the 2MRS catalog (blue continuous line), with a density $\rho = 10^{-5}$ Mpc^{-3} in a 1 nG magnetic field. Taken from [57].

2.9.4 Status of the experimental results

Several studies of anisotropies at large angular scales have been carried out using the data collected by different experiments of EAS. In most of them, the Rayleigh method [59] is applied to perform

an analysis of first harmonics in right ascension to search for any anisotropy signal in the cosmic-ray flux [59]. In the ultra-high energy region, results obtained by several experiments point to a very isotropic distribution of arrival directions over a wide range of energy. The Haverah Park experiment claimed a possible sign of anisotropy [60]: in the region of $\sim 10^{17}$ eV a dipole of amplitude $d = (1.52 \pm 0.44)\%$ was detected in the direction of right ascension $\alpha = 212^\circ \pm 17^\circ$ with a chance probability of 0.3%. However, the results obtained by the Yakutsk experiment are compatible with an isotropic flux distribution in the energy range of $\sim 10^{16.5} - 10^{17.5}$ eV [61]. The AGASA experiment also did not detect significant anisotropy in a similar energy range ($\sim 10^{17.} - 10^{17.5}$ eV), while for energies around 10^{18} eV, an excess around the galactic center and the Cygnus region [62] was reported: a dipolar anisotropy of amplitude $\simeq 4\%$ with a chance probability of 0.2% was found using a two-dimensional analysis in right ascension and declination with a total of ≈ 114000 events with energies above 10^{17} eV. However, this result could not be confirmed by the Pierre Auger Observatory when a much larger number of detected events was used to improve the statistics.

The existence of an anisotropy signal for energies around $\sim 10^{18}$ eV in a direction close to the galactic center was also reported by the SUGAR experiment [63]. However, it was observed that the signal was consistent with that of a point source, and no evidence of an excess of cosmic rays from the direction of the galactic center was detected. On the other hand, a dedicated search by the Pierre Auger Observatory for signs of anisotropy from the galactic center region has failed to confirm the excess measured by AGASA [64].

Upper limits for the equatorial dipole amplitude $d_\perp$ of the first harmonic modulation were obtained by the Pierre Auger collaboration in [65] from studies of the propagation of particles in the galactic magnetic fields. Figure 2.10 shows the results obtained in this study, as well as the main results of anisotropies obtained by various cosmic-ray experiments. The upper limits on the equatorial dipole amplitudes range from 1.3% at $10^{17.3} < E < 10^{17.7}$ eV, to 9.9% above $10^{18.9}$ eV and are calculated with a 95% confidence level. For an energy of $\approx 10^{18}$ eV, the upper limit is $d_\perp = 1.5\%$, which contradicts the excess measured by AGASA. Figure 2.10 summarizes the status of anisotropy studies at large angular scales before the most recent work done in [66].

2.9.4.1 Pierre Auger Observatory results

Several studies in a search for large scales anisotropies have been carried out by the Pierre Auger Collaboration in its almost 17 years of operation since 2004. An analysis of the first harmonics in right ascension was performed in [65] over a wide energy range with data collected by the Pierre Auger Observatory in the period from January 1^{rst}, 2004 to December 31, 2009. Various energy ranges were analyzed ($1-2, 2-4, 4-8, > 8$ EeV). Below 8 EeV, no statistically significant signal of anisotropy was found. However, in the range of energies higher than 8 EeV, an amplitude of the first harmonic $r_\alpha = 4.1\%$ was detected with chance probability (p-value) of 0.09 corresponding to a component of the dipole in the equatorial plane $d_\perp = 9.9\%$ in the direction $\alpha_d = 117^\circ \pm 27^\circ$.

In [59], more than 70 000 events with energies above 4 EeV were analyzed, detected over a

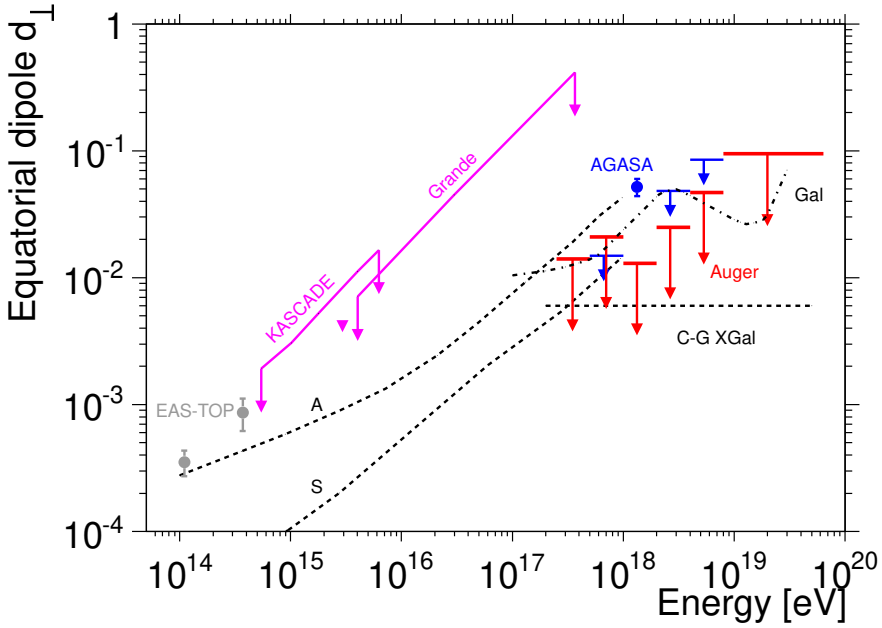

Figure 2.10: Upper limits for the amplitude of the equatorial anisotropy obtained from the first harmonic as a function of the energy obtained in [65]. Results of the EAS-TOP, AGASA, KASKADE and KASKADE-Grande experiments are also displayed. Also shown in dashed lines are predictions up to 1 EeV of two galactic magnetic field models with different symmetries (A and S), predictions for a purely galactic origin of UHECRs up to a few tens of 10^{19} eV, and the expectations of the Compton-Getting effect for an isotropic extragalactic component in the CMB resting frame. Taken from [65].

10-year period from January 1, 2004, to December 31, 2013. For the $4 - 8$ EeV energy range, no significant anisotropy signal was detected. For energies above 8 EeV, the analysis in right ascension revealed an amplitude of the first harmonic of $r_\alpha = (4.4 \pm 1.0)\%$ with a p-value of 6.4×10^{-5}. This amplitude, together with that one equivalent for the azimuth angle modulation produced a dipole amplitude of $d = (7.3 \pm 1.5)\%$ in direction $(\alpha_d,\ \delta_d) = (95^\circ \pm 13^\circ,\ -39^\circ \pm 13^\circ)$. On the other hand, the analyses carried out in [67] on this same data set, but with two different methods, revealed similar dipole amplitudes: using a power spectrum analysis method, a dipole of amplitude $d = (6.0 \pm 1.5)\%$ was detected with a p-value of 1.3×10^{-5}, while a needlets analysis [68] revealed a dipole of amplitude $(6.8 \pm 1.6)\%$ in the direction $(\alpha,\ \delta) = (97^\circ \pm 16^\circ,\ -39^\circ \pm 17^\circ)$ with a p-value of 2.5×10^{-3}.

Recently, in [66], in an extension of the analysis carried out in [59], the collection period has been extended until August 31, increasing the statistics by approximately 18%. In this case, the analysis was carried out with a total of more than 100 000 events with energies above 4 EeV. Again the results obtained in the range of 4 to 8 EeV were consistent with an isotropic distribution. Above 8 EeV, a dipole anisotropy of amplitude $d = (6.5^{+1.3}_{-0.9})\%$ was detected in the direction $\alpha_d = 100^\circ \pm 10^\circ$ and $\delta_d = -24^\circ{}^{+12^\circ}_{13^\circ}$, now with a statistical significance of more than 5.2σ, reaffirming the results obtained in [59] and confirming the existence of a strong anisotropy signal

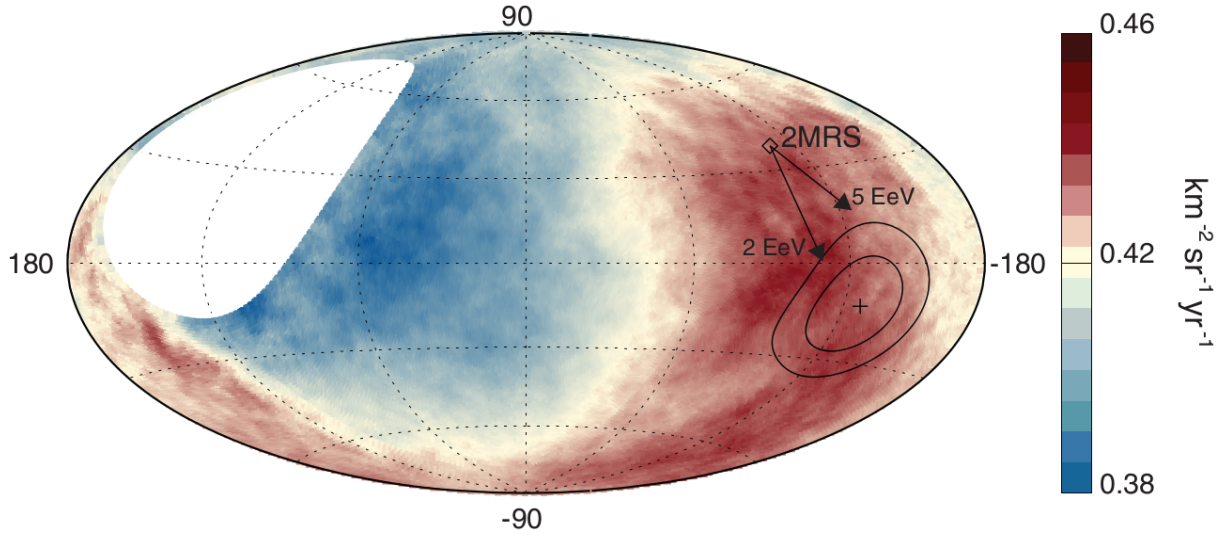

Figure 2.11: Sky map in galactic coordinates showing the cosmic-ray flux for energies above 8 EeV smoothed with a 45° top-hat function. The galactic center is at the origin. The cross indicates the measured dipole direction and the scans denote the 68% and 95% confidence level regions. The dipole in the 2MRS galaxy distribution is indicated. Arrows show the deflections expected for particles propagating from the direction of the 2MRS dipole with rigidity $E/Z = 5$ and 2 EeV under the influence of the galactic magnetic field. Taken from [66].

for events with energies above 8×10^{18} eV. Figure 2.11 shows the sky map in galactic coordinates of the cosmic-ray flux for energies above 8 EeV analyzed in [66]. The dipolar pattern can be seen in a region that is consistent with the direction expected for particles propagating from the 2MRS dipole direction under the influence of the galactic magnetic field. As shown in Figure 2.11, the direction of the dipole lies $\sim 125°$ from the Galactic center, disfavoring a Galactic origin for cosmic rays observed in the region of energies above 8 EeV. This detection thus possibly constitutes the first observational piece of evidence for an extragalactic origin of cosmic rays beyond the ankle.

In [69], a similar analysis was performed further splitting the events detected with $E \geq 4$ EeV into four energy bins. The direction of the reconstructed dipoles suggests an extragalactic origin for the CRs in each energy bin. Also, an indication at the 3.7σ CL of an increase of the dipolar amplitude with energy was found, expected due to the smaller deflections suffered by the cosmic rays at higher rigidities. The dipole amplitude is also enhanced for increasing energies owing to the increased attenuation suffered by the particles coming from distant sources, which implies an increase in the relative contribution to the flux arising from the nearby sources, leading to a more anisotropic flux distribution.

Chapter 3

Extensive air showers and the Pierre Auger Observatory

We discuss in this chapter the main physical ingredients necessary to understand the development of an extensive air shower, especially its electromagnetic and hadronic components. A brief description of the detection systems of the Pierre Auger Observatory is also included. The discussion is intended only to introduce the reader to the main features of the observatory and present important variables to be used in the data analysis of the next chapters. The reader is directed to the appropriate references for further details.

3.1 Extensive air showers

When a sufficiently energetic cosmic ray hits the top of the atmosphere, it can produce a nuclear reaction, generating secondary particles that in turn can interact again with the constituent atoms constituents of the atmosphere, thus initiating a cascade or atmospheric shower where at each step of interaction new particles are generated. The particles in this shower form a disk with a thickness of a few meters and a lateral diameter that can extend over several kilometers. The disc propagates at a speed close to that of light in the atmosphere, with a slightly curved front that can be considered flat in a first approximation (fig. 3.1).

The total number of secondary particles increases with the energy of the primary cosmic ray. For example, protons with an energy of 10^{15} and 10^{19} eV produce approximately 10^6 and 10^9 secondary particles, respectively. The total number of particles at each instant varies with the shower propagation deep into the atmosphere. When the energy of the particles in the cascade reaches the threshold of producing new secondary particles, the number of particles in the shower starts to decay exponentially with atmospheric depth due to absorption processes. The atmospheric depth X is a measure of the amount of matter traversed by the shower during its development to

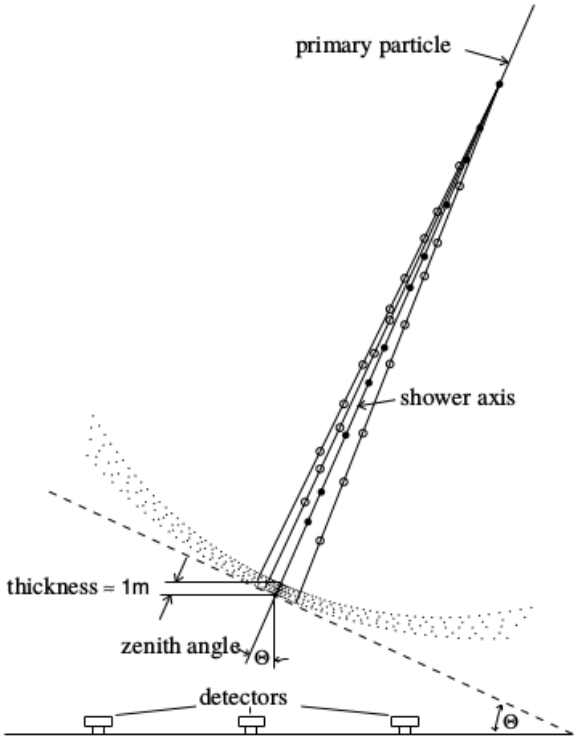

Figure 3.1: Schematic representation of the detection of an atmospheric shower by an array of surface detectors. The zenith angle θ represents the inclination of the shower axis in relation to the vertical line. The disk, with a thickness $\sim$ 1 m near the center, is represented by the small dots. The thick dots represent the different interactions that occurred around the shower axis during its development, the primary interaction typically occurs at heights of $\sim$ 10 km. Figure extracted from [54].

a certain height h_0 defined mathematically in the approximation of a flat atmosphere as

$$X = \int_{h_0}^{\infty} \rho(h) \frac{dh}{\cos(\theta)} \ , \tag{3.1}$$

called slant depth and usually expressed in units of g cm^{-2}, here θ is the angle formed by the shower axis and the vertical direction, called the shower head or zenith angle, and $\rho(h)$ is the function which describes the density variation with height. Cosmic rays with sufficiently high energies generate extensive air showers whose secondary particles are able to reach the Earth's surface. The number of particles that reach the surface depends both on the nature and energy of the primary particle and on its arrival direction. About 99% of these particles are electrons (or positrons) and photons, forming the electromagnetic component of the shower. Their energy is in a range of 1 to 10 MeV and they carry $\sim$ 85% of the total energy of the cascade. The second significant component is the muonic component, carrying $\sim$ 10% of the total energy. Finally, pions and a small portion of baryons form the hadronic component that is concentrated very close to the shower axis and takes $\sim$ 4% of the total shower energy. Neutrinos are also produced in cascade interactions, however, their contribution is negligible in relation to the components mentioned above.

3.1.1 Electromagnetic component

In the primary interaction, mainly pions and kaons are produced. The subsequent decay of neutral pions into photons generates the electromagnetic component: photons create electron-positron pairs via pair production, which swiftly emit new photons through bremsstrahlung radiation creating a cascade process. Secondary processes such as Compton scattering by photons and energy losses in electrons by ionization processes can be neglected at high energies. Based on these aspects, Walter Heitler [70] proposed a simple model to describe the evolution of the electromagnetic component of the shower as a binary branching process, where at each step all particles interact and produce two new secondary particles, each with half the energy of the previous particle, that is, in each interaction, a photon creates a pair e^+e^- with equal energies, and each electron (or positron), emits a photon via bremsstrahlung with half its energy (see fig. 3.2).

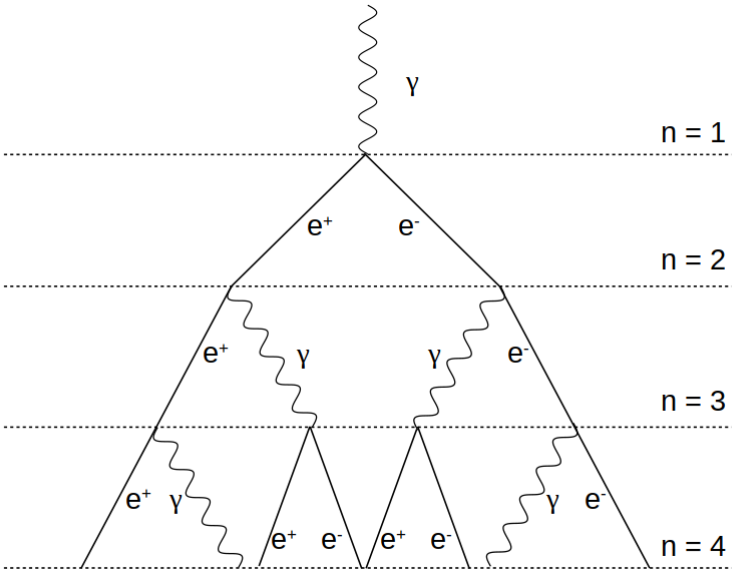

Figure 3.2: Schematic representation of the Heitler cascade model for the evolution of the electromagnetic component of the shower. At each step of interaction, the number of particles is doubled, either by pair creation or photon emission via bremsstrahlung.

Each ramification occurs, on average, after traveling a distance $d = \lambda_r \ln 2$, determined by the radiation length λ_r ($\lambda_r = 37$ g cm^{-2} in air), defined as the average distance at which an electromagnetic interaction occurs. Thus, after the shower has traveled a distance X, we have $n = X/d$ ramifications. The total number of particles then is $N(X) = 2^{X/d}$, and the individual energy of each particle is $E(X) = E_0/N(X)$, where E_0 is the energy of the primary particle. This development continues until the individual energy of the particles involved drops below a certain critical value where the rate of creation of new particles equals the rate of energy loss by ionization of the medium. This critical energy in air is $E_c^\gamma \approx 80$ MeV. At this point, the cascade reaches its maximum development characterized by the atmospheric depth $X_{\max}$. The number of particles at this stage $N_{max}(X_{\max})$ is given by the ratio between the energy of the primary particle

E_0 and the critical energy E_c. Passed this point in the shower development, the particles start to continuously lose energy, and are gradually absorbed by the medium. This simplified model is able to reproduce correctly the three main properties of electromagnetic cascades:

1. the number of particles at the point of maximum development of the cascade is proportional to the energy of the primary cosmic ray

$$N_{max}(X_{\max}) = E_0/E_c^{\gamma} \ , \tag{3.2}$$

2. the evolution of the shower maximum depth $X_{\max}$ is logarithmic with energy

$$X_{\max} = X_0 + \lambda_r \ln(E_0/E_c^{\gamma}) \ , \tag{3.3}$$

   where X_0 is the depth of the first interaction,

3. the elongation rate D_{10}, defined as the rate of evolution of $X_{\max}$ with energy, is determined by the radiation length

$$D_{10} = \frac{dX_{\max}}{d(\log_{10} E_0)} = 2.3 \ \lambda_r \ , \tag{3.4}$$

   In air this value is about 85 g cm^{-2}.

These predictions have been confirmed by Monte Carlo simulations of the development of extensive atmospheric showers, although the number of particles at the maximum shower development is overestimated by a factor of 2∼3. This can be explained by the fact that very often multiple photons are created during bremsstrahlung emission, and that electrons lose their energy much faster than photons.

3.1.2 Hadronic component

Heitler's model can be adapted to describe the development of the hadronic component of the shower [71, 7], composed mainly by n, p, π^0, $\pi^{\pm}$, K^0, and $K^{\pm}$. In this case, the relevant parameter to be considered is the hadronic interaction length λ_I. At each interaction step of atmospheric depth $\lambda_I \ln 2$, the creation of $2N_\pi$ charged pions and N_π neutral pions with equal energy is assumed [1]. The π^0's decaying into photons immediately becomes part of the electromagnetic component of the shower, while the $\pi^{\pm}$ continue participating in the cascade interaction processes until they reach the critical energy $E_c^{\pi} \approx 20$ GeV in air, with which its decay into muons ($\pi^{\pm} \rightarrow \mu^{\pm} + \nu_\mu$) is more likely than a new hadronic interaction. At each interaction step, the electromagnetic component is fed with 1/3 of the hadronic component energy. Therefore, showers, where a larger number of steps for the pions to reach the critical energy E_c^{π}, have a stronger electromagnetic component. Furthermore, due to the fact that the density of the atmosphere gradually decreases with height, the probability of a hadronic interaction also decreases, therefore E_c^{π} increases with

[1] $N_\pi = 5$ for pions with energies between 1 GeV and 10 TeV [7].

height, and showers initiated at greater atmospheric depth X_0, will have a lower critical energy and consequently a lower number of muons produced. This means that the total energy carried by the muons that reach the ground level decreases with the atmospheric depth of the first interaction.

To obtain an estimate of the total number of muons in the shower, we assume that all pions decay into muons when they reach critical energy. So the number of muons N_μ can be calculated by

$$N_\mu = \left(\frac{E_0}{E_\mu^\pi}\right)^\beta , \tag{3.5}$$

where $\beta = \ln 2N_\pi / \ln 3N_\pi$ [2]. Unlike the electromagnetic component, the number of muons does not increase linearly with the energy of the primary particle, but at a lower rate. The precise value of β depends on the average multiplicity value used for the pions, as well as the inelasticity of hadronic interactions. Assuming that only half of the energy is carried by the pions at each interaction step, we obtain a value of $\beta = 0.93$, whereas detailed simulations give values of β between 0.93 and 0.95. However, this simplified model cannot be used to correctly predict the total number of muons at the ground, in particular for large distances from the shower axis. For this, the knowledge of the distribution of muon production with height, the distribution of moments, and in particular, their transversal component, plays a fundamental role.

Determining the depth of the shower maximum development for the hadronic component is more complicated than in the case of the electromagnetic component. As the cross-section and multiplicity N_π increase, the value of $X_{\max}$ decreases, while the evolution of these magnitudes with energy modifies the elongation rate D_{10}. On the other hand, the inelasticity of hadronic interactions also modifies both the depth $X_{\max}$ and the rate of elongation. The proper determination of these magnitudes needs to be done by making use of detailed shower simulations.

However, an approximate theoretical extension of the previous Heitler's model can be made using the superposition principle for the case where the primary particle is an atomic nucleus. In this sense, the interaction of a nucleus of atomic mass A can be seen as the superposition of the individual interactions of A nucleons with energy E_0/A. As a result, showers initiated by heavier nuclei will reach their maximum development faster and higher in the atmosphere, and with smaller shower-to-shower fluctuations than those initiated by lighter nuclei. From this, we can extract the following conclusions:

1. Showers initiated by nuclei with mass number A will reach their maximum development higher in the atmosphere, being the relative displacement to proton showers

$$X_{\max}^p - X_{\max}^A = \lambda_r \ln A. \tag{3.6}$$

2. Showers initiated by nuclei with mass number A will have a higher number of muons given by

$$N_\mu^A = N_\mu^p A^{1-\beta}. \tag{3.7}$$

[2] $\beta = 0.85$ for $N_\pi = 5$ [7].

3. The evolution with primary cross-section, energy, and multiplicity for nuclei is the same as for protons, so different nucleons will have identical elongation rates.

4. $X_{\max}$ shower-to-shower fluctuations will be smaller for heavier showers.

All hadronic interaction models share these basic principles, and the results shown above have been largely confirmed by detailed shower simulations [72, 73, 74, 75].

When the particles of the muonic component reach the critical energy, the charged pions and kaons $\pi^{\pm}$ e $K^{\pm}$ decay into muons $\mu^{\pm}$ which represent $\sim 80\%$ of the total number of charged particles that reach the surface, taking $\sim 10\%$ of the total energy. Muons are able to reach the ground because of their great ability to pass through matter, dominating the signal in the surface detectors at large distances from the shower axis. Neutrinos are mainly produced by the decay of both pions and muons, having a minor role in the detection of secondary particles since their cross-section of interaction is very small.

3.1.3 Chemical composition

The identification with good accuracy of the primary cosmic ray chemical composition, on an event-by-event basis, is a challenging task mainly due to the shower-to-shower fluctuations in their development. Therefore, the identification of the chemical composition of the incident particles can only be done in specific energy ranges by analyzing a statistically significant set of showers. For the highest energies, the best-established technique to extract information on the chemical composition of the primary cosmic ray is the measurement of the position of the maximum development of the shower $X_{\max}$ [76]. The main models predict the following relationship between the average value of $X_{\max}$, the energy E of the primary particle and its mass number A

$$X_{\max} = (1-b)\lambda_r \left(\ln \frac{E}{E_c} - \langle \ln A \rangle \right) , \tag{3.8}$$

where the parameter b is zero for a purely electromagnetic cascade, and for a mixed shower, it is less than unity by an amount that depends on the hadronic model of interaction used. The fluctuations of $X_{\max}$ become smaller as the mass of the primary particle increases, regardless of the hadronic model in question. Thus, both $X_{\max}$ and its standard deviation $\sigma_{X_{\max}}$ are useful observables for chemical composition studies. To extract any quantitative information from the $X_{\max}$ distributions it is necessary to compare these distributions with the results obtained through showers simulations which depend mainly on the hadronic interaction model used in the computations.

3.2 The Pierre Auger Observatory

The Pierre Auger Observatory is located in Malargüe, Argentina, at $-35.2°$ of latitude and $69.5°$ of longitude. It consists of a very large array of detectors specially designed for the study of

EASs produced by the interaction of cosmic rays with atoms at the top layers of the atmosphere. The prime goal of this observatory is to investigate the main features of the UHECRs, regarding sources, origination, acceleration, and propagation by means of the analysis of the energy spectrum, arrival direction distribution, and chemical composition of the detected particles. In addition to its large extension, a distinctive characteristic of the Pierre Auger Observatory is the use of a hybrid detection technique based on the combined use of Cherenkov surface detectors operating in conjunction with fluorescence telescopes. The Surface Detector (SD) is composed of an array of 1600 water-Cherenkov detectors distributed over an area of 3000 km^2 with a spacing of 1500 m between them, and it is aimed to detect the secondary shower particles that hit the Earth's surface. On the other hand, the Fluorescence detector (FD) consists of an ensemble of 27 fluorescence telescopes located in four optical stations positioned at the periphery of the SD array and it is designed to measure the fluorescence light emitted during the shower development. The SD has a duty cycle of nearly 100% while the FD only operates on moonless nights, with low cloud cover and favorable weather conditions, so its operational observation time is about 13% of the SD. These two complementary detection methods, together with the large detection area, allow the Pierre Auger Observatory to acquire data with great statistics and quality, making it the most important observatory today specialized for the study of cosmic rays with the highest energies.

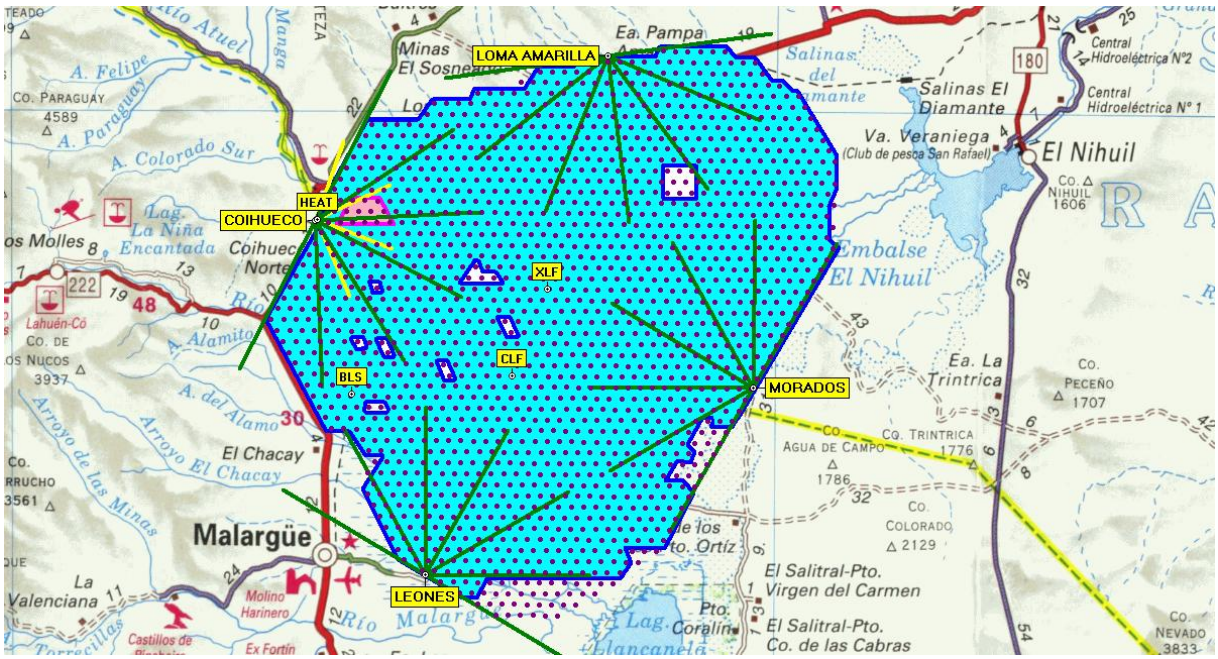

Figure 3.3: Aerial view of the Pierre Auger Observatory. The black dots represent the water Cherenkov detectors of the SD. The green solid lines represent the field o view in azimuth of each of the fluorescence detectors.

3.2.1 The surface detector

The SD measures the lateral distribution at the ground level of the particles generated in the shower in the atmosphere. It consists of an array of 1600 water Cherenkov detectors aligned in a triangular equilateral grid with a spacing of 1500 m between adjacent detectors. Each detector is basically a cylindrical tank of 10 m^2 of base area and 1.2 m of height containing a total of 12000 liters of ultra-pure water. At the top of each tank, there are three photomultiplier tubes (PMTs) symmetrically distributed at a distance of 1.2 m from the central axis, looking down into the water through transparent polyethylene windows. These photomultipliers capture the Cherenkov light produced by the passage of charged relativistic particles through water and are also sensitive to high-energy photons capable of creating electron-positron pairs in the volume of water. Each surface detector station is self-sufficient in the sense that it is powered by its own system of solar panels and batteries, which provide an average of 10 Watts to the PMTs and the detector's electronic package, consisting of a processor, a GPS receiver, a radio transceiver, and a power controller. Thus, electrons, photons, and muons from the EAS are monitored at the surface approximately 100% of the time. Figure 3.4 shows the components of an SD station. A detailed description can be found in [77].

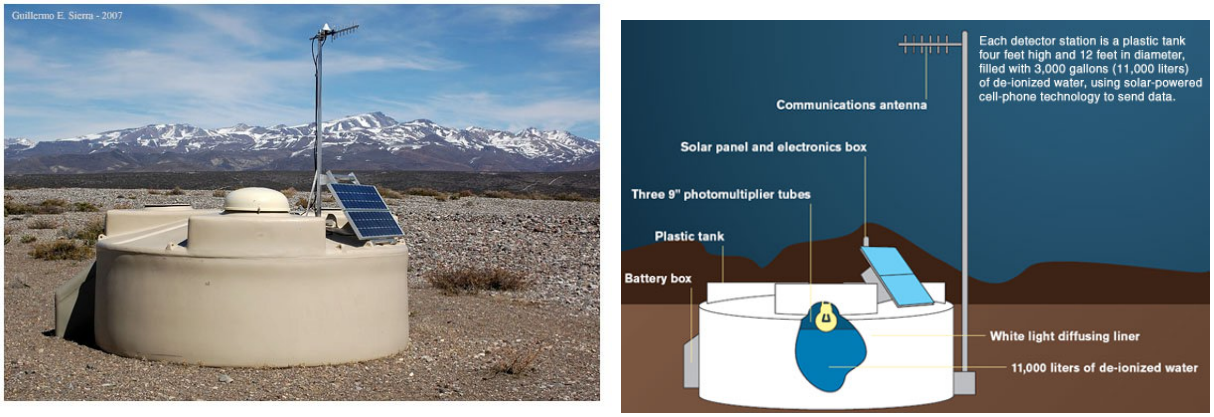

Figure 3.4: Lateral view of the Pierre Auger Observatory surface detector station with a brief description of its main components.

3.2.2 The fluorescence detector

The fluorescence detector consists of four optical stations located atop small elevations on the periphery of the SD array (see fig. 3.3). Each station has a total of six fluorescence telescopes looking onto the array with a small elevation of $\simeq 1.5°$. The field of view of each telescope is $30° \times 30°$ with which each station covers an angular window of $180°$ in azimuth by $30°$ in elevation. Figure 3.5 shows a schematic view of the arrangement of detectors in a station.

The purpose of the FD is to collect the fluorescence light emitted by the atmosphere during the passage of the shower. The operation of the telescopes is based on Schmidt optics. Each one

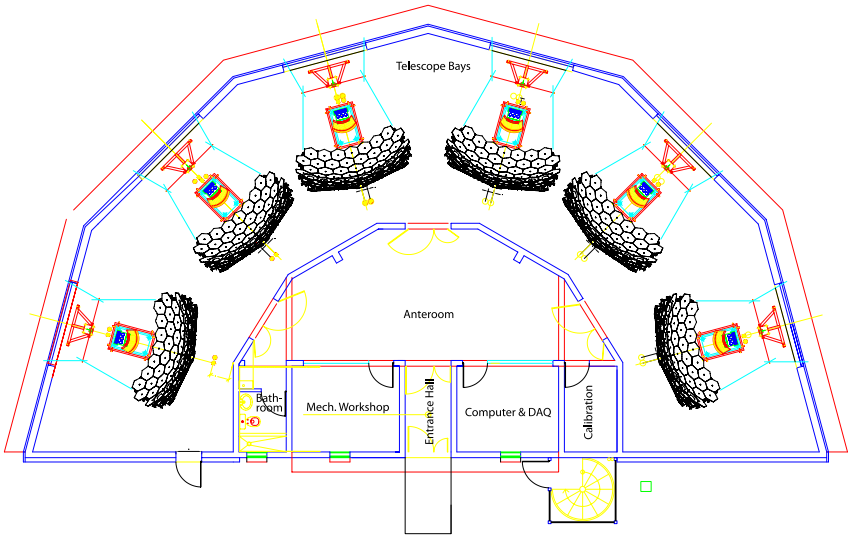

Figure 3.5: Schematic drawing of the fluorescence telescopes arrangement in an FD station. Figure extracted from [78].

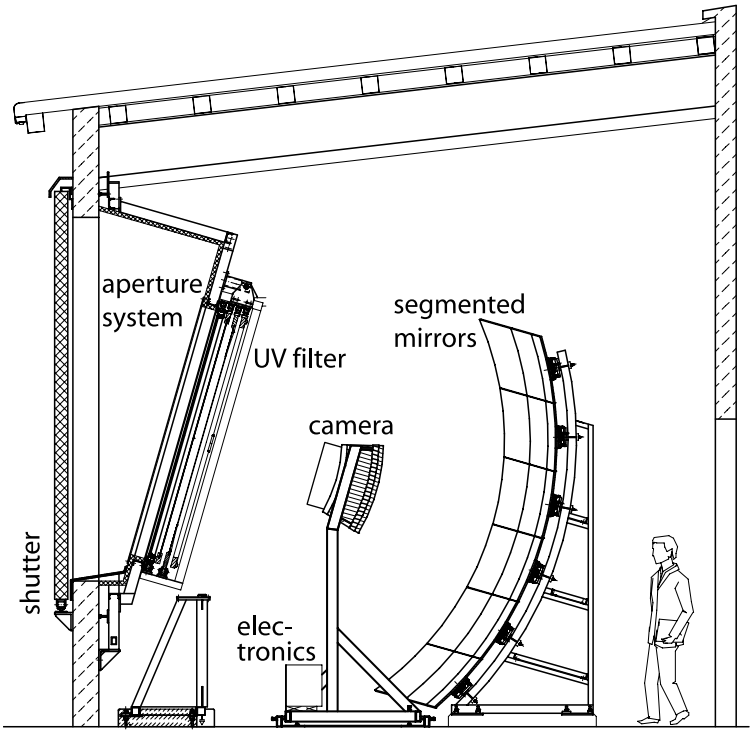

Figure 3.6: Schematic view of an SD fluorescence telescope. Figure extracted from [78].

consists of a segmented spherical mirror of ~ 10 m^2, a spherical focal plane, an ultraviolet light band-pass filter of $300 - 410$ nm, and a refractive corrector ring at the opening. The fluorescence light passes through the ultraviolet filter and the corrector lens and is focused by the mirror onto a 440-pixel photomultiplier tube camera. The light pulses are digitized every 100 ns and a multi-level hierarchy of triggers culminates in the detection and recording of cosmic-ray showers. There are several levels of triggers. The first digitizes the signals from the analog boards of each pixel above 10 MHz. The second trigger looks for track segments of five active pixels, and for this goal,

every 100 ns the entire camera is scanned in search of track patterns in the triggered pixels. The third trigger level in FD is a software algorithm that rejects events caused by lightning, muons impacting the focal plane, or randomly triggered pixels. In addition, each detector is properly calibrated to find the correct conversion between digital counts and actual light measured in number of photons. Figure 3.6 shows the main components of a fluorescence camera. Further details can be found in [77].

Chapter 4

Arrival direction distributions of UHECRs

In this chapter, we explore astrophysical scenarios of UHECRs consistent with the results of previous studies of large-scale anisotropies performed with the data collected by the Pierre Auger Observatory. Section 2.9.4.1 summarizes some of the most important results of studies regarding large scale anisotropies carried out by the Pierre Auger Collaboration. Here we will focus our attention on the results published in [66], where a dipolar anisotropy of amplitude $\Delta = 0.065$ was found in the cosmic-ray flux for energies above 8 EeV. Here we will analyze the behavior of dipolar anisotropy patterns as a function of the energy as well as the influence of both galactic and extragalactic magnetic fields in the arrival direction distribution detected at Earth. The cosmic-ray propagation under the influence of energy-loss processes and magnetic deflection was simulated with the CRPropa code [79].

4.1 Anisotropies of UHECRs of extragalactic origin

In general, a dipolar component of anisotropy can be calculated as follows. The distribution of arrival directions $\hat{u}$ of particles from a single source at distance $r_s \equiv r_s \hat{r}_s$ depends only on the angle between $\hat{u}$ e $\hat{r}_s$, $\theta = \arccos(\hat{u} \cdot \hat{r}_s)$ and can be expanded into Legendre polynomials as

$$\Phi(\hat{u}) = f(\cos\theta) = \Phi_0 + \Phi_1 \hat{u} \cdot \hat{r}_s + \dots \ , \tag{4.1}$$

where the expansion coefficients can be calculated directly as

$$\Phi_0 = \frac{1}{4\pi} \int \Phi(\hat{u}) d\Omega = \frac{1}{2} \int_{-1}^{1} f(\cos\theta) d\cos\theta \ , \tag{4.2}$$

$$\Phi_1 = \frac{1}{4\pi} \int \Phi(\hat{u}) \hat{u} \cdot \hat{r}_s d\Omega = \frac{3}{2} \int_{-1}^{1} f(\cos\theta) \cos\theta d\cos\theta \ , \tag{4.3}$$

with which the dipolar amplitude is given by

$$\Delta = \frac{\Phi_1}{\Phi_0} = 3\langle \cos\theta \rangle \tag{4.4}$$

pointing in the source direction. In the case of perfectly rectilinear propagation, we have $\langle \cos\theta \rangle = 1$ and $\Delta = 3$. At this stage, the simulations were made considering the propagation of protons in extragalactic space, assuming for simplicity that an isotropic and uniform turbulent magnetic field is present in the diffusion region. In the case of isotropic diffusion, which is characterized by a diagonal diffusion tensor, the flux of particles is given by $\mathbf{J} = -D\,\nabla n$, with n being the particle number density and D the diffusion coefficient. The diffusion length $l_D \equiv 3D$ characterizes the distance after which the particle deflection is $\simeq 1$ rad. As long as the distance from the source is much greater than l_D, the spatial diffusion of particles occurs. For sufficiently large energies, l_D becomes greater than r_s, and we enter the quasi-rectilinear regime where the total deflection of particles arriving from the source is less than 1 rad, and, therefore, only some angular diffusion will occur, but the spatial diffusion will not take place. The beginning of the quasi-rectilinear regime corresponds to the condition $r_s = l_D$, which means $E > E_{rect} \equiv E_c\sqrt{r_s/l_c}$, where $E_{rect} > E_c$ was assumed so $D \propto E^2$ which is indeed the case when $r_s \gg l_c$[56]. In these simulations, the evolution of the anisotropy signal with energy will be studied for various different scenarios.

4.1.1 Anisotropies from a single source

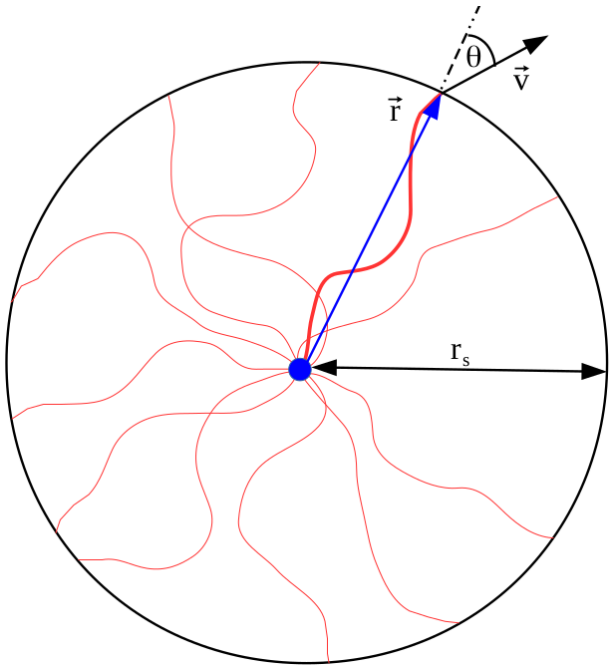

Figure 4.1: Geometric construction used to calculate the dipolar amplitude of the cosmic-ray flux coming from a source located at a distance r_s. The distribution of arrival directions depends only on the angle θ between the direction of the source and the speed of the particle at the moment of detection. The dipolar amplitude is calculated as $\Delta = 3\langle \cos\theta \rangle$.

In order to calculate the amplitude of the expected dipolar anisotropy of a particle flux from a source at a distance r_s, we follow the trajectory of a large number of protons emitted isotropically at the source and calculate the mean value of the cosine of the angle between the velocity of the particle and its position every time it passes through a spherical layer of radius r_s centered on the position of the source. Figure 4.1 schematizes the geometry used.

In all cases, the proton emission spectrum at source was taken as a power law $dN/dE_0 \propto E_0^{\gamma}$, in an energy range of $10^{17} - 10^{21}$ eV with a spectral index $\gamma = -2$. The dipolar amplitude was calculated in bins of $\log(E/\mathrm{EeV}) = 0.1$.

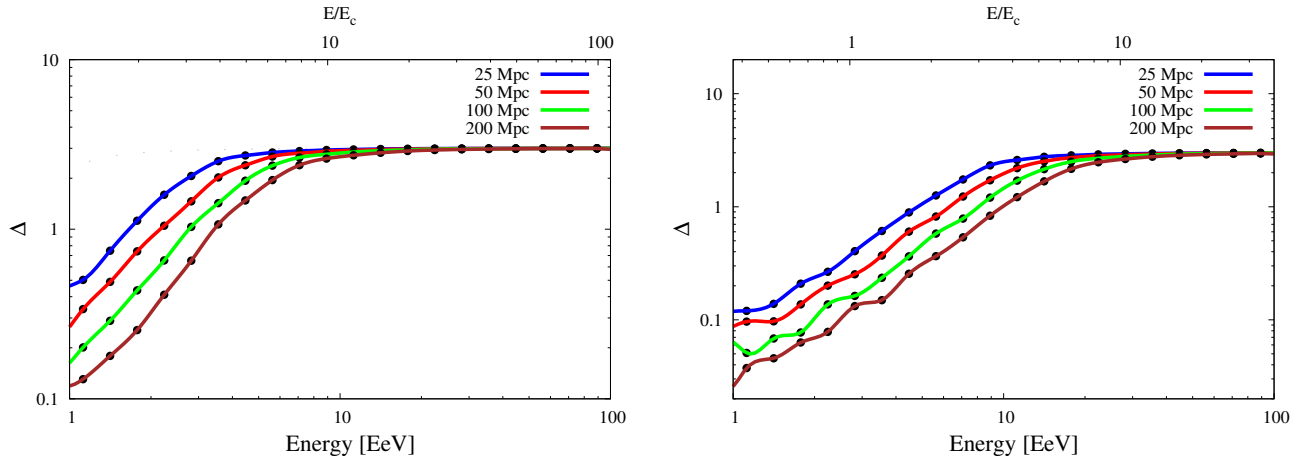

(a) $B_{\mathrm{rms}} = 1.0$ nG (b) $B_{\mathrm{rms}} = 3.0$ nG

Figure 4.2: Expected dipolar amplitude of an extragalactic proton flux coming from a source located at distances of 25, 50, 100, and 200 Mpc, for a magnetic field of amplitude $B_{\mathrm{rms}} = 1$ nG and 3 nG, and coherence length $l_c = 1$ Mpc.

Figure 4.2 shows the resulting dipole amplitude from a single source at distances of 50, 100, 200, and 400 Mpc. In the left panel, $B_{\mathrm{rms}} = 1$ nG was considered, leading to $E_c = 0.9$ EeV, while in the right panel, we consider $B_{\mathrm{rms}} = 3$ nG, corresponding to $E_c = 2.7$ EeV. Both results are similar when the energy is scaled by a factor ~ 3, that is, corresponding to the same values E/E_c, although this scale factor is not exactly 3 due to the energy losses. For very high energies, the amplitude reaches its maximum limit $\Delta = 3$, corresponding to the rectilinear propagation regime. For intermediate energies, with an increase in the distance between the source and the observer, the dipolar amplitude decreases due to a greater diffusion of the flux. The simulations were performed with 10^6 cosmic rays generated at each source, which is a number high enough to obtain a smooth curve in most parts of the energy region considered. However, small fluctuations are observed at the lower energies because the number of events detected for these bins is relatively low.

4.1.2 Anisotropies from multiple sources

In a more realistic scenario, the total cosmic-ray flux is probably composed of a set of different sources. The total dipolar component of the flux will then depend mainly on the location and luminosity of the nearest sources and on whether or not there is a large-scale anisotropy pattern intrinsic to the source distributions. If there are several sources contributing to the total flux, the amplitude of the dipolar anisotropy can be obtained by superimposing the dipoles of individual sources as

$$\mathbf{\Delta}(E) = \sum_{i=1}^{N} \frac{n_i(E)}{n_t(E)} \mathbf{\Delta}_i(E) \ , \tag{4.5}$$

where N is the number of sources that contribute to the flux at energy E, n_i is the cosmic-ray density from the i-th source, and n_t is the total density. Thus, n_i/n_t represents the fraction of the flux coming from the i-th source, and $\mathbf{\Delta}_i$ is the corresponding dipolar amplitude calculated using the method described in section 4.1. In these simulations, it was assumed, for simplicity, that the sources are stable and have equal intrinsic luminosity, that is, an equal number of initial particles was generated in all sources for propagation. We have also not included any kind of evolution of luminosity with the redshift. The source spatial distribution was considered homogeneous in comoving distance. In this way, N sources were distributed in random directions, and the distance from the i-th source to the observation point is calculated as the expected average value in a homogeneous distribution with a comoving density ρ which is given by [56]

$$\langle r_i \rangle = \left(\frac{3}{4\pi\rho} \right)^{1/3} \frac{\Gamma(i+1/3)}{(i-1)!} \ . \tag{4.6}$$

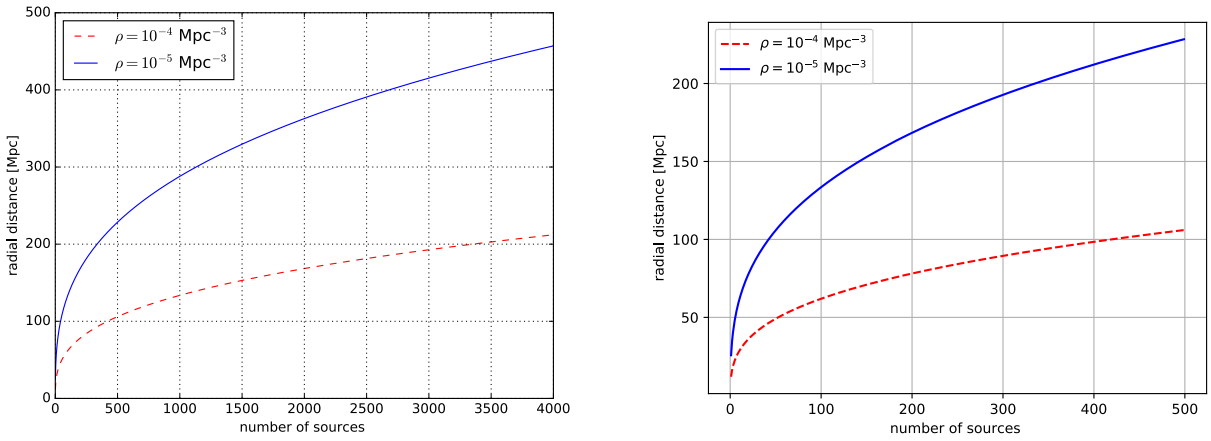

Figure 4.3: Average radial distance between the source and the observer as a function of the number of sources for a homogeneous distribution with comoving densities $\rho = 10^{-4}$ Mpc $^{-3}$ and $\rho = 10^{-5}$ Mpc $^{-3}$, respectively.

Even though a homogeneous spatial distribution of sources at large scales is considered, the appearance of anisotropy signals is expected from equation 4.5, for the reason that we have different

contributions to the total flux coming from each individual source, implying that the anisotropies generated by the nearest sources will have a greater weight on the total anisotropy. Therefore, from the reference system centered at the point of detection, the local source distribution will have a dominant impact on the overall anisotropy pattern.

In the simulations, we used source comoving density values of $\rho = 10^{-5}$ and 10^{-4} Mpc^{-3}, which are consistent with predictions on the lower bound value of $\rho_- = 6 \times 10^{-6}$ found in [80] for large angular scales. Figure 4.3 shows the behavior of equation 4.6 for the two source densities used in these simulations. For $\rho = 10^{-5}$ Mpc^{-3}, the nearest source is at a distance $\langle r_1 \rangle \simeq 25$ Mpc, while for $\rho = 10^{-4}$ Mpc^{-3}, $\langle r_1 \rangle \simeq 11$ Mpc. It can be seen that the number of sources increases rapidly with the distance, going from $\gtrsim 300$ sources for 200 Mpc to $\gtrsim 2500$ for 400 Mpc in the case of a source density of $\rho = 10^{-5}$ Mpc^{-3}. Therefore, for reasons of computational cost, at the time of producing these results, the simulations were performed with the sources being distributed up to a maximum distance of ~ 250 Mpc, which is of the order of the GZK horizon for particles with energies above $\sim 10^{19.4}$ eV, corresponding to a number of ≈ 500 sources for $\rho = 10^{-5}$ Mpc^{-3}. The extragalactic magnetic field was taken as statistically uniform and turbulent with a strength characterized by a root-mean-square value of the intensity $B_{\rm rms} = \sqrt{\langle \mathbf{B}^2(\mathbf{x}) \rangle}$. Another important property of the turbulent magnetic field is the distribution of the magnetic energy density ϵ on different length scales, which is often described by a power law in Fourier space:

$$\epsilon(k) \propto k^{-m} \, . \tag{4.7}$$

In the simulations, we adopted a Kolmogorov model. Therefore, $m = -5/3$ and the energy spectrum of turbulence $E(k)$ is related to the energy density $\epsilon(k)$ by

$$E(k) = C \, \epsilon^{2/3} \, k^{-5/3} \, . \tag{4.8}$$

A distinctive characteristic of the field is its coherence length l_c which can be defined as [56]

$$l_c = \frac{L_{max}}{2} \frac{m-1}{m} \frac{1 - (L_{min}/L_{max})^m}{1 - (L_{min}/L_{max})^{m-1}} \, , \tag{4.9}$$

where L_{max} and L_{min} are the minimum and maximum scales of the turbulence spectrum. Here we used a value of $l_c = 1$ Mpc. Another important quantity that characterizes particle diffusion is the critical energy E_c, defined in such a way that $r_L(E_c) = l_c$, and given by

$$E_c = ZeBl_c \simeq 0.9 \, Z \frac{B}{\rm nG} \frac{l_c}{\rm Mpc} \, {\rm EeV} \, . \tag{4.10}$$

This typical value separates the low-energy resonant diffusion regime, in which the particles have large deflections, from the non-resonant high-energy one, in which the deflections after crossing a distance $\sim l_c$ are relatively small.

At this point, we simulated only protons propagating from extragalactic sources. In general, the diffusion of particles decreases with the increase of the electric charge, therefore, stronger

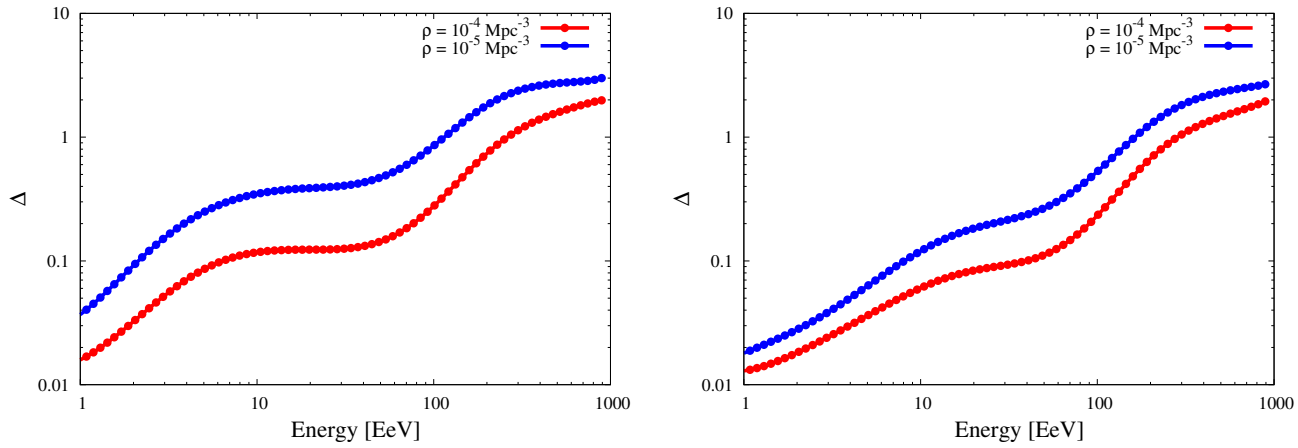

(a) $B_{\rm rms} = 1.0$ nG (b) $B_{\rm rms} = 3.0$ nG

Figure 4.4: Expected dipolar amplitude when protons are injected in the extragalactic space with a homogeneous source distribution of comoving densities $\rho = 10^{-4}$ and 10^{-5} Mpc $^{-3}$, and a magnetic field of $B_{\rm rms} = 1$ and 3 nG, respectively.

anisotropy signals are expected for heavier nuclei, and the results obtained in this chapter can be related to lower limits of dipolar anisotropy amplitude.

Figure 4.4 shows the expected dipole amplitude Δ when multiple proton sources are distributed in extragalactic space with comoving densities of $\rho = 10^{-4}$ and 10^{-5} Mpc $^{-3}$ and a $B_{\rm rms} = 1$ and 3 nG magnetic field, respectively. In both cases, a similar behavior is appreciated, and the dipole amplitude increases continuously with energy, starting from $\sim 1\%$ for the lowest energies. For higher energies, with the shrinkage of the GZK horizon, a marked increase in anisotropy is observed because the number of sources contributing to the total flux decreases as the sources will be preferentially inside the GZK sphere, so the dominating source distribution will be nearby, leading to a greater anisotropy. The higher intensity of the magnetic field results in slightly lower amplitude values, especially for low energies where the diffusion of particles increases considerably when a higher intensity field is present.

Nevertheless, we know that in the case of an isotropic source distribution, as the number of sources increases, the dipolar amplitude consequently decreases as more and more sources homogeneously distributed will contribute to the total flux, with which it is necessary to determine from what distance the resulting dipolar amplitude is no longer considerably affected by the incorporation of more sources. Figure 4.5 shows a study of this type, where we have the resulting dipolar amplitude as a function of the distance to the most distant source for various energy bins and a magnetic field of $B_{\rm rms} = 1$ nG.

It can be observed that as we increase the energy, a larger anisotropy is expected and more sources are needed for the dipole amplitude to remain constant. In this graph, a maximum distance of 900 Mpc was considered and we can see an almost asymptotic behavior of the dipole amplitude above ~ 600 Mpc in all cases. Therefore, from now on, simulations shall be performed with sources distributed up to this maximum distance.

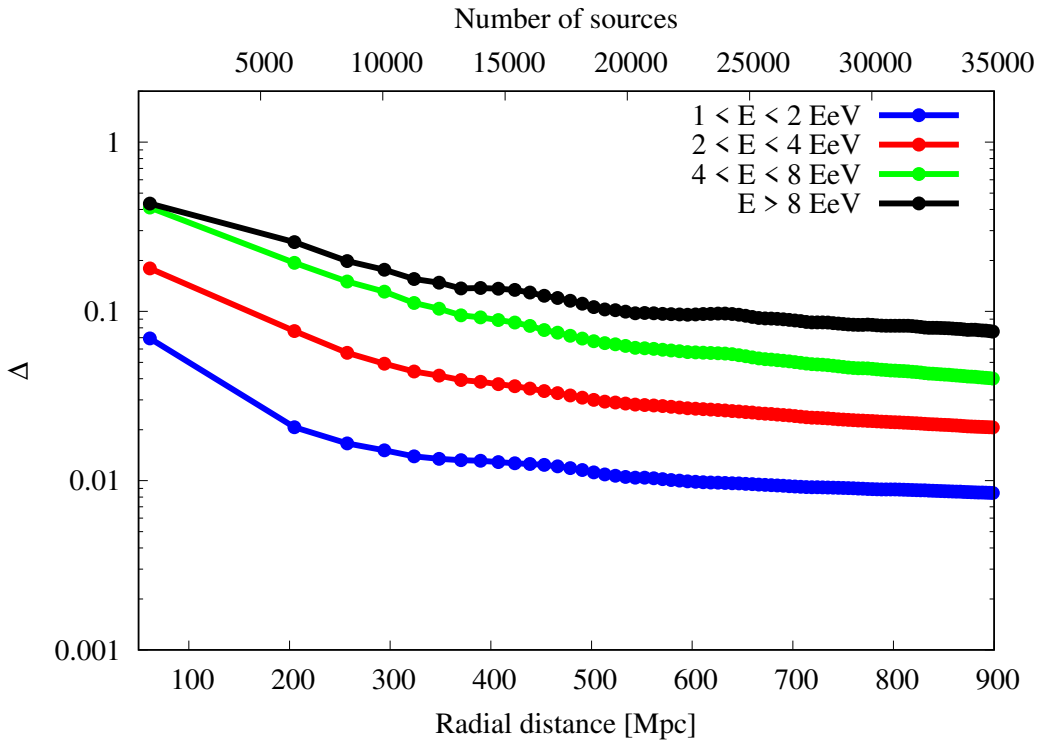

Figure 4.5: Dipolar amplitude as a function of the distance between the most distant source and the observer when protons are injected in the extragalactic space with a homogeneous source distribution of comoving density $\rho = 10^{-5}$ Mpc^{-3}, for different energy bins in a magnetic field of $B_{\rm rms} = 1$ nG.

Figure 4.6 shows the arrival direction distribution for protons propagating from five different extragalactic sources. It can be appreciated that with the increase in energy, the propagation starts to be more and more rectilinear and the arrival direction of the cosmic rays points to the direction of the source. Therefore, in the limit of very high energies, one expects that the direction of the resulting dipole will be completely determined by the source distribution in the extragalactic space.

4.2 Galactic propagation of UHECRs

In order to explore the influence of the galactic magnetic fields in both the amplitude and direction of a cosmic-ray flux with dipolar anisotropy, we follow the inverted trajectories of many particles propagated from Earth up to the border of the galaxy (backtracking). In these simulations, the region of the galaxy was considered as a sphere with radius $R_g = 20$ kpc. Then we propagate anti-protons with energies above 8 EeV from the Earth, located at 8.5 kpc from the galactic center, through galactic space under the influence of the JF12 galactic magnetic field (GMF) model [39, 40]. The Striated and Random components of the GMF are turned off, and the strength of the field is characterized by the value of $B_{\rm rms} = 10^{-4}$ G. The starting distribution of the cosmic-ray directions is dipolar with amplitude $d = 0.1$ and with the initial dipole oriented in

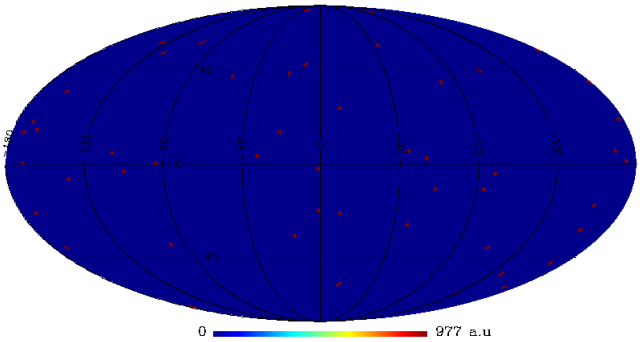

(a) $E/E_c = 0.1$

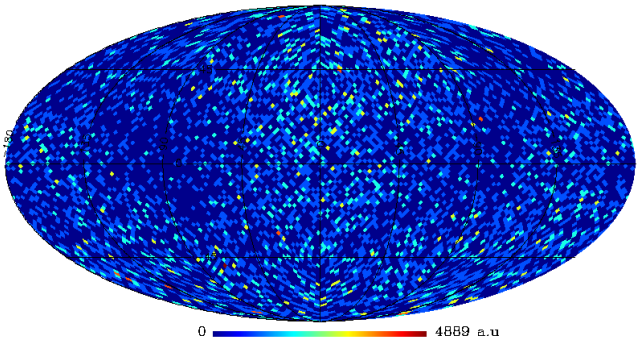

(b) $E/E_c = 1.0$

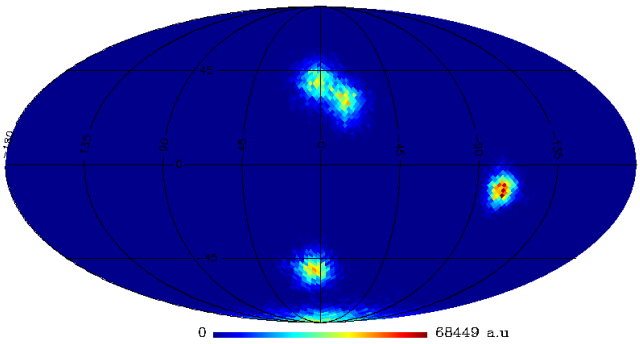

(c) $E/E_c = 10$

Figure 4.6: Sky maps in equatorial coordinates of the arrival directions distribution of protons propagating from five different sources, for various values of E/E_c and a magnetic field of $B = 1$ nG.

different directions. At the end of the simulation, we obtain a sky map with the distribution of the backtracked cosmic-ray directions at the border of the galaxy. Our intention is to explore the effect of the GMF in both dipole amplitude and orientation of the starting distribution.

Figures 4.7 and 4.8 show the mollview projections of the sky maps with both the starting dipolar distribution of particles backtracked and the final one recorded at the border of the galaxy. As can be seen in table 4.1, both the amplitude and direction of the initial distribution suffer important variations under the influence of the galactic magnetic field.

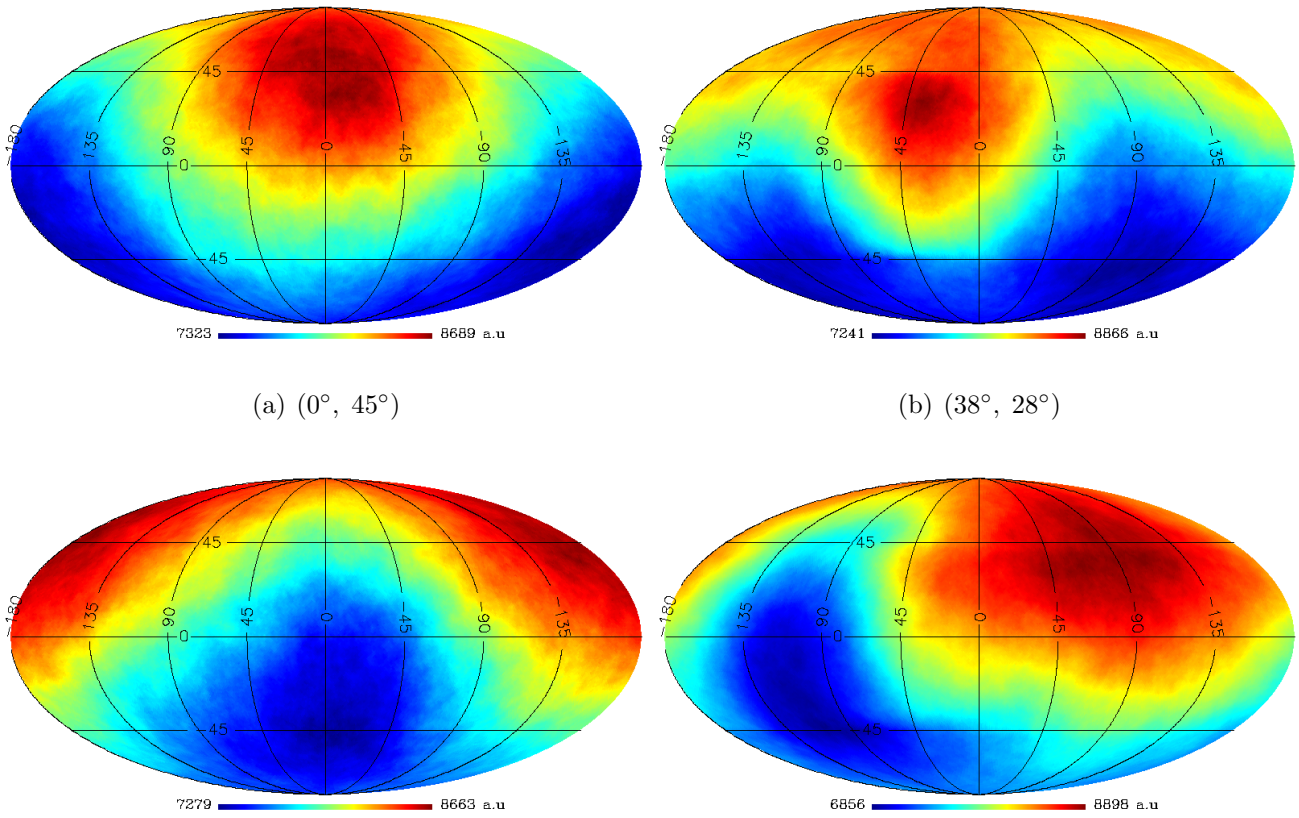

(a) (0°, 45°)

(b) (38°, 28°)

(c) (180°, 45°)

(d) (286°, 48°)

Figure 4.7: Sky maps of the backtracked cosmic-ray distribution (right panel plots) for initial dipole orientation in different directions in the northern hemisphere (left panel plots), in equatorial coordinates (α, δ) and smoothed with a 45° top-hat filter.

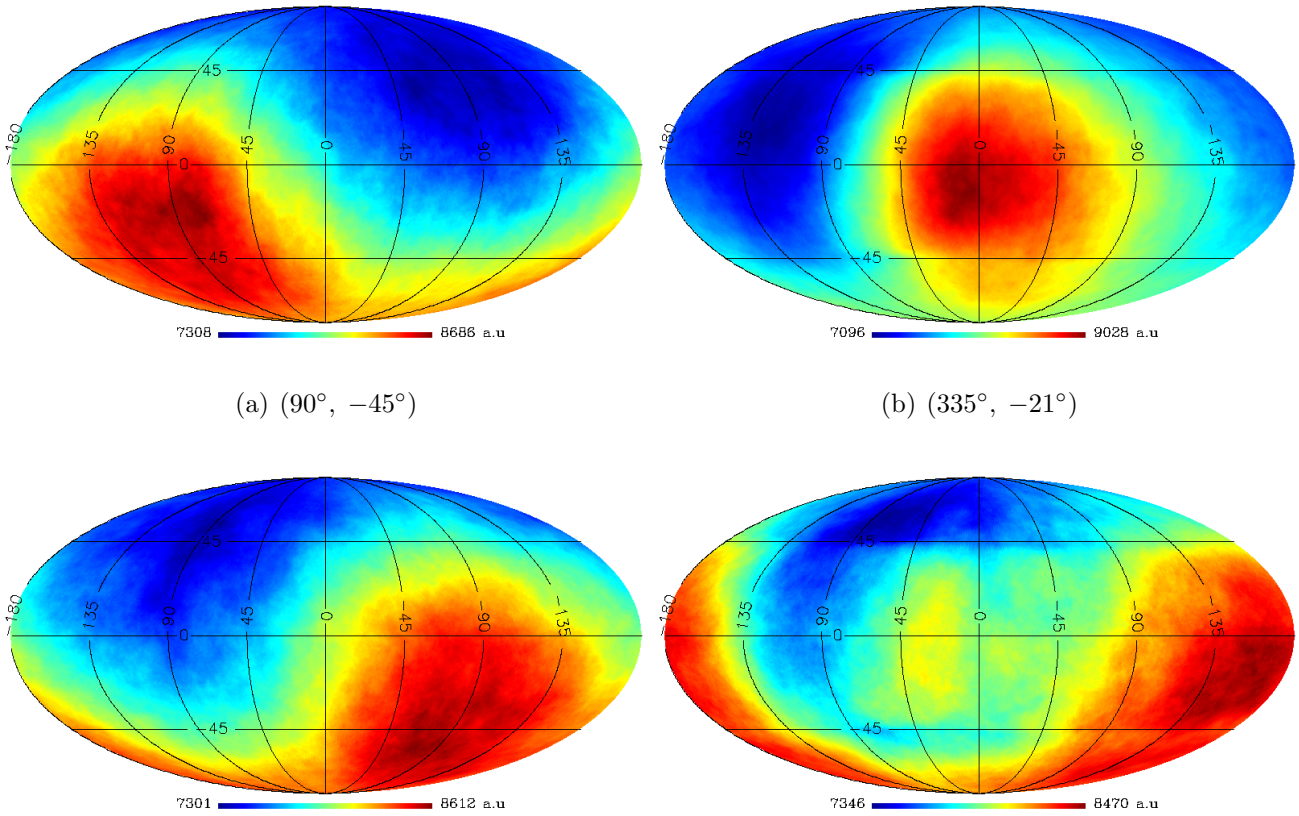

(a) (90°, −45°)

(b) (335°, −21°)

(c) (270°, −45°)

(d) (228°, −49°)

Figure 4.8: Sky maps of the backtracked cosmic-ray distribution (right panel plots) for initial dipole orientation in different directions in the southern hemisphere (left panel plots), in equatorial coordinates (α, δ) and smoothed with a 45° top-hat filter.

$(\Delta_0, \alpha_0, \delta_0)$	$(\Delta_f, \alpha_f, \delta_f)$	$1 - \Delta_f/\Delta_0$	ang. desv.
(0.10, 0°, 45°)	(0.10, 38°, 28°)	1.1×10^{-4}	28°
(0.10, 180°, 45°)	(0.14, 286°, 48°)	0.4	71°
(0.10, 90°, −45°)	(0.12, 335°, −21°)	0.2	91°
(0.10, 270°, −45°)	(0.05, 228°, −49°)	0.5	30°

Table 4.1: Results of backtracking studies of the influence of the galactic magnetic field in both amplitude and direction of the starting distribution. The subscript 0 indicates quantities measured on Earth and the subscript f those measured at the entrance of the galaxy halo.

Chapter 5

Extragalactic propagation in the absence of magnetic fields

At this point of the study, we will use rectilinear propagation in the absence of any magnetic field to simulate the cosmic-ray trajectories from the sources to the point of detection at Earth. This approach is consistent with a scenario in which cosmic magnetic fields can be neglected, which is the case when either the intensity of the extragalactic magnetic fields is negligible or the proximity of the sources and the large energies of the arriving cosmic rays allow ruling out any significant effect of magnetic deflections. Sections 5.1 and 5.2 introduce the astrophysical model and statistical estimator to be used throughout this study. In section 5.3, the fitting procedure is applied to the real Auger data in order to find the astrophysical scenarios that best fit the data.

5.1 The astrophysical model

The cosmic-ray extragalactic propagation, including the processes of energy loss and production of secondary particles, was simulated using the Monte Carlo code CRPropa [79] throughout this work. In all scenarios, we considered in the simulations the main processes of energy loss that take place as a result of the interaction of the cosmic rays with the radiation fields, namely, photopion production, photodisintegration and pair creation. Also energy losses by adiabatic expansion of the Universe were taken into account in the simulations. In this first scenario there is no magnetic field involved in the propagation, so the cosmic-ray trajectories can be considered rectilinear from the source to the point of detection, and the simulations can be tackled as 1-dimensional in effect. In the simulation, a total of 10^8 primary nuclei of charge Z are accelerated up to an energy $\sim Z \times 10^{22}$ eV and injected onto the extragalactic environment from random positions at redshift $0 \leq z \leq 1$. This scenario is consistent with a uniform and homogeneous spatial distribution of sources in comoving distance. Similar to previous works and for comparative purposes, we considered a mixed composition of ^{1}H, $^{4}_{2}$He, $^{14}_{7}$N, $^{28}_{14}$Si and $^{56}_{26}$Fe. In principle, all kinds of nuclei can be produced and accelerated at the sources. However, in our approach, considering a subset

of different representative chemical elements is sufficient to describe the main characteristics of the astrophysical scenarios we are investigating. In this approach, we injected a total of 10^8 nuclei for each chemical element, with energies ranging from 1 to $Z \times 10^4$ EeV, from which a total of $\approx 3.5 \times 10^7$ where detected at the end of their propagation with final energies above $10^{18.7}$ eV, giving a detection efficiency of 7%. Table 5.1 shows a summary of the number of cosmic rays detected with energies above $10^{18.7}$ eV, descending from each chemical element injected at source. The injection energy spectrum is modeled with a power low $\frac{dN}{dE} \propto E_0^{\gamma}$ shaped with a cut-off term depending on the magnetic rigidity $R = E_0/Z$ aimed to limit the maximum energy potentially supplied by a source to a nucleus of charge Ze. This choice is motivated by Hillas' idea [29] of an acceleration scenario related to magnetic confinement.

model	N_H	N_{He}	N_N	N_{Si}	N_{Fe}	N_T
B0nG	3.4×10^5	1.3×10^6	4.7×10^6	9.3×10^6	1.9×10^7	3.4×10^7

Table 5.1: Number of particles detected with energies above $10^{18.7}$ eV. For each chemical element a total of 10^8 a were injected at sources.

Therefore, following [81], the injection spectrum model takes the form

$$J_0(E) = \frac{dN_0}{dE} = \sum_A \frac{dN_0^A}{dE} \,, \tag{5.1}$$

where

$$\frac{dN_0^A}{dE} \equiv J_0^A(E) = j_0 f_A \left(\frac{E}{E_0}\right)^{-\gamma} \times f_{cut}(E_0, Z_A R_m) \,, \tag{5.2}$$

where A is the atomic mass number of the injected nuclei, f_A the relative fraction of the injected flux (at $E_0 = 10^{18}$ eV) corresponding to a chemical element of mass number A, j_0 the observed source luminosity and the cut-off function f_{cut} is given by:

$$f_{cut}(E_0, Z_A R_m) = \begin{cases} 1 & (E_0 < Z_A R_m) \\ \exp\left(1 - \frac{E_0}{Z_A R_m}\right) & (E_0 > Z_A R_m) \,. \end{cases} \tag{5.3}$$

Therefore, the free parameters that determine the physical properties of the sources are

- the power-law spectral index of the injection spectrum γ,
- the maximum rigidity of acceleration R_m,
- and the intrinsic luminosity of the sources j_0,
- and four of the mass fractions f_A, as the fifth one is constrained by the completeness condition $\sum_A f_A = 1$.

After injection, cosmic rays start propagating through the extragalactic space under the influence of the cosmic magnetic fields and energy radiation backgrounds. The main effect of the magnetic field is the deflection of the particles' trajectories resulting in an increment of the overall trajectory length. On the other hand, the interaction with the cosmic photon backgrounds may lead to processes of energy losses and nuclear disintegration. For protons, the energy losses are dominated by the pair production and photopion production phenomena due to the interaction mainly with the CMB. In the case of heavier nuclei, the dominant energy loss processes are photodisintegration and also pair production due to interaction predominantly with EBL photons. The nuclear interactions of the cosmic rays with the background light are simulated using Domínguez model of EBL [82] and the TALYS [83, 84] model of photodisintegration cross sections. At the end of the propagation the arriving particles that were injected at sources with energies E_{inj} and detected with energy E_{det} are recorded in a 2-dimensional grid of width $\log_{10}(E_{det}/\mathrm{EeV}) = 0.01$ and $\log_{10}(E_{inj}/\mathrm{EeV}) = 0.01$. The chemical composition of the detected particles is also stored and transformed into an estimate of $X_{\max}$ assuming the parameterization given by the hadronic interaction model EPOS-LHC [85].

5.2 The statistical estimator

In order to find the astrophysical model parameters $\boldsymbol{\theta} = \{\theta_i\}$ that best fit the data set $\mathbf{d} = \{d_i\}$, here we follow closely the procedure adopted in [81], adopting a joint likelihood composed by the following two parts:

- The likelihood related to the energy spectrum $\mathcal{L}_J(\boldsymbol{\theta}|\mathbf{d})$, linked to the energy distribution of the detected events.
- The likelihood related to the atmospheric depth of the point of maximum development of the shower $\mathcal{L}_{X_{\max}}(\boldsymbol{\theta}|\mathbf{d})$, linked to the chemical composition at detection.

The outcome of the joint likelihood [1] maximization $\mathcal{L}_J \cdot \mathcal{L}_{X_{\max}}$ gives the parameter values that describe the astrophysical scenario according to the available data.

5.2.1 Energy spectrum

The data associated with the energy spectrum were collected during the period 2004-2019 by the SD. Therefore, the number of events contained in the majority of the energy bins (except for the last two bins at the very end of the spectrum) is large enough for us to assume Gaussian statistics for the arriving flux $J = dN/dE$. In this way, the energy spectrum likelihood is constructed

[1] Since we are not assuming any prior information on the parameters $\boldsymbol{\theta}$ of the astrophysical model, we shall refer to $\mathcal{L}(\boldsymbol{\theta}|\mathbf{d})$ as a likelihood, but from the point of view of the Bayes theorem, it is really a posterior probability distribution.

assuming a Gaussian model for the fluctuations of the arriving flux of cosmic rays J detected in each energy bin:

$$\mathcal{L}_J(\boldsymbol{\theta}|\mathbf{d}) = \prod_i \frac{1}{\sqrt{2\pi\sigma_i^2}} \exp\left\{-\frac{1}{2}\left(\frac{J_i^{obs} - J_i^{\rm mod}}{\sigma_i}\right)^2\right\} , \tag{5.4}$$

where $J_i^{\rm obs}$ and $J_i^{\rm mod}$ are the observed and model-simulated flux, respectively, and σ_i is the statistical uncertainty on $J_i^{\rm obs}$.

Measurements of the arriving UHECR's energies are affected by uncertainties of the order of 10%, due to both shower-to-shower fluctuations and detector resolution effects. These can cause detected events to be reconstructed in the wrong energy bin. As a consequence of the incoming flux being a decreasing function of the energy, shower-to-shower fluctuations and finite detector resolution lead to an asymmetric migration of events when binned in terms of their reconstructed energy $E_{\rm rec}$. The effect is such that, for an arbitrary true energy E_*, due to the fluctuations, more events with $E_{\rm true} < E_*$ migrate to the region $E_{\rm rec} > E_*$, than in the opposite direction across E_*. The net result of this migration is that the reconstructed spectrum becomes harder and smoother than the true one. To take into account these experimental uncertainties and biases introduced by the process of detection and reconstruction of the events, an unfolding procedure is applied to correct the measured spectrum as follows

$$J_{\rm unf}^{\rm obs}(E) = C(E) \cdot J_{\rm fold}^{\rm obs} . \tag{5.5}$$

Here $J_{\rm fold}^{\rm obs}(E)$ is the flux measured directly, i.e, the flux calculated by dividing the raw event count in a given energy bin by the bin width and the detector exposure, whereas $J_{\rm unf}^{\rm obs}(E) = J^{\rm obs}(E)$ is the *true* flux corrected by detection effects to be matched with the prediction of the theoretical model. The correction factors are calculated assuming a priori a *true* phenomenologically modeled spectrum $J_{\rm unf}^{\rm mod}(E)$ over which a convolution procedure is applied in order to obtain a folded spectrum $J_{\rm fold}^{\rm mod}(E)$ incorporating the detector response function as follows

$$J_{\rm fold}^{\rm mod}(E_{\rm rec}) = \int_0^\infty p(E_{\rm rec}|E_{\rm true}) J_{\rm unf}^{\rm mod}(E_{\rm true}) dE_{\rm true}, \tag{5.6}$$

where

$$p(E_{\rm rec}|E_{\rm true}) = {\rm Gauss}\left(E_{\rm rec}|bE_{\rm true},\ \frac{\sigma_E}{E}E_{\rm true}\right) , \tag{5.7}$$

represents the probability of detecting an event with reconstructed energy $E_{\rm rec}$ when the true energy was $E_{\rm true}$, being b the energy bias and σ_E the SD energy resolution [81]. Using this, the correction factors are computed as

$$C(E) = \frac{J_{\rm unf}^{\rm mod}(E)}{J_{\rm fold}^{\rm mod}(E)} . \tag{5.8}$$

The quantity to be minimized in the fit is defined as the deviance

$$\mathcal{D}_J \equiv -2\ln\frac{\mathcal{L}_J}{\mathcal{L}_J^{\rm sat}} , \tag{5.9}$$

where $\mathcal{L}_J$ is the model likelihood defined in equation 5.4 and $\mathcal{L}_J^{\rm sat}$ is the likelihood of the so-called *saturated* model, that is, the one that perfectly describes the data. In this case, the saturated likelihood is obtained by making $J_i^{\rm obs} = J_i^{\rm mod}$, leading to:

$$\mathcal{L}_J^{\rm sat} = \prod_i \frac{1}{\sqrt{2\pi\sigma_i^2}} \,, \tag{5.10}$$

hence the deviance associated to the energy spectrum data $\mathcal{D}_J$ takes the form of a standard χ^2:

$$\mathcal{D}_J = \sum_i \left(\frac{J_i^{obs} - J_i^{mod}}{\sigma_i} \right)^2 . \tag{5.11}$$

5.2.2 Chemical composition

In the case of the $X_{\rm max}$ distributions, as the FD only operates $\sim 13\%$ of the time compared to the essentially 100% duty-cycle of the SD, the size of the $X_{\rm max}$ data sample is only a fraction of the energy spectrum sample. Therefore, when the data are binned using a 2D grid $(E, X_{\rm max})$, the number of events per bin is not always large enough to assume Gaussian statistics and, in this case, Poisson fluctuations must be assumed. Therefore, we can construct the $X_{\rm max}$ likelihood in the form of a multinomial distribution [81]:

$$\mathcal{L}_{X_{\rm max}}(\boldsymbol{\theta}|\mathbf{d}) = \prod_i n_i! \prod_j \frac{1}{k_{ij}!} \cdot (G_{ij})^{k_{ij}} \,, \tag{5.12}$$

where n_i is the total number of events in the $X_{\rm max}$ sample falling into the i-th energy bin, and for that same bin, k_{ij} is the corresponding number of events falling into j-th $X_{\rm max}$ bin so that $\sum_j k_{ij} = n_i$, G_{ij} is the model probability to observe an event in the reconstructed energy bin i and $X_{\rm max}$ bin j, normalized so that $\sum_j G_{ij} = 1$ for each i, and given by

$$G_{ij}(X_{\rm max}^{rec}) = \sum_A p_A \cdot g(X_{\rm max}^{rec}|E_i,\ A) \tag{5.13}$$

where $g(X_{\rm max}^{\rm rec}|E_i,\ A)$ represents a Gumbel distribution function filtered via a convolution procedure ($\otimes$) to take into account the detector response of acceptance $\mathcal{A}$ and resolution $\mathcal{R}$ (see [86] for the details)

$$g(X_{\rm max}^{rec}|E,\ A) = g(X_{\rm max}|E,\ A) \cdot \mathcal{A}(X_{\rm max}|E) \otimes \mathcal{R}(X_{\rm max}^{rec}|E,\ A) \,. \tag{5.14}$$

The functions $g(X_{\rm max}|E, A)$, in turn, were calculated using parameters determined with CONEX shower simulations [87] using the EPOS-LHC hadronic interaction model.

The deviance associated to the $X_{\rm max}$ data sample is defined similarly to the spectrum case as

$$\mathcal{D}_{X_{\rm max}} \equiv -2 \ln \frac{\mathcal{L}_{X_{\rm max}}}{\mathcal{L}_{X_{\rm max}}^{\rm sat}} \,. \tag{5.15}$$

Taking the logarithm of equation 5.12 we have

$$\ln\left(\mathcal{L}_{X_{\rm max}}\right) = \sum_i \ln n_i! - \sum_i \sum_j \ln k_{ij}! + \sum_i \sum_j k_{ij} \cdot \ln G_{ij} \tag{5.16}$$

and using Stirling's approximation we can transform the previous equation into

$$\begin{aligned}\ln\left(\mathcal{L}_{X_{\max}}\right) &= \sum_i (n_i \cdot \ln n_i - \cancel{n_i}) - \sum_i \sum_j (k_{ij} \cdot \ln k_{ij} - \cancel{k_{ij}}) + \sum_i \sum_j k_{ij} \cdot \ln G_{ij} \\ &= \sum_i n_i \cdot \ln n_i + \sum_i \sum_j k_{ij} \cdot \ln\left(\frac{G_{ij}}{k_{ij}}\right) \\ &= \sum_i \sum_j k_{ij} \ln n_i + \sum_i \sum_j k_{ij} \cdot \ln\left(\frac{G_{ij}}{k_{ij}}\right) \\ &= \sum_i \sum_j k_{ij} \ln\left(\frac{n_i \cdot G_{ij}}{k_{ij}}\right) \ .\end{aligned} \tag{5.17}$$

and the saturated likelihood corresponds to the case where $n_i \cdot G_{ij} = k_{ij}$, so that we can write

$$\mathcal{L}^{\text{sat}}_{X\max} = 1 \ , \tag{5.18}$$

with the $X_{\max}$ deviance finally given by

$$\mathcal{D}_{X_{\max}} = -2 \cdot \ln\left(\mathcal{L}_{X_{\max}}\right) = 2 \sum_{i,j} k_{ij} \cdot \ln\left(\frac{k_{ij}}{n_i \cdot G_{ij}}\right) \ . \tag{5.19}$$

Hence the total deviance takes the form

$$\mathcal{D}_{J+X_{\max}} = \mathcal{D}_J + \mathcal{D}_{X_{\max}} = \sum_i \left(\frac{J_i^{obs} - J_i^{mod}}{\sigma_i}\right)^2 + 2 \sum_{i,j} k_{ij} \cdot \ln\left(\frac{k_{ij}}{n_i \cdot G_{ij}}\right) \ . \tag{5.20}$$

5.3 Fit of the Pierre Auger energy spectrum and $X_{\max}$ data

The data set we use in this study [88] has been recorded by the Pierre Auger Observatory over a period of more than 15 years of operation. The data consist of the energy distribution of the events detected by the SD, along with the $X_{\max}$ distributions of a subset of those events that are detected simultaneously by the FD and SD. Table 5.2 shows the energy spectrum data used in this work. It consists of the values of the arriving flux J_i recorded in energy bins of width 0.1 $\log_{10}(E/\text{eV})$ with asymmetric statistical uncertainties given by the lower and upper limits J^i_{low} and J^i_{up}, respectively. Since we have assumed Gaussian statistics for the energy spectrum, we transform these asymmetric intervals into a symmetric one by calculating the standard deviation in each energy bin as

$$\sigma_i = \frac{J^i_{\text{up}} - J^i_{\text{low}}}{2} \ . \tag{5.21}$$

For each energy bin, the $X_{\max}$ data in the interval [0, 2000 g cm^{-2}] are further distributed into 100 bins of width 20 g cm^{-2}. Table 5.3 shows the total number of measured $X_{\max}$ values per energy bin and the corresponding asymmetric systematic (not statistical!) uncertainties for each

energy bin[2] . For the $X_{\rm max}$ sample, the last energy bin integrates events detected with $E > 10^{19.6}$ eV. The energy region of interest in the fit is that of $18.70 < \log_{10}(E/{\rm eV}) < 20.20$ for both the spectrum and $X_{\rm max}$ data samples. This is motivated by the fact that cosmic rays of these energies are believed to be of extragalactic origin. Therefore, the energy threshold of $10^{18.7}$ eV is chosen in order to guarantee that any galactic component of the cosmic-ray flux has become negligible at these energies.

The systematic uncertainty on $X_{\rm max}$ is not negligible and should be taken into account to get a reasonable agreement between data and model. In a similar way to [81], in the fits combining the spectrum and the $X_{\rm max}$ data, we introduce an extra fit parameter $\alpha_{\rm sys}$, measured in units of the energy-dependent systematic uncertainty $\sigma_{\rm sys}$. More precisely, when calculating the model probabilities $G_{ij}(X^{rec}_{\rm max})$, in each energy bin i, a shift $\Delta X^i_{\rm max}$ is introduced in the model-$X^{rec}_{\rm max}$ with respect to the corresponding data-$X^{rec}_{\rm max}$ in the form

$$\Delta X^i_{\rm max} = \alpha_{\rm sys}\sigma^i_{\rm sys} \ , \tag{5.22}$$

where, in this thesis, we have adopted the following convention

$$\sigma^i_{\rm sys} \equiv \frac{\sigma^i_{\rm up} - \sigma^i_{\rm low}}{2} \ . \tag{5.23}$$

In [81], an extra fit parameter dealing with systematic uncertainties is taken into account, i.e., the one related to the absolute energy scale. Their results, however, indicate best-fit systematic energy shifts consistent with zero within the statistical uncertainty. Therefore, we should not include these energy shifts here. In this thesis, in order to evince the role of $X_{\rm max}$ in breaking degeneracies in the parameters of the astrophysical models, we will perform two kinds of fits:

- spectrum-only with a maximum of 7 fitted parameters: the spectral index γ, the maximum rigidity $\log_{10}(E/{\rm eV})$, four out of five chemical fractions f_i (the fifth fraction is obtained through the normalization condition $\sum_i f_i = 1$) contributing to the injected flux and the luminosity of the sources j_0;
- spectrum+$X_{\rm max}$ with a maximum of 8 fitted parameters, due to the inclusion of the systematic shift $\Delta X_{\rm max}$.

The general procedure to find the best-fit solution starts with a 2-dimensional scan of the likelihood in the (γ, R_m) parameter space. This space was explored with a grid step $\epsilon = 0.1$ for both γ and $\log_{10}(R_m/{\rm eV})$. At the first moment, for each point in the grid, the minimum deviance is found by fixing the values of γ and R_m and fitting the remaining five/six parameters (the chemical fractions, source luminosity and, if that is the case, the $X^{rec}_{\rm max}$ systematic shift $\alpha_{\rm sys}$) of the model. All the minimizations were performed using the package Minuit [89] from CERN's ROOT framework [90]. After this initial exploratory scan is performed, and the region of minimum deviance is identified, a more detailed fit is done, now allowing all the parameters to vary. More

[2] `https://www.auger.unam.mx/AugerWiki/Phenomenology/CombinedFitDataSets` (restricted access)

specifically, in Minuit, the parameters are released in a specific order: we start with all parameters fixed, except the normalization j_0, then γ and R_m are released, and finally, all 7/8 parameters are free to vary. The minimization algorithm used during the process was Migrad.

In the minimization algorithm, the chemical fractions $\{f_i, i = 1, ..., 5\}$ are mapped into the squared Cartesian projections of a point with angular coordinates $(\varphi_1, \varphi_2, \varphi_3, \varphi_4)$ over a 5-dimensional sphere of unit radius:

$$\begin{aligned} f_1 &= \cos^2(\varphi_1) \\ f_2 &= \sin^2(\varphi_1)\cos^2(\varphi_2) \\ f_3 &= \sin^2(\varphi_1)\sin^2(\varphi_2)\cos^2(\varphi_3) \\ f_4 &= \sin^2(\varphi_1)\sin^2(\varphi_2)\sin^2(\varphi_3)\cos^2(\varphi_4) \\ f_5 &= \sin^2(\varphi_1)\sin^2(\varphi_2)\sin^2(\varphi_3)\sin^2(\varphi_4)\ , \end{aligned} \tag{5.24}$$

in such a way that now the fitting parameters handled by Minuit are the angles φ_i ranging over $0 \leq \varphi_i \leq \pi$ $(i = 1, 2, 3)$ and $0 \leq \varphi_4 < 2\pi$. In this way we guarantee that $\sum_i f_i = 1$ and $0 \leq f_i \leq 1$.

$\log_{10}(E/\text{eV})$	J [km $^{-2}$sr^{-1}yr^{-1}eV^{-1}]	J_{low}[km^{-2}sr^{-1}yr^{-1}eV^{-1}]	J_{up} [km^{-2}sr^{-1}yr^{-1}eV^{-1}]
18.75	2.1909×10^{-19}	2.1767×10^{-19}	2.2051×10^{-19}
18.85	1.2170×10^{-19}	1.2074×10^{-19}	1.2265×10^{-19}
18.95	6.8495×10^{-20}	6.7854×10^{-20}	6.9137×10^{-20}
19.05	3.7790×10^{-20}	3.7364×10^{-20}	3.8215×10^{-20}
19.15	2.0617×10^{-20}	2.0337×10^{-20}	2.0897×10^{-20}
19.25	1.0350×10^{-20}	1.0173×10^{-20}	1.0527×10^{-20}
19.35	5.3024×10^{-21}	5.1892×10^{-21}	5.4157×10^{-21}
19.45	2.5720×10^{-21}	2.5014×10^{-21}	2.6426×10^{-21}
19.55	1.2975×10^{-21}	1.2525×10^{-21}	1.3425×10^{-21}
19.65	5.8195×10^{-22}	5.5478×10^{-22}	6.0913×10^{-22}
19.75	2.0190×10^{-22}	1.8753×10^{-22}	2.1627×10^{-22}
19.85	7.1988×10^{-23}	6.4306×10^{-23}	7.9669×10^{-23}
19.95	1.3062×10^{-23}	9.9255×10^{-24}	1.6199×10^{-23}
20.05	4.5748×10^{-24}	2.8066×10^{-24}	6.3429×10^{-24}
20.15	2.9294×10^{-24}	1.7721×10^{-24}	4.6702×10^{-24}

Table 5.2: Energy spectrum data sample used in the combined fit [88]. For each energy bin, it is shown the center of the bin, the cosmic-ray flux (J), and the flux statistical uncertainties in the form of lower (J_{low}) and upper (J_{up}) limits at 68% CL.

$\log_{10}(E/\text{eV})$	$N_{X_{\max}}$	σ_{up} [g cm^{-2}]	σ_{low} [g cm^{-2}]
18.75	707	+7.428	-8.297
18.85	560	+7.585	-7.964
18.95	417	+7.773	-7.649
19.05	321	+7.971	-7.389
19.15	253	+8.183	-7.178
19.25	159	+8.412	-7.014
19.35	122	+8.642	-6.900
19.45	80	+8.870	-6.828
19.55	50	+9.143	-6.778
> 19.60	35	+9.608	-6.755

Table 5.3: Summary of some properties of the $X_{\max}$ data sample used in the combined fit [88]. For each energy bin, it is shown the center of the bin, the number of events, and the upper (σ_{up}) and lower (σ_{low}) boundaries of the systematic uncertainty on $X_{\max}$.

5.3.1 Astrophysical scenarios consistent with the Auger energy spectrum data

Figure 5.1 shows a 2-dimensional likelihood scan in the (γ, R_m) parameter space, using only the energy spectrum data. This scan is obtained by fixing the values of the spectral index and maximum rigidity at each point in the (γ, R_m) parameter space and fitting the remaining parameters of the model, namely, four out of five chemical fractions and the luminosity of the sources. Hereafter, the luminosity of the source will be treated as a mere overall normalization factor, adjusted to match the Auger statistics. Therefore, we will not analyze the physical implications of this parameter value in our astrophysical model. In the same figure 5.1, two local minima can be seen appearing at $(\gamma, R_m) = (2.12, 10^{19.67}\,\text{eV})$, which we shall label as B0nG-M1 and $(\gamma, R_m) = (1.50, 10^{18.69}\,\text{eV})$, which we shall label as B0nG-M2.

model	γ	$\log_{10}(R_m/\text{EeV})$	j_0 $[au]$	f_{H} [%]	f_{He} [%]	f_{N} [%]	f_{Si} [%]	f_{Fe} [%]	D_J
B0nG-M1	2.12	1.67	18.42	15	18	0.2	49	17	36
B0nG-M2	1.50	0.60	18.69	19	0	9	70	2	136

Table 5.4: Best-fit values for an astrophysical scenario with extragalactic propagation in the absence of magnetic fields and using only the Auger energy spectrum data.

Table 7.1 shows the parameter values of the models found at the regions of local minima. It is worth noticing that the model with the higher magnetic rigidity B0nG-M1 has a relevant contribution of Iron, in contrast with the lower rigidity model B0nG-M2.

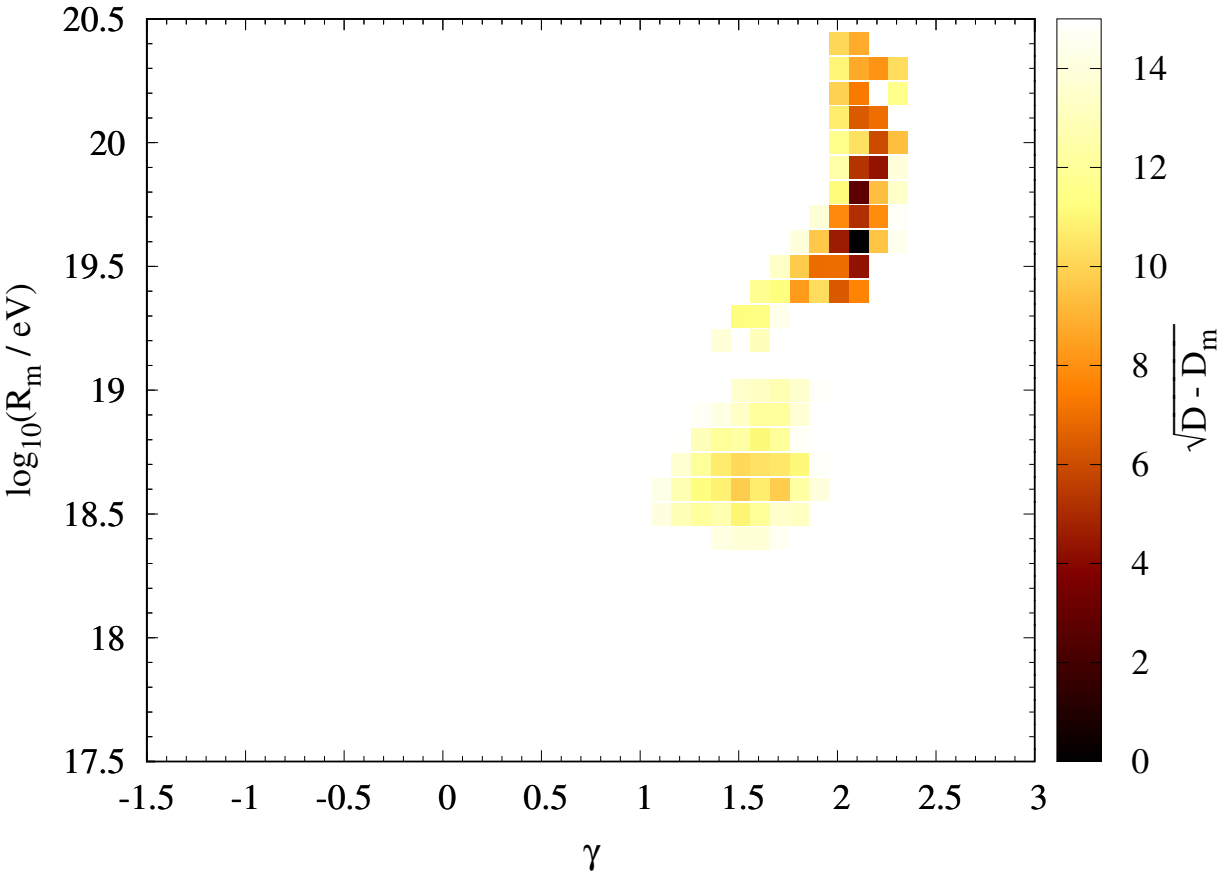

Figure 5.1: Likelihood scan using the Auger energy spectrum data for an astrophysical model constructed with extragalactic propagation in the absence of magnetic fields. The color scale shows the deviance $\sqrt{D - D_m}$, where D_m is the minimum deviance of the scan, for each point in the (γ, R_m) parameter space.

Figure 5.2 shows the energy spectrum predicted by the models B0nG-M1 and B0nG-M2. Despite the fact that the overall energy spectrum is well reproduced by both models, B0nG-M1 presents a dominant proton component of the arriving flux at the highest energies, which is in tension with previous results related to mass composition [91] pointing to a mixed composition of the flux at the end of the spectrum. For example, figure 5.3 shows the results found in [81] regarding the $X_{\rm max}$ distributions. It can be appreciated how the Auger data hints at a heavier composition at the end of the spectrum.

5.3.2 Astrophysical scenarios consistent with the Auger energy spectrum and $X_{\rm max}$ data

Figure 7.1 shows the result of a likelihood scan performed with the inclusion of the $X_{\rm max}$ data sample. Notice how the region of minima at values that appears when only the energy spectrum information is used, around ($\gamma \sim 2.0, R_m > 10^{19}\,$eV), vanishes when the $X_{\rm max}$ data sample is introduced in the likelihood, thus restricting the region of local minima to values ($\gamma \lesssim 2.0, R_m \lesssim$

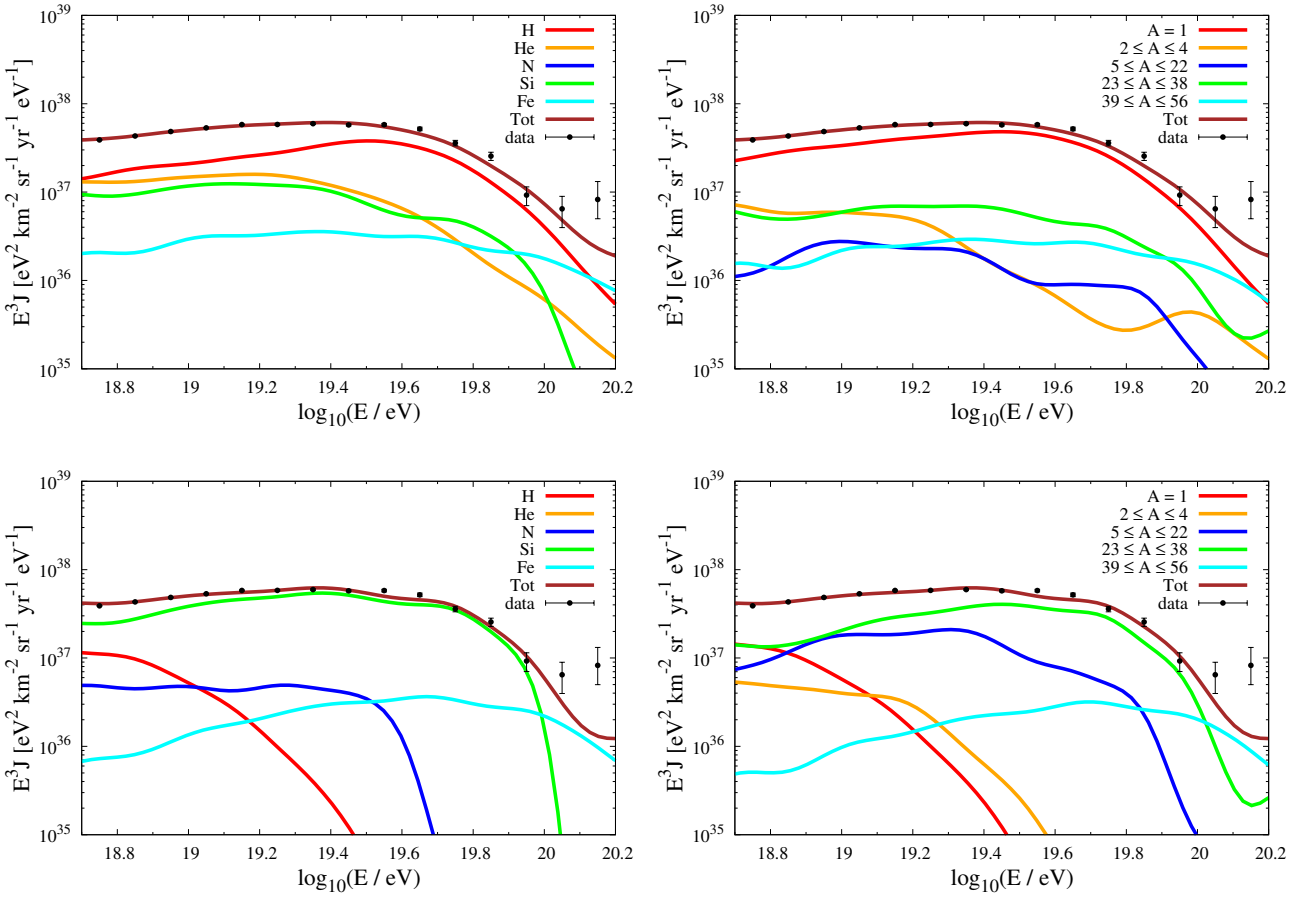

Figure 5.2: B0nG-M1 (top) and B0nG-M2 (bottom) energy spectrum models split by chemical contribution at the sources (left) and mass composition at detection (right).

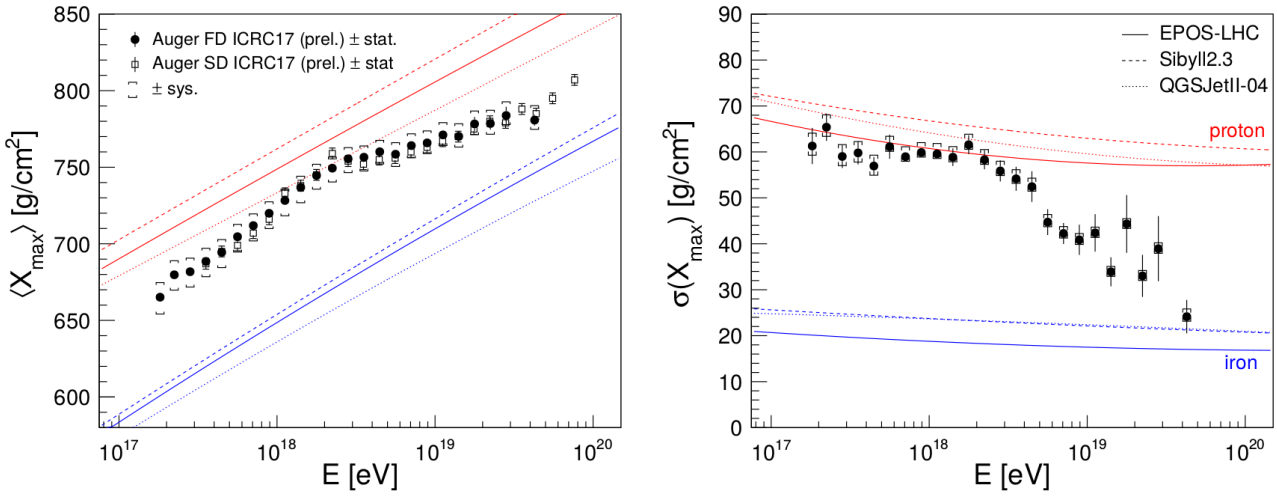

Figure 5.3: Average and standard deviation of the X_{max} distribution as predicted assuming EPOS-LHC hadronic interactions in the atmosphere. Taken from [49].

10^{19}).

Table 7.2 shows the parameter values found at the point of minimum deviance of the likelihood

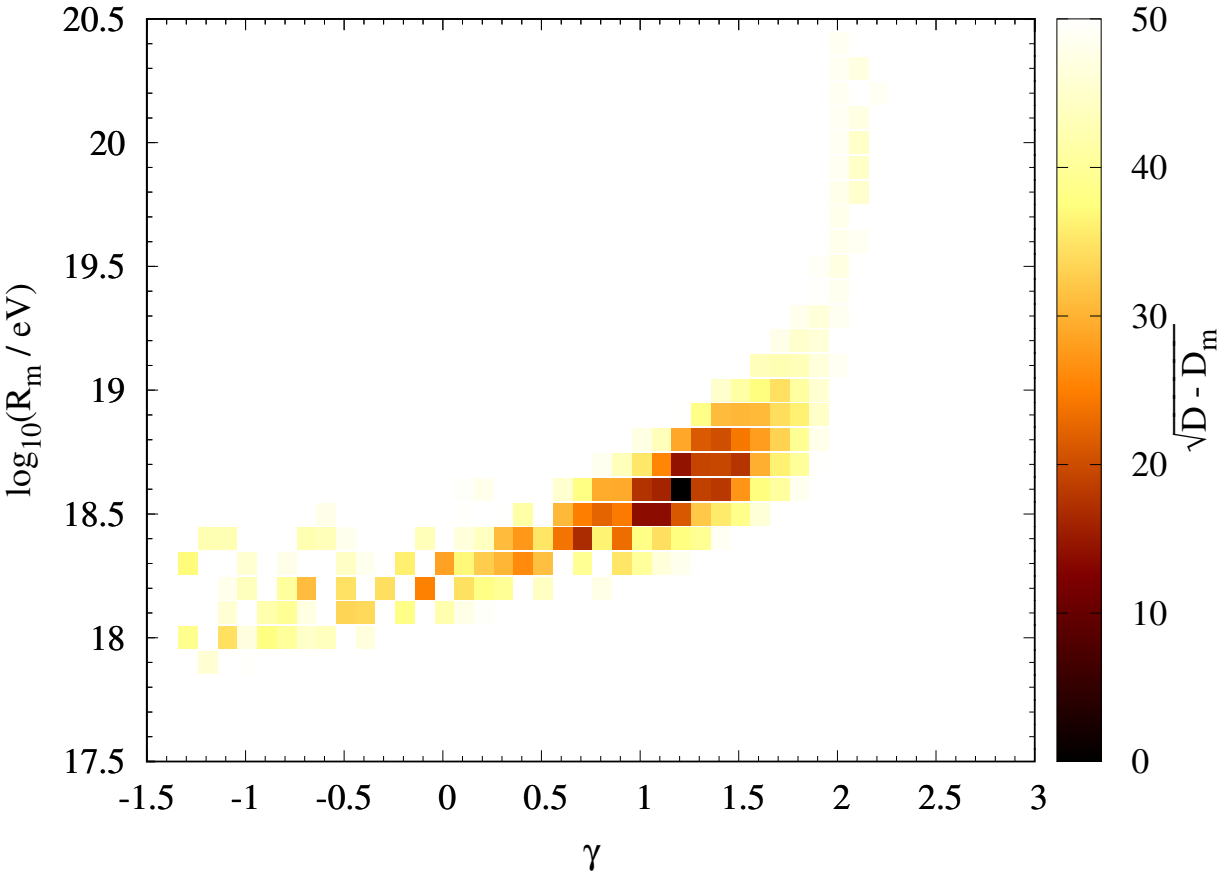

Figure 5.4: Likelihood scan performed using the Auger energy spectrum and $X_{\rm max}$ data with an astrophysical model of extragalactic propagation in the absence of magnetic fields. The color code shows the deviance $\sqrt{D - D_m}$, where D_m is the minimum deviance of the scan, for each point in the (γ, R_m) parameters space.

model	γ	$\log_{10}(R_m/\mathrm{EeV})$	j_0 $[au]$	$f_{\rm H}$ [%]	$f_{\rm He}$ [%]	$f_{\rm N}$ [%]	$f_{\rm Si}$ [%]	$f_{\rm Fe}$ [%]	α_{sys}	$D_{J+X_{\rm max}}$
B0nG-M3	1.21	0.61	19.10	0	21	32	45	1	1.26	1212

Table 5.5: Best-fit values for an astrophysical scenario with extragalactic propagation in the absence of magnetic fields and using the combined spectrum+$X_{\rm max}$ Auger data.

scan computed using the Auger energy spectrum+$X_{\rm max}$ data. We shall label this set of parameters B0nG-M3. Figures 5.5 and 5.6 show the energy spectrum and $X_{\rm max}$ distributions predicted by B0nG-M3. We can see that the proton component is relevant only for the lowest energies and the arriving flux at the highest energies presents a mixed heavier composition. Therefore we can say that even though the energy spectrum is well reproduced by models with values of magnetic rigidity above 10^{19} eV, the $X_{\rm max}$ data is crucial to discard these models in favour of models with lower magnetic rigidity.

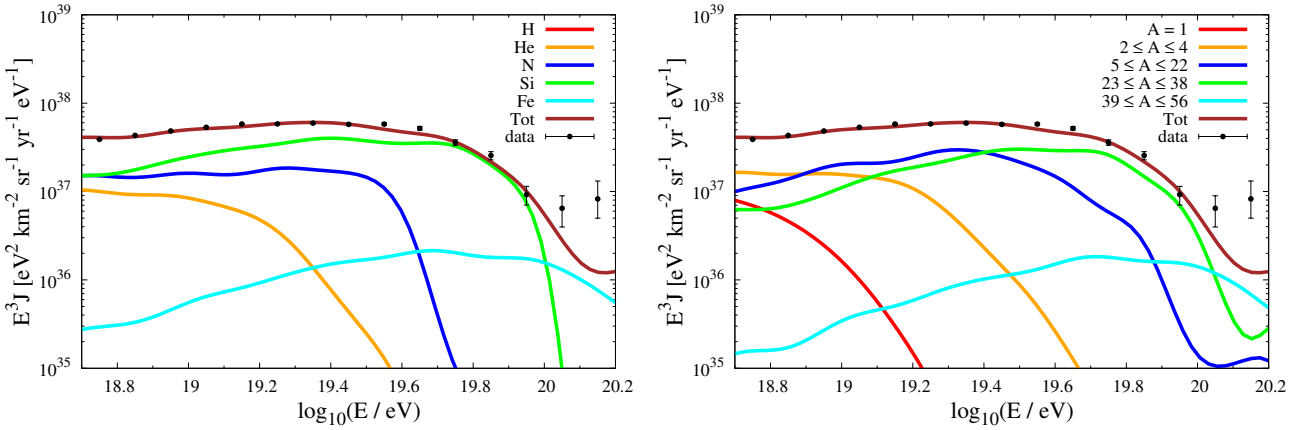

Figure 5.5: B0nG-M3 energy spectrum model divided by chemical contribution at source (left) and mass composition at detection (right).

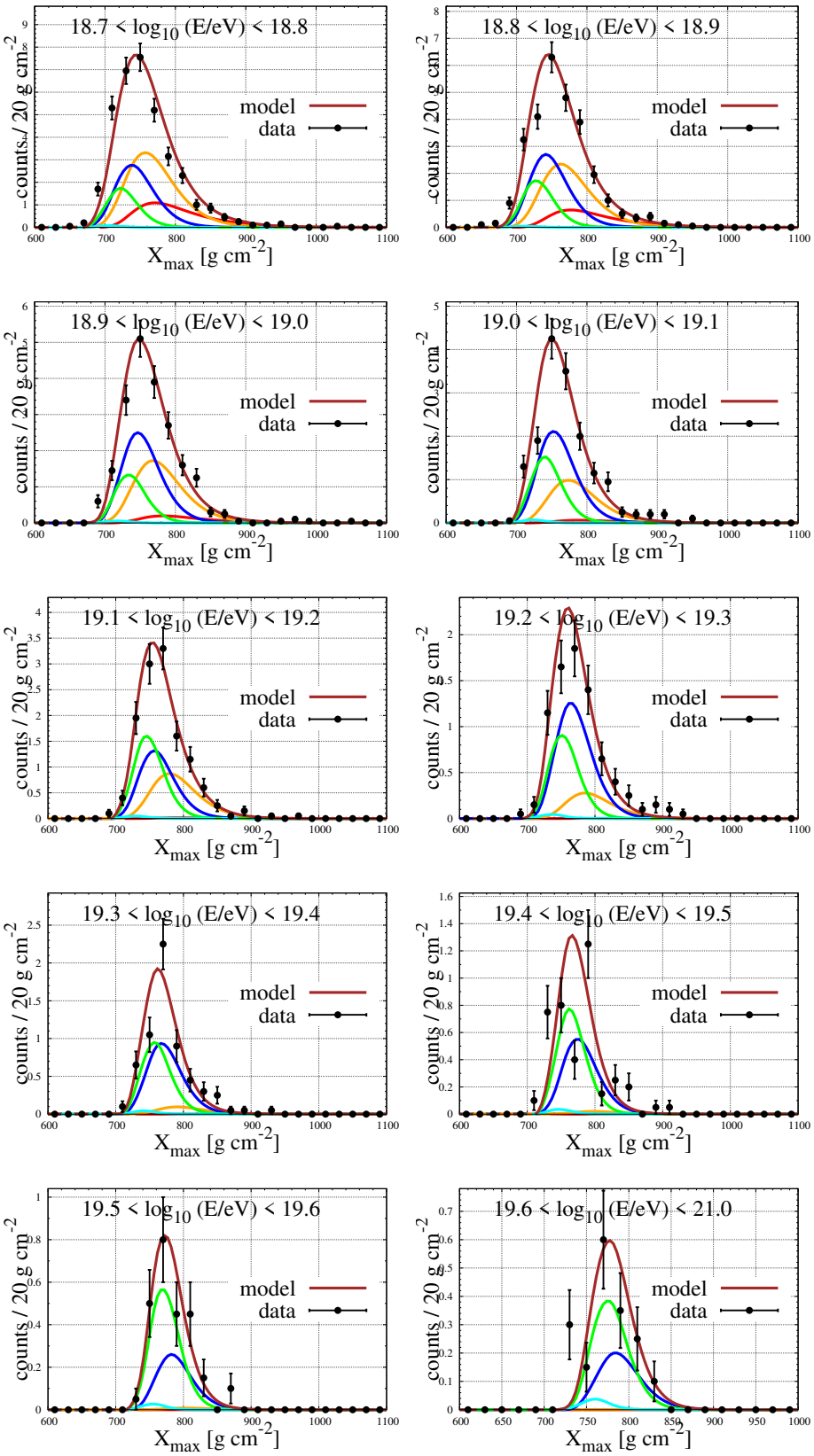

Figure 5.6: B0nG-M3 $X_{\max}$ distribution model divided by mass composition at detection. Partial distributions are grouped according to the mass number similarly as in previous figures: $A = 1$ (red), $2 \leq A \leq 4$ (orange), $5 \leq A \leq 22$ (blue), $23 \leq A \leq 38$ (green), $39 \leq A \leq 56$ (cyan), total (brown).

Chapter 6

Extragalactic propagation under the influence of cosmic magnetic fields

The influence of cosmic magnetic fields has an impact not only on the trajectory of the particles via Lorentz deflections but also on the energy spectrum detected. This happens because the cosmic-ray trajectories to the Earth increase when the particles are deflected by the magnetic field, leading to an increase in the propagation time and the probability of suffering energy losses in the interaction with the radiation fields. In this chapter, we explore astrophysical scenarios of extragalactic propagation of cosmic rays under the influence of the energy-loss processes and the effect of magnetic deflection with different models of cosmic magnetic fields. Consistency of these scenarios with the combined data set of the spectrum and $X_{\max}$ distributions measured by the Pierre Auger Observatory is also checked.

6.1 Extragalactic propagation in an MHD-simulated cosmic magnetic field.

In order to explore a realistic scenario,instead of a homogeneous magnetic field, we simulate the extragalactic propagation of cosmic rays using cosmic magnetic field (CMF) models for the local universe obtained in [92] through magneto-hydrodynamical (MHD) cosmological simulations. In general, these MHD CMF models are obtained following a dynamical evolution of dark and baryonic matter coupled since the early universe, constrained with observational data that resemble the local universe in order to follow the evolution of the magnetic fields of primordial or another origin that are amplified during structure formation and by different dynamical processes. In this work, we explored the *astrophysical* and *primordial* models obtained in [92]. The *astrophysical* model considers a scenario in which the CMF is generated by the release of over-pressurized outflows of thermal energy and the corresponding magnetic feedback in halo regions where the physical gas number density exceeds a critical value of 10^{-2} cm^{-3}. The *primordial* model simulates an amplification scenario of a primordial magnetic field of strength 0.1 nG along each cartesian

direction, starting at $z = 60$. Specific details of the simulations carried out to obtain these CMF models can be found in [92]. Figure 6.1 shows the intensity $B(\mathbf{x})$ profile of these two models in the galaxy vicinity.

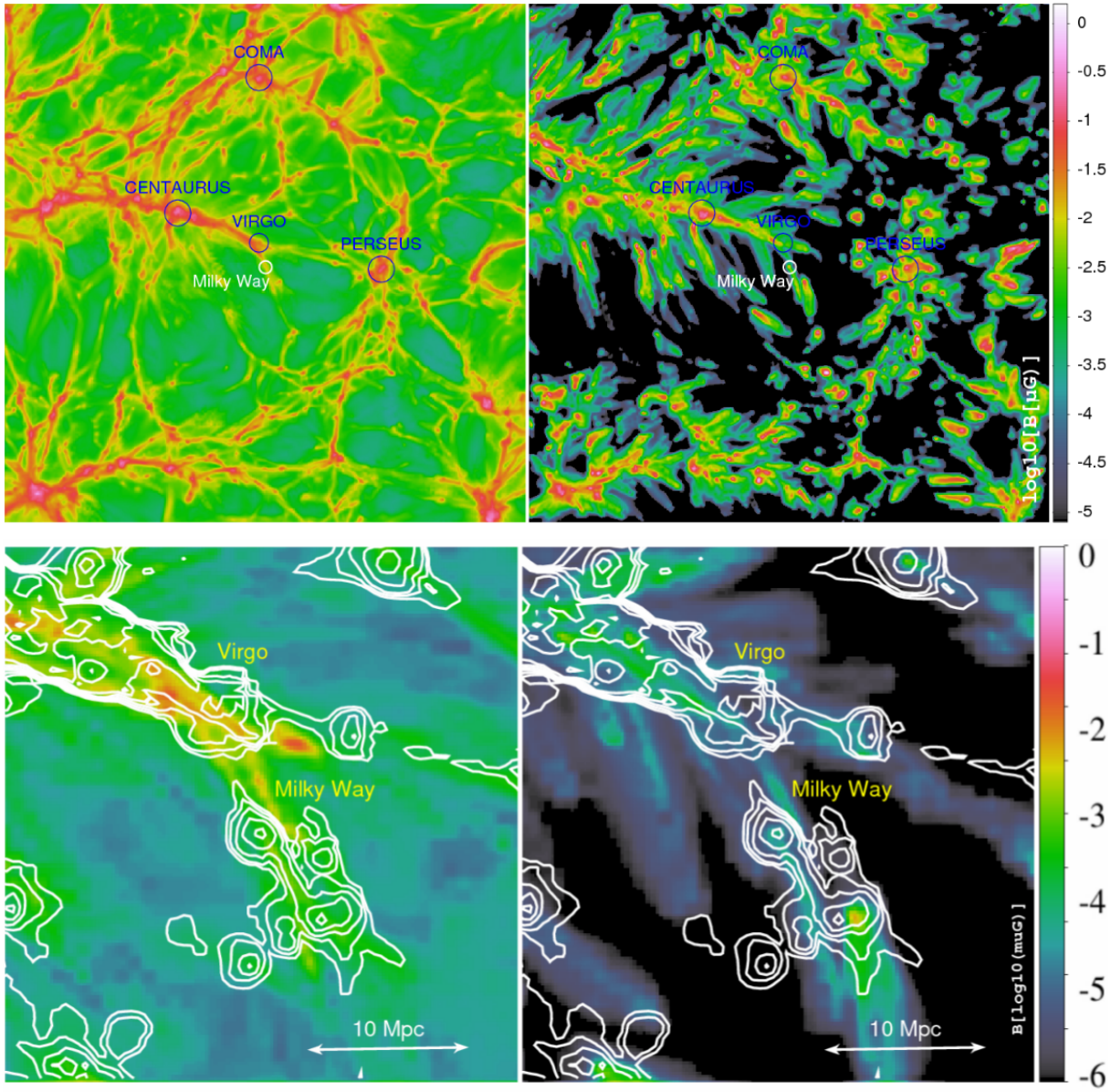

Figure 6.1: Intensity $B(X, Y)$ profile of the MHD-simulated CMFs *primordial* (left) and *astrophysical* (right) models at $z = 0$. Magnetic field intensities are in μG and color bars show a logarithmic scale. The X and Y coordinates are the super-galactic coordinates. Taken from [92].

Because now we are interested in exploring the effects of magnetic deflections, the cosmic-ray extragalactic propagation, in this scenario, is 3-dimensional in nature, again, using the CRPropa code [79]. In this case, the volume of the simulation was chosen as a 3-dimensional box of dimensions $250 \times 250 \times 250$ Mpc in comoving coordinates, embedded in the cosmic magnetic field. As we are interested only in extragalactic propagation, the detector was set as a sphere radius 20 kpc, located at the center of the box to emulate the border of the galaxy. The cosmic rays

model	N_H	N_{He}	N_N	N_{Si}	N_{Fe}	N_T
MHDAstro	4.8×10^4	1.8×10^5	4.6×10^5	5.9×10^5	5.6×10^5	1.8×10^6
MHDPrimo	5.8×10^3	2.1×10^4	5.5×10^4	7.1×10^4	6.8×10^4	2.2×10^5

Table 6.1: Number of particles detected with energies above $10^{18.7}$ eV. For each chemical element a total of 10^8 and 2×10^7 events were simulated for the *astrophysical* and *primordial* CMF models, respectively.

are accelerated up to an energy $\sim Z \times 10^{22}$ eV and injected into the extragalactic environment from random positions inside the box. Since the size of the detection sphere is small compared to that of the total simulation box, in order to increase the detection efficiency, periodic boundary conditions were adopted in CRPropa through the PeriodicBox option [1], in such a way that every time a particle crosses the boundaries of the simulation volume, it is re-injected at the opposite side of the box. In this scenario, for each chemical element injected by the sources, we simulated 10^8 and 2×10^7 events for the *astrophysical* and *primordial* CMF models, respectively. In this case, we achieved a detection efficiency of about 0.4%. Table 6.1 shows a summary of the number of cosmic rays detected with energies above $10^{18.7}$ eV, coming from a given chemical element injected by the source (the "parent" particle).

Figure 6.2 and 6.3 shows the likelihood scan performed using the energy spectrum and the $X_{\max}$ data sample for the two magnetic field models considered. In these astrophysical scenarios, the region of local minima points to models with a harder injection spectrum and lower magnetic rigidity compared to the scenario of 1-dimensional propagation. Table 6.2 shows the best-fit parameter values for the two scenarios explored, namely MHDAstro and MHDPrimo, constructed with extragalactic propagation under the influence of the MHD-simulated CMFs *astrophysical* and *primordial* models.

model	γ	$\log_{10}(R_m/\mathrm{EeV})$	j_0 $[au]$	f_{H} [%]	f_{He} [%]	f_{N} [%]	f_{Si} [%]	f_{Fe} [%]	α_{sys}	$D_{J+X_{\max}}$
MHDAstro	-0.31	0.29	21.12	0	11	74	14	1	1.25	916
MHDPrimo	-0.49	0.25	19.81	1	83	11	4	1	1.23	2556

Table 6.2: Best fit parameter values for the astrophysical scenarios of extragalactic propagation in an MHD-simulated magnetic field.

Figure 6.4 shows the comparison of the measured energy spectrum with model predictions using the best-fit solutions of table 6.2. The total flux on Earth was divided both by the chemical composition at the injection point (top panels) and on Earth (bottom plots). As in the 1D case, the end of the energy spectrum predicted by the models is dominated by a mixed chemical composition on Earth in order for the predictions to be consistent with the $X_{\max}$ data. Such consistency can in fact be appreciated in figures 6.5 and 6.6, where the $X_{\max}$ distributions of the Pierre Auger data sample are compared to the prediction of MHDAstro and MHDPrimo, respectively. The predicted

[1] https://crpropa.github.io/CRPropa3/

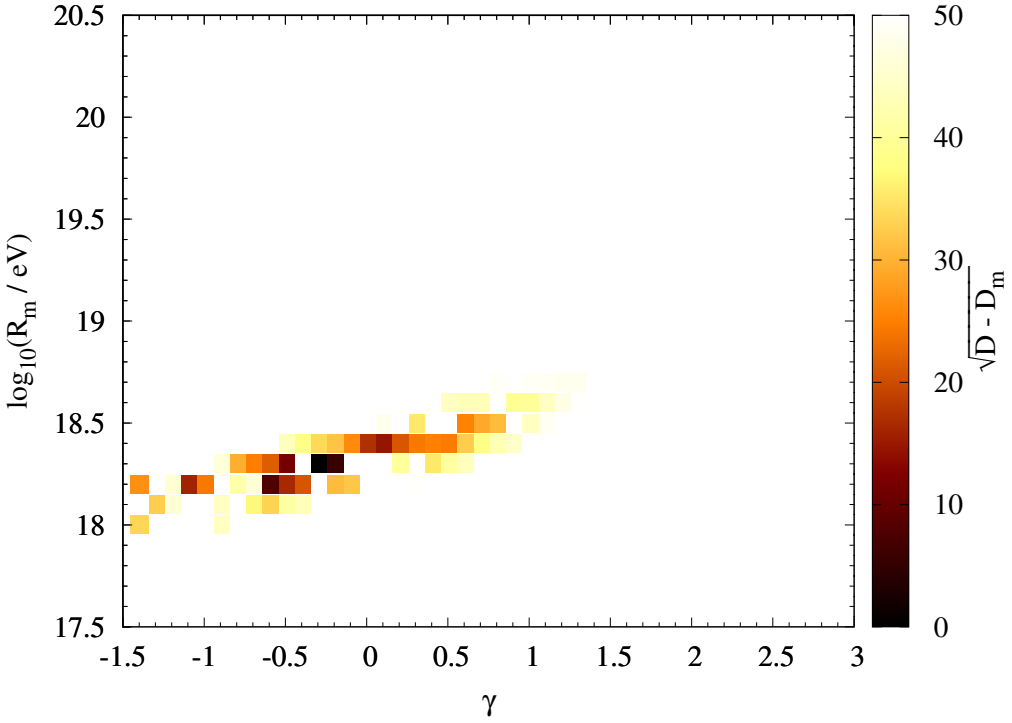

Figure 6.2: Likelihood scan using the energy spectrum and $X_{\max}$ data with an astrophysical scenario of extragalactic propagation in an MHD-simulated magnetic field with the *astrophysical* model. The color code shows the deviance $\sqrt{D - D_m}$, where D_m is the minimum deviance of the scan, for each point in the (γ, R_m) parameters space.

$X_{\max}$ distributions are divided into 10 energy bins and further decomposed into their chemical components on Earth.

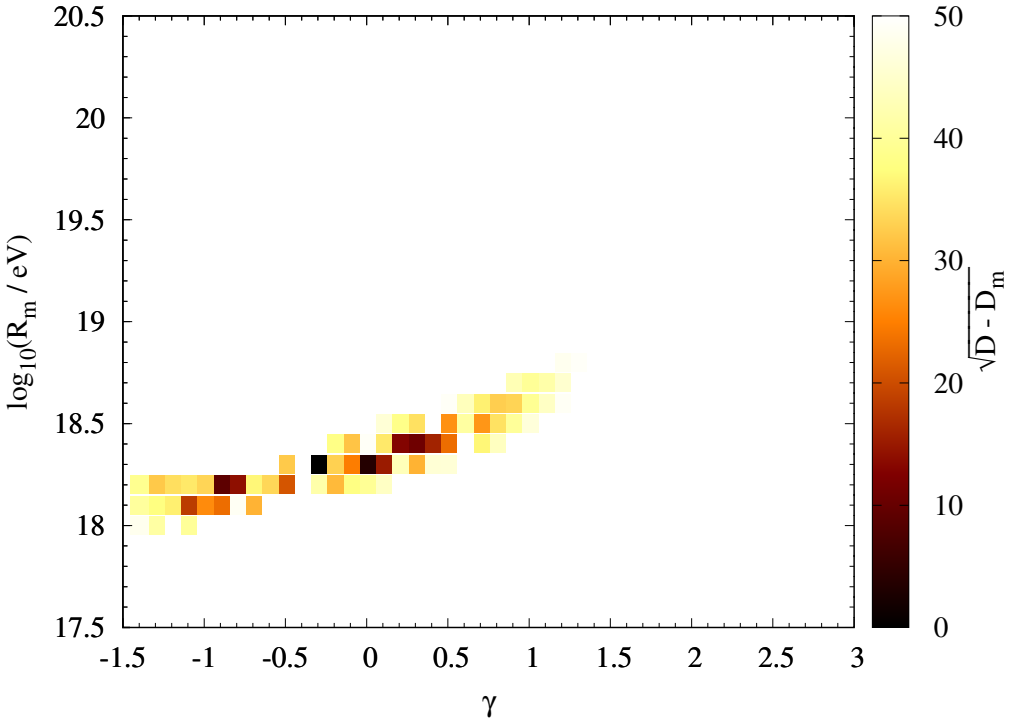

Figure 6.3: Likelihood scan using the energy spectrum and $X_{\max}$ data with an astrophysical scenario of extragalactic propagation in an MHD-simulated magnetic field with the *primordial* model. The color code shows the deviance $\sqrt{D - D_m}$, where D_m is the minimum deviance of the scan, for each point in the (γ, R_m) parameters space.

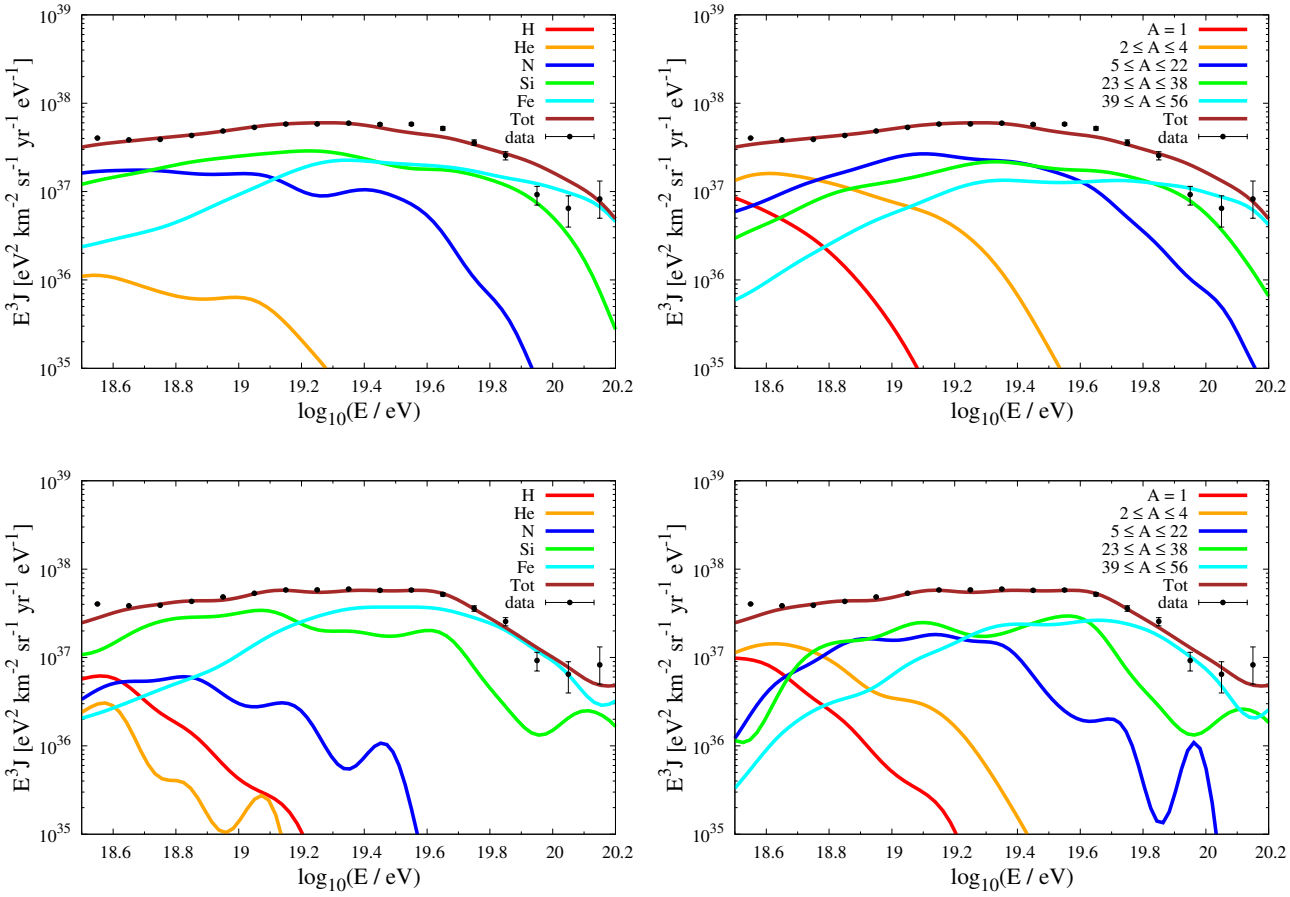

Figure 6.4: MHDAstro (top) and MHDPrimo (bottom) energy spectrum models divided by chemical contribution at source (left) and composition at detection (right).

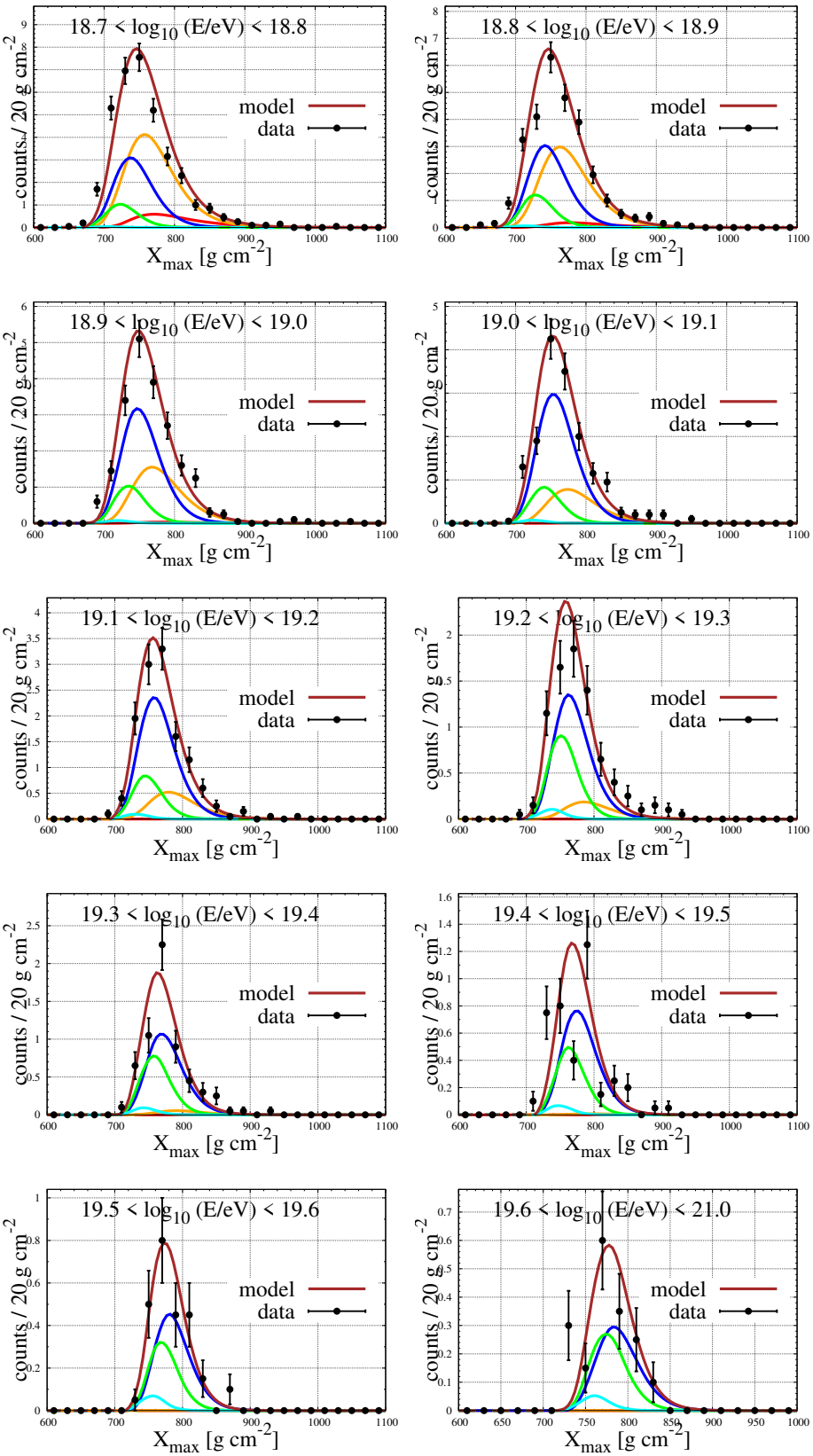

Figure 6.5: MHDAstroM3 $X_{\max}$ distributions divided by chemical composition at detection. Partial distributions are grouped according to the mass number similarly as in previous figures: $A = 1$ (red), $2 \leq A \leq 4$ (orange), $5 \leq A \leq 22$ (blue), $23 \leq A \leq 38$ (green), $39 \leq A \leq 56$ (cyan), total (brown).

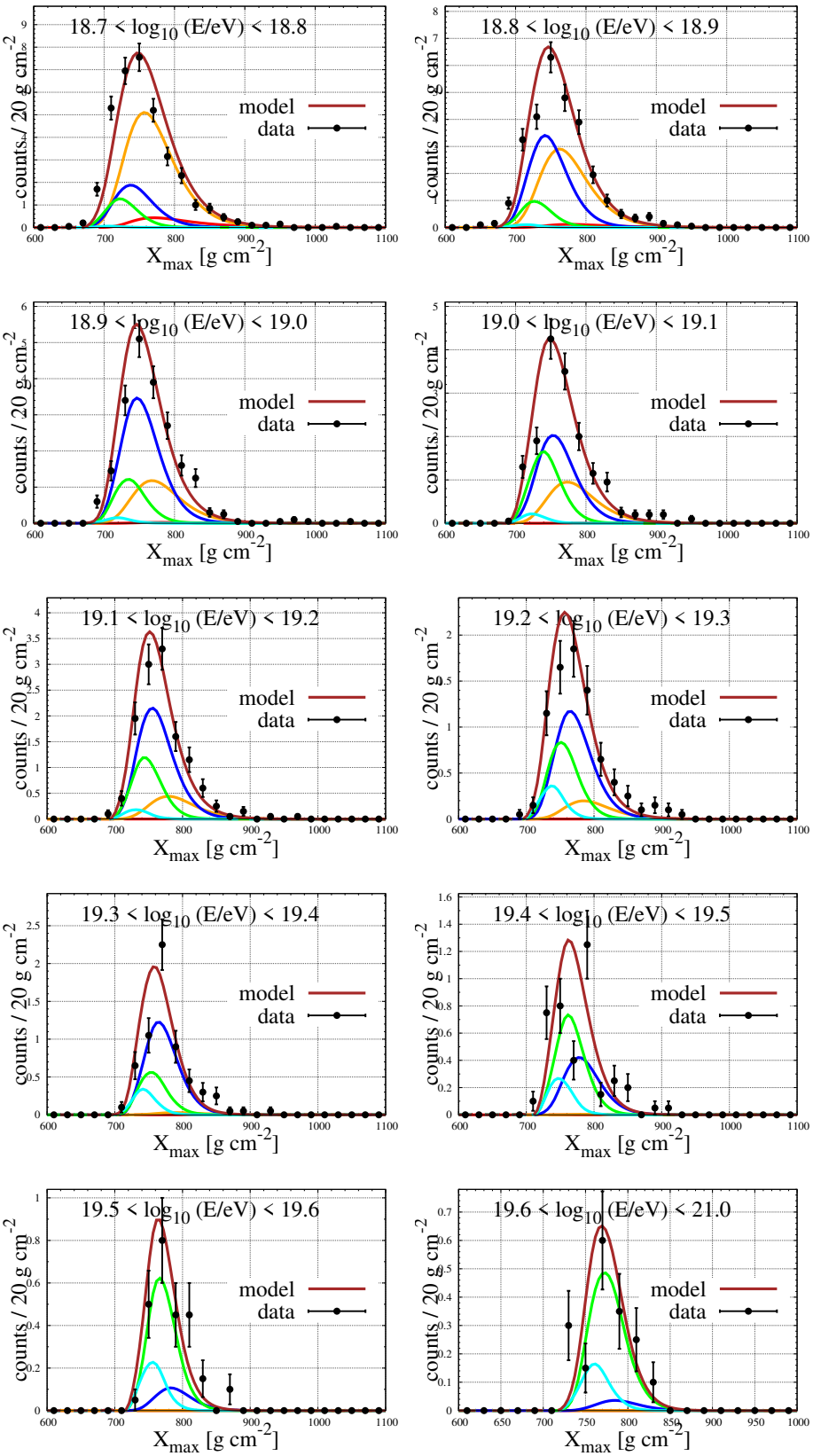

Figure 6.6: MHDPrimoM3 $X_{\max}$ distributions divided by chemical composition at detection. Partial distributions are grouped according to the mass number similarly as in previous figures: $A = 1$ (red), $2 \leq A \leq 4$ (orange), $5 \leq A \leq 22$ (blue), $23 \leq A \leq 38$ (green), $39 \leq A \leq 56$ (cyan), total (brown).

Chapter 7

Results and Implications

Throughout this work, we searched for astrophysical models of the origin and propagation of UHECRs consistent with the energy spectrum and $X_{\rm max}$ data collected by the Pierre Auger Observatory over a period of ~ 15 years of operation. We also explored scenarios where large-scale anisotropy patterns arise due to the combined effects of source spatial distributions and extragalactic magnetic deflections.

Regarding the anisotropy studies, chapter 4 presented an analysis of the evolution of the dipolar amplitude in the flux of cosmic rays propagating through the extragalactic space under the influence of magnetic fields and energy losses. To do that, simulations of the propagation of charged particles were made using the Monte Carlo code CRPropa [79], and different configurations of the extragalactic cosmic-ray sources were explored. In a scenario where the total cosmic-ray flux originates from a set of different sources, we performed an analysis of the evolution of the dipolar amplitude with energy. We explored the behavior of the dipole amplitude with the total number of sources homogeneously distributed, or equivalently, with the distance to the farthest source. In this case, the amplitude decreases with the incorporation of new sources farther and farther away. That happens because, as the number of sources increases, the distribution becomes more homogeneous at large scales and the anisotropies are almost completely determined by the nearest sources and their spatial distribution. We found that the distance beyond which the increment of new sources does not considerably affect the global anisotropy amplitude is around 700 Mpc, for a broad energy range above 1 EeV. Different source densities and magnetic field magnitudes were explored, with a high-density scenario represented by 10^{-4} Mpc^{-3} and a low-density one by $\rho = 10^{-5}$ Mpc^{-3}, whereas magnetic fields with $B_{\rm rms} = 1$ nG and 3 nG were treated. The low-density and small magnetic field RMS amplitude scenarios lead to larger dipole amplitudes as compared to the high-density and large magnetic field amplitude case.

In section 4.2 the influence of the galactic magnetic field (according to the JF12 model [39, 40]) on an incoming cosmic-ray flux having a dipolar anisotropy pattern was also explored. We found that the relative change $(1 - \Delta_f/\Delta_0)$ between the original dipole amplitude at the border of the galaxy Δ_f and that detected on Earth Δ_0 can reach values of up to $\simeq 50\%$, whereas the dipole direction can suffer deflections of several tens of degrees. The conclusions at this point are

very general as we explored a limited number of scenarios of dipole amplitude and orientation. However, we can affirm that the galactic magnetic field has a major impact on both the amplitude and direction of a potential dipolar anisotropy in the arrival directions distribution of UHECRs.

Regarding the description of the energy spectrum and $X_{\max}$ distributions of the Pierre Auger Observatory, two different scenarios of extragalactic propagation of the cosmic rays were explored. Similar to previous studies [81], the first scenario considered was the extragalactic propagation in the absence of magnetic fields using 1-dimensional (1D) simulations in CRPropa. Tables 7.1 and 7.2 show the best-fit values of the astrophysical models found in this scenario, when only the energy spectrum data are considered in the fit (B0nG-M1 and B0nG-M2 models) and when the $X_{\max}$ data sample is incorporated through a combined fit (B0nG-M3 model). As shown in figure 5.1, we found that the energy spectrum data can be well described by models with parameter values in a wide region of the (γ, R_m) parameter space, in particular, an important region of local minima, with low values of deviance, appears for rigidities $R_m > 10^{19}$ eV. We also found that the energy spectrum predicted by the best-fit models of higher magnetic rigidity presents a dominant proton component at the highest energies, a result which is in tension with the $X_{\max}$ distributions measured by the Pierre Auger as illustrated in figure 5.3 and [49]. In the case of the spectrum+$X_{\max}$ combined fit, we found that, as shown in figure 7.1, with the inclusion of the $X_{\max}$ information, the hierarchy of the regions of minimum deviance flips and the models with higher magnetic rigidity are discarded in favor of those with $R_m \lesssim 10^{19}$ eV, and, of course, a chemical composition on Earth more consistent with the data. The results obtained in this 1D scenario are consistent with those of previous studies [81]. For comparison, figure 7.2 shows the likelihood scan obtained in [81], where the reference model was constructed using the propagation code SimProp [93] (instead of CRPropa), and Gilmore EBL model [4] (instead of Dominguez [82]). Moreover, the energy spectrum deviance in [81] was calculated by comparing the model to the data at the level of shower counts per energy bin with a Poisson-based likelihood, instead of the Gaussian-based one for the cosmic-ray flux used in this thesis. And, of course, the dataset used is slightly different due to the extra events of the 2019 sample used in this work with respect to 2017. Despite these differences in the general procedure, we can see a similar correlation between γ and R_m with the region of best-fit located at $\gamma \approx 1$ and $R_m \simeq 10^{18.7}$ eV.

model	γ	$\log_{10}(R_m/\mathrm{EeV})$	j_0 $[au]$	f_{H} [%]	f_{He} [%]	f_{N} [%]	f_{Si} [%]	f_{Fe} [%]	D_J
B0nG-M1	2.12	1.67	18.42	15	18	0.2	49	17	36
B0nG-M2	1.50	0.60	18.69	19	0	9	70	2	136

Table 7.1: Best-fit values for an astrophysical scenario with extragalactic propagation in the absence of magnetic fields and using only the Auger energy spectrum data.

The second scenario explored here, which is a novel contribution of this study, considers extragalactic 3-dimensional propagation in more realistic structured CMF models, where now the effect of magnetic deflection has an impact on the particles' trajectories, leading to stronger diffusion and energy losses. Figure 7.3 shows the likelihood scan performed with the spectrum +

model	γ	$\log_{10}(R_m/\mathrm{EeV})$	j_0 $[au]$	f_{H} [%]	f_{He} [%]	f_{N} [%]	f_{Si} [%]	f_{Fe} [%]	α_{sys}	$D_{J+X_{\mathrm{max}}}$
B0nG-M3	1.21	0.61	19.10	0	21	32	45	1	1.26	1212

Table 7.2: Best-fit values for an astrophysical scenario with extragalactic propagation in the absence of magnetic fields and using the combined spectrum $+X_{\mathrm{max}}$ Auger data.

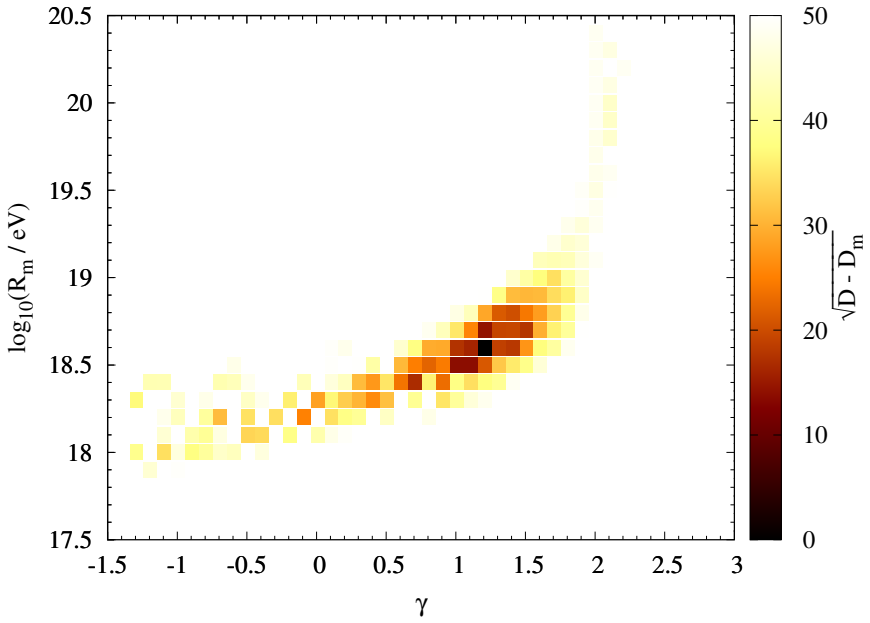

Figure 7.1: Likelihood scan performed using the Auger energy spectrum and X_{max} data with an astrophysical model of extragalactic propagation in the absence of magnetic fields. The color code shows the deviance $\sqrt{D - D_m}$, where D_m is the minimum deviance of the scan, for each point in the (γ, R_m) parameters space.

X_{max} data sample. In contrast with the case of rectilinear propagation, this scenario favors models with $-1.5 \lesssim \gamma \lesssim 1$, pointing to a harder injection spectrum at the sources. This can be explained as a consequence of the increase in the particles' track lengths in the extragalactic, which in turn, leads to larger energy losses that need to be compensated increasing the number of nuclei injected at the highest energies.

model	γ	$\log_{10}(R_m/\mathrm{EeV})$	j_0 $[au]$	f_{H} [%]	f_{He} [%]	f_{N} [%]	f_{Si} [%]	f_{Fe} [%]	α_{sys}
MHDAstro	-0.31	0.29	21.12	0	11	74	14	0	1.25
MHDPrimo	-0.49	0.25	19.81	1	83	11	4	0	1.23

Table 7.3: Best fit parameter values for the astrophysical scenarios of extragalactic propagation explored in this study using the Auger energy spectrum and $\mathrm{X}_{\mathrm{max}}$ data.

Table 7.3 shows the best-fit parameter values of the models describing the astrophysical scenarios explored in this work. One clear distinction between 1D- and the 3D-propagation-based astrophysical models is the sign of the spectral index γ, with $\gamma > 0$ preferred by the 1D case, whereas the 3D ones lie in $\gamma < 0$ region, both describing fairly well the spectrum and the

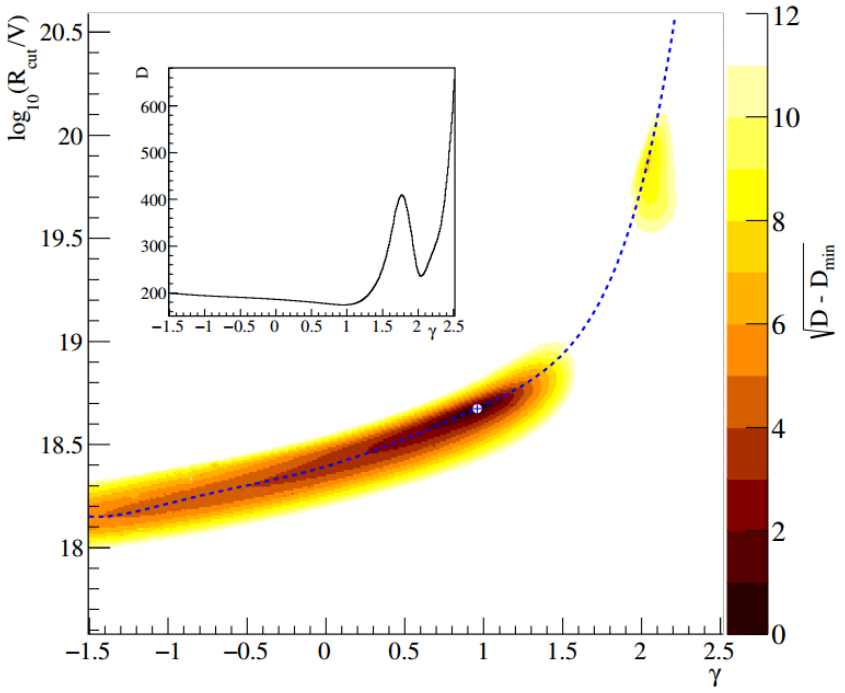

Figure 7.2: Likelihood scan obtained in [81] using the Auger energy spectrum and $X_{\max}$ data (collected up to 2017) with an astrophysical model of extragalactic propagation in the absence of magnetic fields. The color code shows the deviance $\sqrt{D - D_m}$, where D_m is the minimum deviance of the scan, for each point in the (γ, R_m) parameters space.

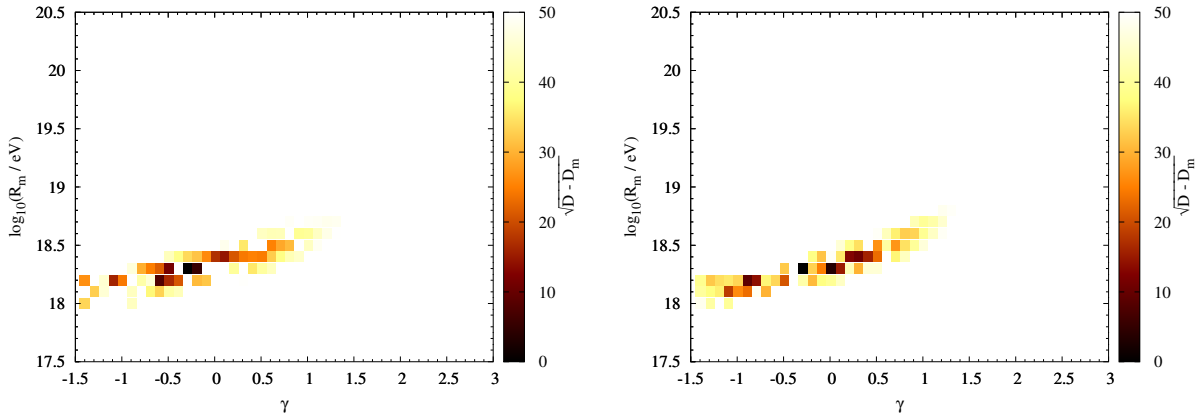

Figure 7.3: Likelihood scan of the astrophysical models explored using the energy spectrum and Xmax data with an astrophysical scenario of extragalactic propagation in an MHD-simulated magnetic field for the *astrophysical* (left) and *primordial* (right) models. The color code shows the deviance $\sqrt{D - D_m}$, where D_m is the minimum deviance of the scan, for each point in the (γ, R_m) parameters space.

$X_{\max}$ data. The values of γ for the 3D case exclude the classical first-order Fermi acceleration in relativistic shock waves, for which $\gamma \simeq 2.2$. On the other hand, models with inverted indexes ($\gamma < 0$) can be found in the literature, they can include acceleration in the winds of young neutron stars [94], in fast rotating pulsars [95], in the magnetosphere of black holes [96] and in AGN jets

model	D_J	$D_{X_{\max}}$	$D_{J+X_{\max}}$
MHDAstro	215	696	910
MHDPrimo	1270	1286	2556

Table 7.4: Deviance best-fit values for the astrophysical scenarios of extragalactic propagation explored in this study using the Auger energy spectrum and $X_{\max}$ data. The contributions coming from the energy spectrum (D_J) and $X_{\max}$ ($D_{X_{\max}}$) to the total deviance ($D_{J+X_{\max}}$) are also shown.

due to highly turbulent magnetic fields [97].

We also find that the exact values of the chemical fractions at the sources are strongly dependent on the minimizer starting point in the parameter space, indicating a level of correlation between the chemical fractions that was not possible to break with the available data set. This can be explained as a consequence of a great portion of the nuclei being injected with energies over the threshold of photodisintegration, resulting in a multitude of chemical sub-products of the nuclei injected during the propagation, leading finally to a partial loss of the initial information of the individual chemical contributions at the sources. A proper uncertainty estimate for the fractions would require an additional simulation campaign, which was not possible to perform during the thesis period.

Bibliography

[1] A. A. Penzias and R. W. Wilson. "A Measurement of Excess Antenna Temperature at 4080 Mc/s." In: *The Astrophysical Journal* 142 (1965), pp. 419–421.

[2] R. H. Dicke et al. "Cosmic Black-Body Radiation." In: *The Astrophysical Journal* 142 (1965), pp. 414–419.

[3] Ruth Durrer. "The cosmic microwave background: the history of its experimental investigation and its significance for cosmology". In: *Classical and Quantum Gravity* 32.12 (2015), p. 124007. ISSN: 1361-6382.

[4] Rudy C. Gilmore et al. "Semi-analytic modelling of the extragalactic background light and consequences for extragalactic gamma-ray spectra". In: *Monthly Notices of the Royal Astronomical Society* 422.4 (2012), 3189–3207. ISSN: 0035-8711.

[5] Asantha Cooray. *Extragalactic Background Light: Measurements and Applications*. 2016.

[6] Kalevi Mattila and Petri Väisänen. "Extragalactic background light: inventory of light throughout the cosmic history". In: *Contemporary Physics* 60.1 (2019), 23–44. ISSN: 1366-5812.

[7] Antoine Letessier-Selvon and Todor Stanev. "Ultrahigh energy cosmic rays". In: *Rev. Mod. Phys.* 83 (3 2011), pp. 907–942.

[8] D. Allard, E. Parizot, and A. V. Olinto. "On the transition from galactic to extragalactic cosmic-rays: Spectral and composition features from two opposite scenarios". In: *Astroparticle Physics* 27.1 (2007), pp. 61–75.

[9] R. Aloisio et al. "A dip in the UHECR spectrum and the transition from galactic to extragalactic cosmic rays". In: *Astropart. Phys.* 27 (2007), pp. 76–91. DOI: 10.1016/j.astropartphys.2006.09.004. arXiv: astro-ph/0608219.

[10] Noemie Globus, Denis Allard, and Etienne Parizot. "A complete model of the cosmic ray spectrum and composition across the Galactic to extragalactic transition". In: *Phys. Rev. D* 92 (2 2015), p. 021302.

[11] Javier G. Gonzalez. "Search for ultra-high energy neutrinos with the Pierre Auger Observatory". In: *Nuclear Instruments and Methods in Physics Research Section A: Accelerators, Spectrometers, Detectors and Associated Equipment* 725.Supplement C (2013), pp. 80 –84.

[12] Jacob Clay. "Penetrating Radiation". In: *Proceedings of the Section of Sciences, Koninklijke Akademie van Wetenschappen Te Amsterdam* 30 (1927), 1115–1127.

[13] W. Bothe and W. Kolhörster. "Das Wesen der Höhenstrahlung". In: *Zeitschrift fur Physik* 56.11-12 (1929), pp. 751–777.

[14] Bruno Rossi. "On the Magnetic Deflection of Cosmic Rays". In: *Physical Review* 36.3 (Aug. 1930), pp. 606–606.

[15] Thomas H. Johnson. "The Azimuthal Asymmetry of the Cosmic Radiation". In: *Physical Review* 43.10 (1933), pp. 834–835.

[16] Luis Alvarez and Arthur H. Compton. "A Positively Charged Component of Cosmic Rays". In: *Physical Review* 43.10 (1933), pp. 835–836.

[17] Bruno Rossi. "Directional Measurements on the Cosmic Rays Near the Geomagnetic Equator". In: *Physical Review* 45.3 (1934), pp. 212–214.

[18] Phyllis Freier et al. "Evidence for Heavy Nuclei in the Primary Cosmic Radiation". In: *Physical Review* 74.2 (1948), pp. 213–217.

[19] H. L. Bradt and B. Peters. "Investigation of the Primary Cosmic Radiation with Nuclear Photographic Emulsions". In: *Physical Review* 74.12 (Dec. 1948), pp. 1828–1837.

[20] M. Birkel and S. Sarkar. "Extremely high energy cosmic rays from relic particle decays". In: *Astroparticle Physics* 9 (1998), pp. 297–309.

[21] Christopher T. Hill, David N. Schramm, and Terry P. Walker. "Ultra-high-energy cosmic rays from superconducting cosmic strings". In: *Phys. Rev. D* 36 (4 1987), pp. 1007–1016.

[22] Veniamin Berezinsky and Alexander Vilenkin. "Cosmic Necklaces and Ultrahigh Energy Cosmic Rays". In: *Phys. Rev. Lett.* 79 (26 1997), pp. 5202–5205.

[23] Enrico Fermi. "On the Origin of the Cosmic Radiation". In: *Phys. Rev.* 75 (1949), pp. 1169–1174.

[24] A. R. Bell. "The acceleration of cosmic rays in shock fronts – I". In: *Monthly Notices of the Royal Astronomical Society* 182.2 (1978), pp. 147–156.

[25] R. D. Blandford and J. P. Ostriker. "Particle acceleration by astrophysical shocks". In: *Astrophysical Journal, Letters* 221 (1978), pp. L29–L32.

[26] R. D. Blandford and J. P. Ostriker. "Supernova shock acceleration of cosmic rays in the Galaxy". In: *Astrophysical Journal* 237 (1980), pp. 793–808.

[27] L O'C Drury. "An introduction to the theory of diffusive shock acceleration of energetic particles in tenuous plasmas". In: *Reports on Progress in Physics* 46.8 (1983), p. 973.

[28] R. A. Chevalier. "The interaction of supernovae with the interstellar medium". In: *Annual review of astronomy and astrophysics* 15 (1977), pp. 175–196.

[29] A. M. Hillas. "The Origin of Ultra-High-Energy Cosmic Rays". In: *Annual Review of Astronomy and Astrophysics* 22.1 (1984), pp. 425–444.

[30] Johannes Blümer, Ralph Engel, and Jörg R. Hörandel. "Cosmic rays from the knee to the highest energies". In: *Progress in Particle and Nuclear Physics* 63.2 (2009), 293–338. ISSN: 0146-6410.

[31] Todor Stanev. *High Energy Cosmic Rays*. 2nd ed. Springer, 2010, pp. 235–249.

[32] Kenneth Greisen. "End to the Cosmic-Ray Spectrum?" In: *Phys. Rev. Lett.* 16 (17 1966), pp. 748 –750.

[33] G. T. Zatsepin and V. A. Kuzmin. "Upper Limit of the Spectrum of Cosmic Rays". In: *Soviet Journal of Experimental and Theoretical Physics Letters* 4 (1966), p. 78.

[34] George R. Blumenthal. "Energy Loss of High-Energy Cosmic Rays in Pair-Producing Collisions with Ambient Photons". In: *Phys. Rev. D* 1 (6 1970), pp. 1596–1602.

[35] F. W. Stecker and M. H. Salamon. "Photodisintegration of Ultra-High-Energy Cosmic Rays: A New Determination". In: *The Astrophysical Journal* 512.2 (1999), p. 521.

[36] J. L. Puget, F. W. Stecker, and J. H. Bredekamp. "Photonuclear interactions of ultrahigh energy cosmic rays and their astrophysical consequences". In: *The Astrophysical Journal* 205 (1976), pp. 638–654.

[37] V.S. Ptuskin et al. "Diffusion and drift of very high energy cosmic rays in galactic magnetic fields". In: *Astronomy and Astrophysics* 268 (1993), pp. 726–735.

[38] Todor Stanev. "Ultra-high-energy Cosmic Rays and the Large-scale Structure of the Galactic Magnetic Field". In: *The Astrophysical Journal* 479.1 (1997), p. 290.

[39] Ronnie Jansson and Glennys R. Farrar. "The Galactic Magnetic Field". In: *The Astrophysical Journal Letters* 761.1 (2012), p. L11.

[40] Ronnie Jansson and Glennys R. Farrar. "A New Model of the Galactic Magnetic Field". In: *The Astrophysical Journal* 757.1 (2012), p. 14.

[41] Julián Candia, Silvia Mollerach, and Esteban Roulet. "Cosmic ray spectrum and anisotropies from the knee to the second knee". In: *Journal of Cosmology and Astroparticle Physics* 2003.05 (2003), p. 003.

[42] Julián Candia, Esteban Roulet, and Luis N. Epele. "Turbulent diffusion and drift in galactic magnetic fields and the explanation of the knee in the cosmic ray spectrum". In: *Journal of High Energy Physics* 2002.12 (2002), p. 033.

[43] Julián Candia, Silvia Mollerach, and Esteban Roulet. "Cosmic ray drift, the second knee and galactic anisotropies". In: *Journal of High Energy Physics* 2002.12 (2002), p. 032.

[44] A. A. Lee and R. W. Clay. "The anisotropy of EHE cosmic rays". In: *Journal of Physics G: Nuclear and Particle Physics* 21.12 (1995), p. 1743.

[45] Diego Harari, Silvia Mollerach, and Esteban Roulet. "Signatures of galactic magnetic lensing upon ultra high energy cosmic rays". In: *Journal of High Energy Physics* 2000.02 (2000), p. 035.

[46] Diego Harari et al. "Lensing of ultra-high energy cosmic rays in turbulent magnetic fields". In: *Journal of High Energy Physics* 2002.03 (2002), p. 045.

[47] J.R. Hörandel. "On the knee in the energy spectrum of cosmic rays". In: *Astroparticle Physics* 19 (2003), pp. 193–220.

[48] R. Aloisio, V. Berezinsky, and A. Gazizov. "Transition from galactic to extragalactic cosmic rays". In: *Astroparticle Physics* 39 (2012), pp. 129–143.

[49] The Pierre Auger Collaboration et al. *The Pierre Auger Observatory: Contributions to the 35th International Cosmic Ray Conference (ICRC 2017)*. 2017.

[50] J. Abraham et al. "Observation of the Suppression of the Flux of Cosmic Rays above 4×10^{19}eV". In: *Physical Review Letters* 101.6, 061101 (2008), p. 061101.

[51] J. Linsley. "Primary cosmic rays of energy 10^{17} to 10^{20} eV, the energy spectrum and arrival directions". In: *International Cosmic Ray Conference* 4 (1963), p. 77.

[52] A.H. Compton and I.A. Getting. "An Apparent Effect of Galactic Rotation on the Intensity of Cosmic Rays". In: *Physical Review* 47 (1935), pp. 817–821.

[53] M. Kachelriess and P.D. Serpico. "The Compton–Getting effect on ultra-high energy cosmic rays of cosmological origin". In: *Physics Letters B* 640.5 (2006), pp. 225 –229.

[54] Marius Grigat. "Large Scale Anisotropy Studies of Ultra High Energy Cosmic Rays Using Data Taken with the Surface Detector of the Pierre Auger Observatory". PhD thesis. Der Fakultät für Mathematik, Informatik und Naturwissenschaften der RWTH Aachen University, June 2011.

[55] Planck Collaboration et al. "Planck 2013 results. XXVII. Doppler boosting of the CMB: Eppur si muove". In: *A&A* 571 (2014), A27.

[56] Diego Harari, Silvia Mollerach, and Esteban Roulet. "Anisotropies of ultrahigh energy cosmic rays diffusing from extragalactic sources". In: *Phys. Rev. D* 89 (12 2014), p. 123001.

[57] D. Harari, S. Mollerach, and E. Roulet. "Anisotropies of ultrahigh energy cosmic ray nuclei diffusing from extragalactic sources". In: *Phys. Rev.* 92.6 (2015), p. 063014.

[58] John P. Huchra et al. "The 2MASS Redshift Survey—Description and Data Release". In: *The Astrophysical Journal Supplement Series* 199.2 (2012), p. 26.

[59] A. Aab et al. "Large Scale Distribution of Ultra High Energy Cosmic Rays Detected at the Pierre Auger Observatory with Zenith Angles up to 80°". In: *The Astrophysical Journal* 802 (2015), p. 111.

[60] J. Lloyd-Evans and A. A. Watson. "Invited Talks, 8th European Cosmic Ray Symposium". In: Iucci et al eds. Bologna, 1983.

[61] M. I. Pravdin et al. "Analysis of anisotropy of cosmic rays with the energy of about 10^{17} eV by Yakutsk EAS array data". In: *Journal of Experimental and Theoretical Physics* 92.5 (2001), pp. 766–770.

[62] N. Hayashida et al. "The anisotropy of cosmic ray arrival directions around 10^{18} eV". In: *Astroparticle Physics* 10 (1999), pp. 303–311.

[63] J.A. Bellido et al. "Southern hemisphere observations of a 10^{18} eV cosmic ray source near the direction of the Galactic Centre". In: *Astroparticle Physics* 15 (2001), pp. 167–175.

[64] J. Abraham et al. "Anisotropy studies around the galactic centre at EeV energies with the Auger Observatory". In: *Astroparticle Physics* 27 (2007), pp. 244–253.

[65] Pierre Auger Collaboration et al. "Search for first harmonic modulation in the right ascension distribution of cosmic rays detected at the Pierre Auger Observatory". In: *Astroparticle Physics* 34 (2011), pp. 627–639.

[66] The Pierre Auger Collaboration et al. "Observation of a Large-scale Anisotropy in the Arrival Directions of Cosmic Rays above 8×10^{18} eV". In: *Science* 357.6537 (2017), pp. 1266–1270.

[67] A. Aab et al. "Multi-resolution anisotropy studies of ultrahigh-energy cosmic rays detected at the Pierre Auger Observatory". In: *Journal of Cosmology and Astroparticle Physics* 2017.06 (2017), p. 026.

[68] D. Marinucci et al. "Spherical needlets for cosmic microwave background data analysis". In: *Monthly Notices of the Royal Astronomical Society* 383.2 (2008), pp. 539–545.

[69] Pierre Auger Collaboration. "Large-scale Cosmic-Ray Anisotropies above 4 EeV Measured by the Pierre Auger Observatory". In: *The Astrophysical Journal* 868.1 (2018), p. 4.

[70] Walter Heitler. *The Quantum Theory of Radiation*. 1st ed. Oxford At The Clarendon Press, 1936.

[71] J. Matthews. "A Heitler model of extensive air showers". In: *Astroparticle Physics* 22 (2005), pp. 387–397.

[72] T. Bergmann et al. "One-dimensional hybrid approach to extensive air shower simulation". In: *Astroparticle Physics* 26 (2007), pp. 420–432.

[73] S. Ostapchenko. "QGSJET-II: towards reliable description of very high energy hadronic interactions". In: *Nuclear Physics B Proceedings Supplements* 151 (2006), pp. 143–146.

[74] T. Pierog and K. Werner. "Muon Production in Extended Air Shower Simulations". In: *Phys. Rev. Lett.* 101 (17 2008), p. 171101.

[75] Eun-Joo Ahn et al. "Cosmic ray interaction event generator SIBYLL 2.1". In: *Phys. Rev. D* 80 (9 2009), p. 094003.

[76] J. Abraham et al. "Measurement of the Depth of Maximum of Extensive Air Showers above 10^{18} eV". In: *Physical Review Letters* 104.9 (2010), p. 091101.

[77] I. Allekotte et al. "The surface detector system of the Pierre Auger Observatory". In: *Nuclear Instruments and Methods in Physics Research A* 586 (2008), pp. 409–420.

[78] The Pierre Auger Collaboration et al. "The Fluorescence Detector of the Pierre Auger Observatory". In: *Nuclear Instruments and Methods in Physics Research Section A: Accelerators, Spectrometers, Detectors and Associated Equipment* 620.2 (2009), pp. 227 –251.

[79] Rafael Alves Batista et al. "CRPropa 3—a public astrophysical simulation framework for propagating extraterrestrial ultra-high energy particles". In: *Journal of Cosmology and Astroparticle Physics* 2016.05 (2016), 038–038. ISSN: 1475-7516.

[80] The Pierre Auger collaboration. "Bounds on the density of sources of ultra-high energy cosmic rays from the Pierre Auger Observatory". In: *Journal of Cosmology and Astroparticle Physics* 2013.05 (2013), 009–009. ISSN: 1475-7516.

[81] A. Aab et al. "Combined fit of spectrum and composition data as measured by the Pierre Auger Observatory". In: *Journal of Cosmology and Astroparticle Physics* 2017.04 (2017), 038–038. ISSN: 1475-7516.

[82] A. Domínguez et al. "Extragalactic background light inferred from AEGIS galaxy-SED-type fractions". In: *Monthly Notices of the Royal Astronomical Society* 410.4 (2010), pp. 2556–2578.

[83] R. Alves Batista et al. "Effects of uncertainties in simulations of extragalactic UHECR propagation, using CRPropa and SimProp". In: *Journal of Cosmology and Astroparticle Physics* 2015.10 (2015), pp. 063–063. ISSN: 1475-7516.

[84] A.J. Koning and D. Rochman. "Modern Nuclear Data Evaluation with the TALYS Code System". In: *Nucl. Data Sheets* 113 (2012), pp. 2841–2934.

[85] T. Pierog et al. "EPOS LHC: Test of collective hadronization with data measured at the CERN Large Hadron Collider". In: *Physical Review C* 92.3 (2015).

[86] A. Aab et al. "Depth of maximum of air-shower profiles at the Pierre Auger Observatory: Measurements at energies above $10^{17.8}$ eV". In: *Physical Review D* 90.12 (2014).

[87] T. Pierog et al. "First results of fast one-dimensional hybrid simulation of EAS using CONEX". In: *Nuclear Physics B - Proceedings Supplements* 151.1 (2006), pp. 159–162.

[88] Antonella Castellina. "Highlights from the Pierre Auger Observatory (ICRC2019)". In: (2019).

[89] F. James and M. Roos. "Minuit: A System for Function Minimization and Analysis of the Parameter Errors and Correlations". In: *Comput. Phys. Commun.* 10 (1975), pp. 343–367. DOI: 10.1016/0010-4655(75)90039-9.

[90] "ROOT — An object oriented data analysis framework". In: *Nuclear Instruments and Methods in Physics Research Section A: Accelerators, Spectrometers, Detectors and Associated Equipment* 389.1 (1997). New Computing Techniques in Physics Research V, pp. 81–86. ISSN: 0168-9002.

[91] Nicusor Arsene. "Mass Composition of UHECRs from Xmax Distributions Recorded by the Pierre Auger and Telescope Array Observatories". In: *Universe* 7.9 (2021), p. 321.

[92] S Hackstein et al. "Simulations of ultra-high energy cosmic rays in the local Universe and the origin of cosmic magnetic fields". In: *Monthly Notices of the Royal Astronomical Society* 475.2 (2018), pp. 2519–2529.

[93] R Aloisio et al. "SimProp: a simulation code for ultra high energy cosmic ray propagation". In: *Journal of Cosmology and Astroparticle Physics* 2012.10 (2012), pp. 007–007.

[94] P. Blasi, R. I. Epstein, and A. V. Olinto. "Ultra–High-Energy Cosmic Rays from Young Neutron Star Winds". In: *The Astrophysical Journal* 533.2 (2000), pp. L123–L126.

[95] Kumiko Kotera, Elena Amato, and Pasquale Blasi. "The fate of ultrahigh energy nuclei in the immediate environment of young fast-rotating pulsars". In: *Journal of Cosmology and Astroparticle Physics* 2015.08 (2015), pp. 026–026.

[96] K. Ptitsyna and A. Neronov. "Particle acceleration in the vacuum gaps in black hole magnetospheres". In: *Astronomy &amp Astrophysics* 593 (2016), A8.

[97] Tobias Winchen and Stijn Buitink. "Energy spectrum of fast second order Fermi accelerators as sources of ultra-high-energy cosmic rays". In: *Astroparticle Physics* 102 (2018), pp. 25–31.